Technische Universität München
International Max-Planck Research School on Astrophysics
Max-Planck-Institut für Extraterrestrische Physik

X-Ray Analysis of Starburst and AGN Components

Yi Fan

Vollständiger Abdruck der von der Fakultät für Physik der Technischen Universität München zur Erlangung des akademischen Grades eines

Doktors der Naturwissenschaften

genehmigten Dissertation.

Vorsitzender:	Univ.-Prof. Dr. M. Ratz
Prüfer der Dissertation:	
	1. Hon.-Prof. Dr. G. Hasinger
	2. Univ.-Prof. Dr. R. Krücken

Die Dissertation wurde am 19.04.2007 bei der Technischen Universität München eingereicht und durch die Fakultät für Physik am 14.05.2007 angenommen.

SUMMARY

The X-ray properties of Starburst and Active Galactic Nuclei (AGN) components of three galaxies (NGC 6240, NGC 2782, and NGC 1386) in the local universe are analysed in this dissertation. These galaxies are well suited to study the physics of Starburst and AGN components. They serve as the nearby laboratories for the corresponding objects at high redshifts. The X-ray observations of these galaxies were performed with the ACIS-S detector of *Chandra X-ray observatory*. The *Chandra* ACIS-S imaging spectroscopy allows us to do both imaging analysis and spectral analysis of the data in great detail. It is possible for us to spatially resolve the different contributing components of the complex sources, do the spectral analysis of these components separately, and derive their physical properties systematically.

The *Chandra* ACIS-S observation of the Ultraluminous Infrared galaxy **NGC 6240** which contains a binary AGN, demostrates that starburst and AGN components contribute to its X-ray emission. The bright extended emission, both near the AGNs and extending over spatial scales of 10 kpc, probably originates from hot thermal plasma and high-mass X-ray binaries. This emission is attributed to starburst activity. The 2-10 keV luminosity of the bright extended emission correlated with the infrared luminosity is a good indicator of the current global star formation rate in the galaxy. Surrounding the bright extended emission, a weak halo component appears to be extended on a scale of $\sim$40 kpc, with evidence for thermal emission (with a constant temperature $kT \sim 0.6$ keV). The northern and southern AGNs located in the center of the galaxy are heavily obscured and the reflection components dominate in the *Chandra* bandpass. Strong neutral Fe Kα lines at 6.4 keV are detected from the two nuclei. The southern nucleus is also found to show ionized iron lines at energies higher than 6.4 keV, indicating the existence of a warm scattering medium. A "jet-like" structure close to the southern nucleus seems to be scattered emission.

For the starburst galaxy **NGC 2782**, the *Chandra* data allow us to disentangle the X-ray emission from this galaxy, for the first time, into three contributing components. A weak large-scale halo emission extends northward and southward, respectively. The bright extended emission including a southern shell-like emission is correlated with the optical (Hα) and radio bubble structures. The correlation of X-ray and optical/radio emission as well as the thermal-plasma spectrum of the bright extended emission indicates starburst-driven superwinds as the origin. In the center of the galaxy, a compact core source dominates in the high energy X-ray band (above 2 keV). We found indications for an Fe Kα line with large equivalent width. Therefore, the emission from this compact core source is most likely the reflected/scattered component of an obscured AGN. However, we can not rule out the possibility of an Ultraluminous X-ray source (ULX) in the center of this galaxy, even though we consider it unlikely.

In the Seyfert 2 galaxy **NGC 1386**, the soft X-ray extended emission is spatially resolved and coincident with the optical [OIII] emission from the narrow line region (NLR). The spectrum of the extended emission can be fitted by a black-body or a bremsstrahlung model. A soft X-ray structure north of the nucleus is correlated with an optical blob in the [OIII] images. This structure is in the outer part of the NLR. The large equivalent width of the Fe Kα line in combination with the ratio of the [OIII] and X-ray luminosity suggests that the AGN in NGC 1386 is also heavily obscured.

ZUSAMMENFASSUNG

In der vorliegenden Dissertation werden die Röntgeneigenschaften von Starburst - und aktiven galaktischen Kern (AGN) - Komponenten dreier Galaxien (NGC 6240, NGC 2782, NGC 1386) im lokalen Universum analysiert. Diese Galaxien eignen sich gut dazu, die Physik von Starburst und AGN Komponenten zu untersuchen. Sie dienen als nahe Laboratorien für die entsprechenden Objekte bei höheren Rotverschiebungen. Die Beobachtungen dieser drei Galaxien wurden mit dem ACIS-S Detektor des Röntgensatelliten Chandra durchgeführt. Die abbildende Spektroskopie mit Chandra's ACIS-S erlaubt es uns, eine sehr genaue Analyse sowohl von direkten Abbildungen, als auch von Spektren durchzuführen. So ist es damit möglich, die unterschiedlichen beitragenden Komponenten der komplexen Quellen räumlich aufzulösen, ihre Spektren zu analysieren und ihre physikalischen Eigenschaften systematisch herzuleiten.

Die Beobachtung der extrem leutchkräftigen Infrarotgalaxie **NGC 6240**, die einen Doppel-AGN-Kern enthält, mit dem ACIS-S Detektor demonstriert, dass Starburst und AGN Komponenten zu ihrer Röntgenemission beitragen. Die helle ausgedehnte Emission, nahe der AGNs ist über einen räumlichen Bereich von 10 kpc ausgedehnt, und wird wahrscheinlich von heissem thermischem Plasma und von massereichen Röntgendoppelsternen erzeugt. Diese Emission ist der Starburst-Aktivität zuzuordnen. Die 2-10 keV Helligkeit der hellen ausgedehnten Emission, die mit der Infrarothelligkeit korreliert ist, ist ein guter Indikator für die derzeitige Sternentstehungsrate der Galaxie. Diese helle ausgedehnte Emission ist von einer schwachen Halokomponente umgeben, die sich bis auf $\sim$ 40 kpc ausdehnt, in der es Anzeichen für thermische Emission gibt (mit einer konstanten Temperatur von kT $\sim$ 0.6 keV). Die nördlichen und südlichen AGNs im Zentrum der Galaxie sind stark verdunkelt, so daß ihre reflektierenden Komponenten im Chandra Energieband dominieren. Stark ausgeprägte neutrale Fe Kα Linien wurden in beiden Kernen nachgewiesen. Im Spektrum des südlichen Kerns findet man außerdem Linien von ionisiertem Eisen bei Energien höher als 6.4 keV, was auf die Existenz eines warmen Streumediums schliessen lässt. Eine Jet-ähnliche Struktur nahe des südlichen Kerns scheint durch gestreute Strahlung zustandezukommen.

Für die Starburstgalaxie **NGC 2782** erlauben die Chandra-Daten es uns zum ersten mal, die Röntgenemission in drei beitragende Komponenten aufzuspalten. Eine schwache Halostrahlung breitet sich jeweils nach Norden und Süden aus. Die helle ausgedehnte Strahlung, die auch eine schalenartige Struktur im Süden beinhaltet, ist mit einer blasenartigen optischen (Hα) und Radio Struktur korreliert. Die Korrelation der optischen/Radio Emission, so wie das thermische Spektrum der hellen ausgedehnten Strahlung legen einen durch Starburst getriebenen Superwind als Ursache nahe. Im Zentrum der Galaxie dominiert eine kompakte Quelle die harte Röntgenstrahlung (oberhalb von 2 keV). Wir finden Anzeichen für eine Eisenlinie mit hoher Äquivalentbreite, deshalb ist die Emission dieser kompakten Kernquelle höchstwahrscheinlich auf die reflektierte/gestreute Komponente eines verdeckten AGN zurückzuführen, wobei eine ultraleuchtkräftige Quelle im Zentrum dieser Galaxie nicht ausgeschlossen werden kann, auch wenn das eher unwahrscheinlich ist.

Die weiche Röntgenstrahlung in der Seyfert-2 Galaxie **NGC 1386** wurde räumlich aufgelöst und fällt mit der optischen [O III] Emission der schmalen Emissionslinienregion (NLR) zusammen. Das Spektrum der ausgedehnten Strahlung kann durch ein

Schwarzkörperstrahlungs - oder ein Bremsstrahlungs-Modell angenähert werden. Eine klumpenartige Struktur im weichen Röntgenband nördlich des Kerns ist mit einem Emissionsgebiet im optischen [O III] verbunden. Diese Struktur ist im äusseren Teil der NLR. Die große Äquivalentbreite der Fe Kα Linie in Verbindung mit dem Verhältnis von [O III] und der Röntgenhelligkeit legen nahe, dass der AGN in NGC 1386 ebenso stark obskuriert ist.

TABLE OF CONTENTS

LIST OF FIGURES

LIST OF TABLES

CHAPTER 1
INTRODUCTION

X-ray emission in galaxies originates from gravitational potential energy release in accretion processes and/or the processes of intense star formation (starbursts). Active galactic nuclei (AGNs) are understood to be non-thermal, high-energy X-ray (above 2 keV; hereafter hard X-ray) emitters with accretion processes onto nuclear supermassive (10^6-10^8 $M_\odot$) black holes. Thermal, low-energy X-ray (below 2 keV; hereafter soft X-ray) emission from hot gas is a general characteristic of starbursts, which may be highly extended via large-scale outflows produced by supernovae and stellar winds. Observations at X-ray wavelengths provide a good insight into the energetic phenomena with both starburst and AGN components.

The emphasis of the X-ray analysis in this dissertation is on the physical processes of AGN and starburst which are related to a wealth of astronomical objects. In this introduction I will concisely give a description of the astrophysical backgrounds which have a close connection with the subjects presented in this dissertation. I will start the introduction with brief summaries of the basic astrophysical understandings of AGN and starburst activities in Section 1.1 and in Section 1.2 respectively. A description of the main properties of Ultraluminous Infrared galaxies (ULIRGs) will be given in Section 1.3. After introducing the currently active *Chandra X-ray Observatory* in Section 1.4, I will point out the aims of X-ray analysis and list the selected objects in Section 1.5. I will then draw an outline of this dissertation in Section 1.6.

1.1 Obscured Active Galactic Nuclei

According to the so-called unified models (see Figure 1.1) of active galactic nuclei (see Antonucci 1993 for a review), the apparently different Seyfert 1 and Seyfert 2 galaxies are intrinsically the same. The different appearance is interpreted as a consequence of an orientation effect. The obscuring torus surrounding the central nuclei blocks the line of sight to the nuclei in Seyfert 2 galaxies, which contain identical nuclei compared to Seyfert 1 galaxies. A clear knowledge of the amount of obscuring gas is crucial to understand the physical properties and the nature of Seyfert galaxies. X-ray observations indicate that the spectra of many Seyfert 2 galaxies have the characteristic of a power-law similar to those observed in Seyfert 1s and a photoelectric cut-off due to the obscuring gas along the line of sight. According to the column density of absorbing gas, the obscured AGNs can be classified into "Compton thin" and "Compton thick". If $N_{\rm H} \leq 10^{24}$ cm^{-2}, X-rays above a few keV can pass through the torus and the source nuclei will be visible to the observers; in this case, the source is named as "Compton thin". If $N_{\rm H} \geq 1.5 \times 10^{24}$ cm^{-2}, no direct X-ray emission from the nuclei is observable below 10 keV; in this case, the source is called "Compton thick". For 10^{24} cm$^{-2} \leq N_{\rm H} \leq 10^{25}$ cm^{-2}, only X-rays in the energy range of 10-100 keV can penetrate the torus, and therefore the column density can only be estimated in this energy range. For $N_{\rm H} \geq 10^{25}$ cm^{-2}, the source is completely hidden from view.

For Compton-thick Seyfert galaxies, X-ray emission in 0.1-10 keV is dominated by reprocessed components: a cold reflected component and/or a warm scattered component (see Mushotzky et al. 1993 for a review). The cold reflected component is

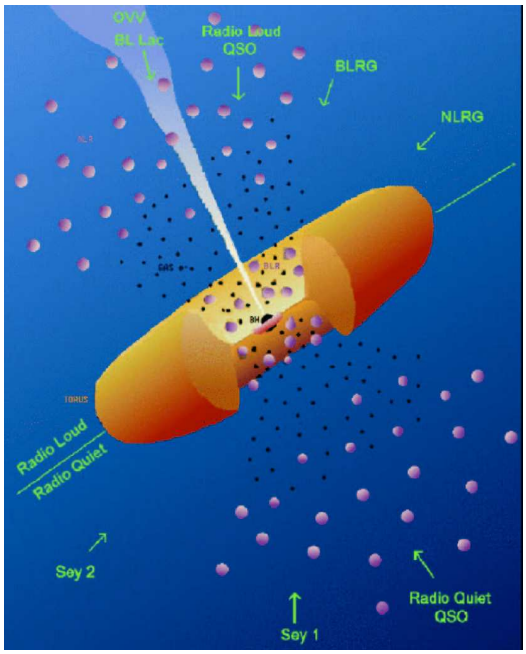

Figure 1.1: A schematic diagram of the unified AGN model. There is a whole zoo of different quasar/AGN types which differ in various observational properties. The unified AGN model interprets the difference between Seyfert 1 and 2 as due to the different viewing angle towards the intrinsically same type of source.

attributed to the optically thick, but geometrically thin accretion disk, and characteristic of an Fe Kα fluorescence line at 6.4 keV with the large Equivalent Width (EW $>$ 1 keV with respect to the reflected continuum). The Fe Kα line could be produced by reflection from the inner edge of the circumnuclear absorbing gas (Ghisellini et al. 1994) or, alternatively, by transmission through the torus itself (Leahy & Creighton 1993). The warm scattered component, as it is observed in many cases, is produced by a photoionized, warm scattering medium close to the nucleus. This is also the origin of the soft emission lines as well as He-like and H-like iron lines at 6.67 and 6.97 keV. The soft X-ray emission lines due to photoionization and photoexcitation by the AGN have been clearly demonstrated in some cases (e.g. NGC 1068: Kinkhabwala et al. 2002, Brinkman et al. 2002).

Because of heavy obscuration towards AGNs, a fraction of AGNs does not have the typical Seyfert features in the optical spectra but has the classical signatures of starburst activity. Those objects are named "elusive" AGNs by Maiolino et al. (2003). These elusive AGNs are in general optically classified as starbursts or LINERs (low-ionization nuclear emission-line regions[1]).

X-ray observations provide the convincing evidence for these obscured AGNs which are buried in strong starbursts, as mentioned above. Some of the luminous hard X-

[1]LINERs are characterized by optical spectra dominated by emission lines of moderate intensities arising from gas in lower ionization states than classical AGNs (e.g. Ho 1999). One key question that is still in dispute is whether the nuclear emission of LINERs arises from starbursts or accretion onto supermassive black holes.

ray sources, with little or without evidence for AGN activities in optical/Infrared(IR) wavelengths, have been detected by deep *Chandra* X-ray surveys (e.g. Mushotzky et al. 2000; Brandt & Hasinger 2005 and references therein). It is possible that many of these sources are the corresponding objects at high redshifts to the "elusive" AGNs in the local universe. "Compton thick" AGNs comprise about 50% of all Seyfert 2 galaxies in the local universe (e.g. Risaliti et al. 1999). Such a large population of heavily obscured AGNs could also be existing, but very difficult to detected at high redshifts.

1.2 Starbursts

Starbursts are brief episodes of intense star formation lasting $\leq 10^8$ yr, which are significant components of the present-day universe. They are powered by high-mass stars ($M \geq 8M_{\odot}$) which are very luminous and short-lived and therefore trace relatively recent star formation. Starbursts are distinctive laboratories for exploring the physical characteristics of star formation, the evolution of high-mass stars, and the interstellar medium. They are also the local analogues of the processes at higher redshifts (Heckman 1998; 2000; 2001; 2003).

1.2.1 Starburst-driven Superwinds

An expected consequence of starbursts is superwinds - galactic-scale outflows of gas driven by the collective effect of the large numbers of supernovae and stellar winds, from the host galaxy into the intergalactic medium (e.g. Chevalier & Clegg 1985; Heckman et al. 1993a; Veilleux et al. 2005 for a recent review). In the past years, multi-wavelength observations of optical line emission, thermal soft X-ray emission, and non-thermal radio emission, have provided unambiguous evidence of the existence of starburst-driven superwinds. They have not only been detected in local edge-on starburst galaxies (e.g. Lehnert & Heckman 1996) but also been indicated in starbursts at high redshifts (e.g. Pettini et al. 2000).

Superwinds are complex multiphase outflows of cool, warm, and hot gas, dust, and magnetized relativistic plasma (Heckman 2003). X-rays observations are uniquely important for the research of superwinds since X-rays are a good tracer of the hot gas. The mass M_X and energy E_X of the X-ray gas scale as follows: $M_X \propto (L_X f)^{1/2}$ and $E_X \propto (L_X f)^{1/2} T_X (1+M^2)$. Here L_X is the X-ray luminosity, T_X is the gas temperature, f is the volume-filling-factor of the X-ray gas and M is its Mach number. Numerical hydrodynamical simulations of superwinds indicates that $M^2 = 2$ to 3 (Strickland & Stevens 2000), and it is argued that f is of-order 10^{-1} (Heckman 2003).

The thermal soft X-ray emission from superwinds in starburst galaxies is found to be fitted by thermal plasma models comprising one or more components with the typical temperature in the range between 0.1 and 1.0 keV (e.g. Dahlem et al. 1998). Superwinds transport large amounts of metal-enriched gas from starburts into the intergalactic medium and/or gaseous halos around galaxies. X-ray spectral data of some starburst galaxies indicate super-solar abundance ratios for the α-elements relative to Fe (e.g. Ptak et al. 1997; Fabbiano et al. 2004; Strickland et al. 2004).

It has been repeatedly reported that there is a strong correlation between Hα and X-ray emission, not only within the central $\sim$ 1 kpc scales of starbursts but also on $\sim$ 10 kpc scales (e.g. McCarthy et al. 1987; Heckman et al. 1996; Lehnert et al. 1999; Strickland et al. 2002). In many cases, the strongly limb-brightened spatial correlations are expected if the X-ray emission is generated by the interaction of the superwinds with cool ambient gas. However, X-ray emission without significant limb-brightening is also observed and indicates a partially filled volume of warm gas with the shocked wind, in contrast to a shell of conductively heated gas. (e.g. NGC 3079, Cecil et al. 2002). In some cases, the distributions of soft X-ray emission are also influenced by absorption by foreground neutral interstellar medium (e.g. Strickland et al. 2000; Stevens et al. 2003).

1.2.2 X-ray spectral components of Starburst galaxies

X-ray spectral components of starburst galaxies have recently been assessed by Persice & Rephaeli (2002), based on the X-ray spectral features of M82 and NGC 253 and a stellar-population evolutionary model. They improved a model for the evolution of galactic stellar populations and drew the conclusions for the complex spectrum of starburst galaxies. They have identified different spectral components of starburst galaxies, such as X-ray binaries, supernova remnants, Compton scattering of ambient far-infrared photons off supernova-accelerated relativistic electrons, diffuse thermal plasma and a compact nucleus of starburst or AGN emission. They point out that a diffuse thermal plasma is assumed to dominate at soft X-rays ($\leq$ 2 keV) in starburst galaxies, which results mainly from shock heating by the interaction between the hot winds and the ambient interstellar medium. They interpret high- and low-mass X-ray binaries (HMXBs and LMXBs) as the main contributors for the spectra in 2-15 keV. The population-averaged spectrum of X-ray binaries is effectively represented by a cut-off power-law and an additional Fe K emission from HMXBs.

The recent X-ray studies of starburst galaxies have shown that without X-ray emission from an AGN, the most prominent stellar component in the 2-10 keV band is the contributions from a few bright off-nuclear X-ray point sources (e.g. Colbert et al. 2004). The brightest sources of these discrete X-ray point-like objects are called Ultraluminous X-ray sources (ULXs) with X-ray luminosities larger than 10^{39} erg s^{-1} which are in excess of the Eddington limit for accretion onto a 1.4 M$_\odot$ neutron star. For example, in NGC4038/4039 (the Antennae), the actively star-forming merging galaxies, quite a few ULXs are detected in *Chandra* observations (Zezas et al. 2002).

1.3 Ultraluminous Infrared Galaxies

Ultraluminous Infrared galaxies (ULIRGs), regarded as the most luminous objects in the local universe, were discovered in the early 1970s (Rieke & Low 1972). ULIRGs have IR luminosities in excess of 10^{12} $L_\odot$ and the emission is dominated by the mid- and far-infrared bands. Most of them occupy gas-rich interacting/merging galaxy systems as well (see Sanders & Mirabel 1996 for an early review).

It is widely accepted that the immense infrared luminosity is due to the existence

of a great amount of warm dust which is heated by the primary power source(s) and emits infrared radiation. But the nature of the power sources is controversial. Starbursts and/or AGNs activities may be responsible for the power sources, however, their relative contributions are still unconstrained.

ULIRGs are found to be more numerous at high-red-shift universe than in the local universe. ULIRGs at high redshifts contribute significantly to the cosmic infrared background and play a role in large-scale structure formation. ULIRGs are frequently involved in the context of the evolutionary scenarios, considerable efforts in both observational and theoretical extragalactic astronomy have been invested in recent years to debate this issue. One of the scenarios is the merger-driven evolutionary scheme: cool ULIRGs → warm ULIRGs → quasars; another scenario is the unification-by-orientation of AGN. These scenarios indicate the close connections between starbursts and AGNs activities. (see Lonsdale et al. 2006 a recent review of ULIRGs).

These current understandings are responsible for the growing interests in local ULIRGs. Firstly, studying local ULIRGs is helpful to determine the relative contributions of starbursts and AGNs as the energy sources in ULIRGs. We are able to investigate the physical processes by which galaxies were built and the heating and metal enrichment of the intergalactic medium in great detail.

Secondly, local ULIRGs are excellent laboratories for the study of distant ULIRGs. Many important hints are expected from the study, since distant ULIRGs have many properties in common with the local counterparts, though they show some differences. Thirdly, the detailed behaviors of local ULIRGs are of extreme importance for the research of the evolutionary scenarios involving ULIRGs and the roles of both starbursts and AGNs in these scenarios.

The astrophysics of local ULIRGs has been studied by multi-wavelength observations, such as optical, near-IR, mid-IR, radio continuum, and X-rays, including both imaging and spectroscopy. We do not cover plenty of literature on the observational results at multi-wavelengths here, but only outline some key points at X-ray wavelength, which are of relevance to this dissertation.

X-ray observations are particularly fundamental to determine the nature of the nuclear X-ray sources and distinguish between AGN and starburst emission in ULIRGs. In some cases, classifications based on optical and IR spectroscopic studies may not reflect the true nature of the dominant nuclear sources. For example, although NGC 6240 is identified as an optical LINER and starburst-dominated (Lutz et al. 1999; Imanishi & Dudley 2000), AGN activity has been found to have significant contribution to the hard X-rays according to X-ray studies via different X-ray observatories. (e.g. Schulz et al. 1998; Iwasawa & Comastri 1998; Vignati et al. 1999). The *Chandra X-ray Observatory* with unprecedented resolution and sensitivity compared to the previous instruments, has a striking ability to diagnose the real features of the nuclear energy sources. NGC 6240, for example, shows a spectacular and fascinating phenomenon: a binary AGN in the nuclear region is revealed in *Chandra* ACIS-S observation by Komossa et al. (2003).

Starburst-driven superwinds related to thermal emission are commonly discovered in ULIRGs. In X-rays, extended thermal emission from superwinds driven by starburst in local ULIRGs was first detected in Arp 220, observed by *ROSAT* soft X-ray telescope (Heckman et al. 1996). X-ray emission in 0.1-2.4 keV extending out to several kpc,

is morphologically related with the optical emission-line nebula, indicating that both X-rays and optical emission arise as the consequence of starburst-driven superwinds.

Thanks to two currently active X-ray missions, the *X-Ray Multi-Mirror Mission-Newton* (*XMM-Newton*: Jansen et al. 2001) and the *Chandra X-ray Observatory*, some individual ULIRGs are well studied in great detail, such as Arp 220 (McDowell et al. 2003), Mrk 231 (Gallagher et al. 2002; Braito et al. 2004), Mrk 273 (Xia et al. 2002; Balestra et al. 2005). In addition to these analysis of individual objects, the results of three recent ULIRGs survey programs have also been presented:

1. *XMM-Newton* X-ray survey of ULIRGs (Franceschini et al. 2003) including 10 ULIRGs demonstrates that ULIRGs are intrinsically faint X-ray sources, with the observed X-ray luminosities being typically $L_{2-10keV} \leq 10^{42}$-10^{43} ergs s^{-1}. Thermal plasma emission is evident in all sample sources, dominating in soft X-ray (0.5-1 keV) spectra, related with starburst activity. The X-ray emission extends out to a scale of $\sim$ 30 kpc for Mrk 231 and IRAS 19254-7245, indicating the presence of starburst-driven superwinds. Four out of ten ULIRGs show evidence for the existence of hidden AGNs, and one of them seems to have a minor AGN contribution. In the remainders of the ULIRG sample, X-ray emission is most likely due to thermal plasma and X-ray binaries, as starburst origins.

2. Ptak et al. (2003) present a *Chandra* survey of the eight nearest (Z $\leq$ 0.04) ULIRGs, in addition to NGC 6240[2]. In every object of the sample, a hard X-ray source is detected in the nuclear region. Three of these near ULIRGs classified as AGNs show about an order of magnitude smaller hard X-ray luminosities than the other five ULIRGs classified as starbursts. NGC 6240 has a higher value than the latter.

3. The results of a further ULIRG (0.04 < Z < 0.16) *Chandra* survey comprising 14 ULIRGs are presented by Teng et al.(2005). In this analysis, hardness ratios are used to estimate the X-ray spectral properties. The photon indices of the objects in both this sample and the *Chandra*-2003 sample by Ptak et al., peak in the range between 1 and 1.5. For those in the sample classified as Seyfert galaxies, the photon indices are larger than 2. Despite a plausible interpretation that X-ray properties of the sample are due to starburst activity, the possibility of Compton-thick AGNs can not be ruled out.

1.4 The Chandra Mission

1.4.1 Overview

The currently active *Chandra* Mission (Weisskopf et al. 2000), together with the *XMM-Newton* observatory, lead us to enter a new era of studying X-ray astrophysics. Now, We give a brief introduction to the *Chandra X-ray Observatory*,[3] by which all the relevant data in this dissertation are obtained.

NASA's *Chandra X-ray Observatory* (CXO) was launched and deployed by Space

[2]NGC 6240 is taken as an IR-luminous galaxy by Ptak et al. (2003), since $L_{IR} = 10^{11.8}\ L_{\odot}$ is just below the ULIRGs luminosity criterion of $10^{12}\ L_{\odot}$.

[3]Elaborate descriptions can be found at http://chandra.harvard.edu/.

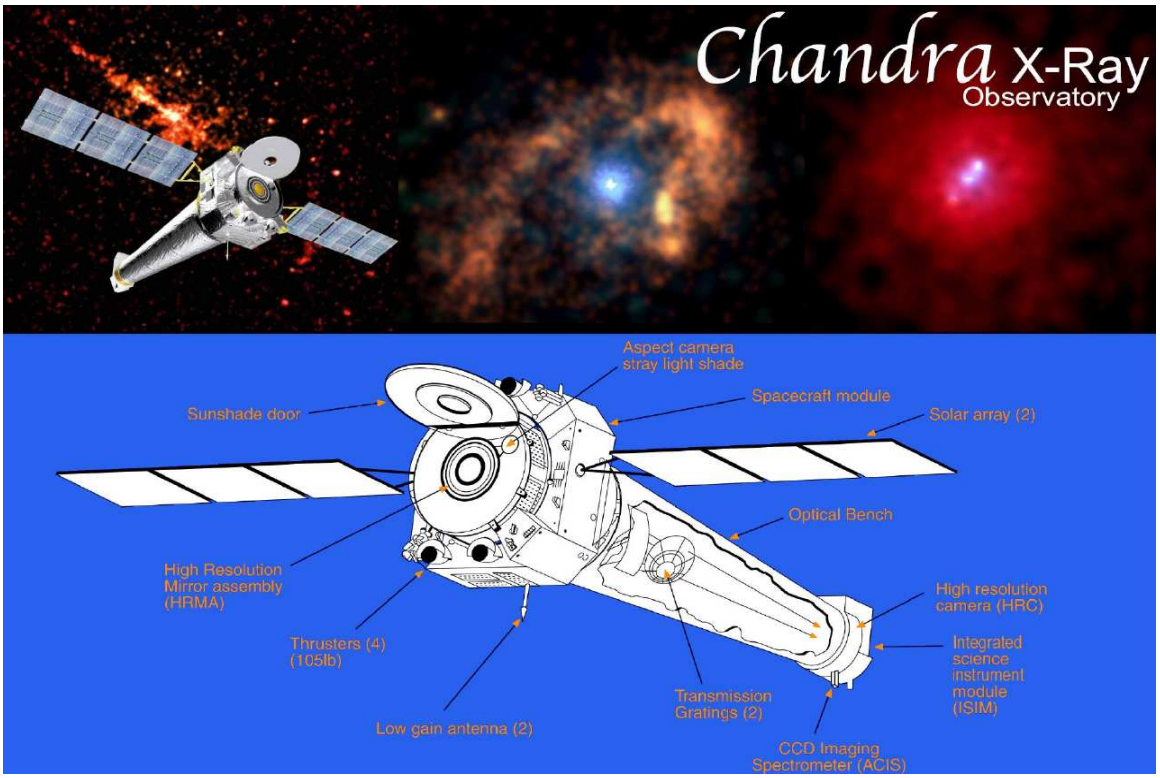

Figure 1.2: A labeled illustration of the *Chandra X-ray Observatory*. Ten CCD chips in 2 arrays of ACIS provide imaging and spectroscopy. HRC uses large field-of-view mircro-channel plates to make X-ray images.

Shuttle *Columbia* on July 23, 1999. Figure 1.2 shows a lbeled illustration of this observatory. CXO has unprecedented powers of sub-arcsecond imaging, spectrometric imaging and high-resolution dispersive spectroscopy in the X-ray energy bands 0.08-10 keV, which allows to explore a wealth of high-energy astrophysical phenomena involving a variety of astronomical objects.

There are two focal plane instruments. One is a High Resolution Camera (HRC),and the other one is an Advanced CCD Imaging Spectrometer (ACIS). ACIS is an array of charged coupled devices. A two-dimensional array of these small detectors does simultaneous imaging and spectroscopy. Pictures of extended objects can be obtained along with spectral information from each element of the picture.

High spatial resolution is required to separate the contribution of different spectral components and to perform spatially-resolved spectroscopy. Fortunately, this superb capability is provided by the detectors on *Chandra*. The high-resolution *Chandra* X-ray observations have significantly increased our understanding of various sources and will deepen this understanding in the coming years.

1.4.2 On-orbit performance

Chandra is designed to provide the high-quality X-ray data and is a unique X-ray astronomy facility for high-resolution imaging and for high-resolution spectroscopy.

The angular resolution of *Chandra* is significantly better than any previous, or current, X-ray observatory. The point spread function (PSF) as measured in ground calibration, had a full width at half-maximum (FWHM) less than 0.5 arcsec and a half-power diameter (HPD) less than 1 arcsec. According to a figure[4] in which the fractional encircled energy is plotted as a function of the radius actually observed in flight (ACIS-S), a 1-arcsec-diameter circle encloses an encircled energy of $\sim 85\%$ at 6.4 keV.

1.4.3 Scientific performance

X-ray emission from highly energetic processes, either thermal or non-thermal can be well studied. *Chandra*'s capability of high-resolution imaging allows the detailed high-resolution research of the structures of extended X-ray sources, e.g. supernova remnants, astrophysical jets, hot gas in galaxies and clusters of galaxies. Moreover, the capability for spectrometric imaging permits us to study structure in X-ray intensity, temperature and chemical composition. Therefore, it is possible that some important astrophysical topics, such as galaxy mergers and dark matter, can be investigated by these observations. Except for the studies of extended structures of X-ray emission, the superb angular resolution affords the possibility of exploring the discrete sources. Populations of individual X-ray sources, with luminosities comparable to those of Galactic X-ray binaries, can be detected at the distance of the Virgo Cluster and beyond; the emission of these sources can be separated from the diffuse emission of hot interstellar gases, both spatially and spectrally (see Fabbiano 2006 for a review).

1.5 The aims and the selected objects

Chandra provides us with unique information about the morphology of X-ray emission. With this information we are able to build models for the different components in spectral analysis. Owing to the surpassingly good resolution of *Chandra*, the different emitting components of the sources will be spatially separated. A detailed study involving the respective physical properties of nearby "pure" obscured AGN objects and "pure" starburst galaxies in the local universe, and the relative importance of AGN and starburst activities in nearby ULIRGs, can be well performed by analyzing *Chandra* ACIS-S data. Such a study may have profound effects on the understandings of both activities and the merger processes, on the construction of the models of cosmological evolution of these two activities, and on the estimations of their contributions to the energy density of universe. To execute such a study, three nearby galaxies are carefully selected from the Chandra Data Archive[5]. With the high spatial resolution and simultaneous spectroscopic data from *Chandra* ACIS-S observations, I will analyze X-ray emission of AGN and/or starburst activities of the following three galaxies in this dissertation:

1. **NGC 6240**

[4]Proposers' Observatory Guide v.9: http://cxc.harvard.edu/proposer/POG/
[5]http://cxc.harvard.edu/cda/

As mentioned in Section 1.3, the local ULIRGs are well suited to study the physical nature of these sources in great detail. As one of the nearest ULIRGs, NGC 6240 is a unique representative powered by both starbursts and AGNs, which has two intrinsically luminous but heavily obscured AGNs and extended soft X-ray emission. Taking advantage of *Chandra* ACIS-S, a wealth of information of X-ray emission from NGC 6240 can be easily exploited in a systematic analysis method.

2. **NGC 2782**

The best laboratories for investigating the astrophysical properties of starburst-driven superwinds are in nearby galaxies, since the complex features can be clearly studied in great detail and the multi-components can be easily disentangled. Moreover, for an exhaustive investigation of superwinds, the best viewing geometry is edge-on galaxies, in which one can easily discriminate between the disk itself and the emission outside the disk plane of the galaxy. NGC 2782 is such a nearby starburst galaxy seen nearly edge-on, hence a favorable object for these investigations. Based on the optical spectroscopy, the nature of the central source is still unclear, and thus the additional aim is to unveil the true features of the nucleus and to look for a Fe Kα line at 6.4 keV in spectral data in the band 2-10 keV.

3. **NGC 1386**

For the Compton-thick Seyfert 2 galaxies with very high column densities, nuclear radiation can be observed by the radiation of a cold reflected component and/or a warm scattered component. These two scattered components have different spectra properties. NGC 1386 is a Compton-thick Seyfert 2 galaxy in the local universe. The analysis of *Chandra* ACIS-S observation of NGC 1386 is expected to check whether a combination of cold and warm reflections is a plausible model for the X-ray emission from the galaxy.

Both imaging analysis and spectral analysis show valuable clues which help us understand the physical natures of these sources. In imaging analysis, different components which change depending on energies, can be identified and isolated in X-ray energy images. Morphological comparisons between the images of X-ray emitting gas and multi-wavelength emission images (e.g. optical line-emission, radio emission, and molecular gas, and so on) may provide important hints to the nature of the X-ray emission. In spectral analysis, a systematic method will be adopted, based on the spatial information yielded by imaging analysis. (The detailed description of this method will be given in the following chapters.) By using this systematic analysis method, it is possible to isolate the different components correctly and fit them properly. Adopting this method can avoid the ambiguities in spectral model fitting. The ambiguities often appear when the total emission (a sum of multi-components) is not properly disentangled and has to be fitted as a whole. Interrelating X-ray data and multi-wavelength observations of the galaxies, the reliable conclusions on the multi-component sources will be drawn.

1.6 Outline of this dissertation

In this dissertation, I will present the X-ray analysis of three galaxies: NGC 6240, NGC 2782, and NGC 1386. This dissertation is organized as follows:

The *Chandra* ACIS-S observation of NGC 6240 will be systematically examined in Chapter 2, including imaging and spectral analysis. The data reduction and analysis methods will be described, the results on both extended emission and nuclear sources will be reported, and astrophysical implications will be discussed.

In Chapter 3, the key characteristics of starburst-driven superwinds in NGC 2782 are described and the true nature of the nuclear source is discussed.

The study of NGC 1386 is presented in Chapter 4, including a detailed investigation of the extended emission of the galaxy and the physical understandings about this object.

Concluding remarks of the results and some prospective views of follow-up investigations are given in Chapter 5.

CHAPTER 2
NGC 6240

2.1 Introduction

NGC 6240 has $L_{IR} = 10^{11.8}\ L_{\odot}$ which is just below the ULIRGs luminosity criterion of $10^{12}\ L_{\odot}$. Nevertheless NGC 6240 has much in common with ULIRGs sources, it is as a ULIRG in this thesis.

NGC 6240, as an interacting and merging galaxy, shows both the AGN and starburst activities. X-rays are a powerful tracer for both of the activities. Starburst-driven superwinds, viewed as strong evidence for the starburst activity, have extended emission in soft X-rays (Schulz et al. 1998; Komossa et al. 1998; Iwasawa & Comastri 1998; Lira et al. 2002; Komossa et al. 2003). On the other hand, many pieces of evidence point toward the existence of AGN emission in NGC 6240, which can contribute a significant fraction of the FIR luminosity. Hard X-rays observations offer an important tool to detect the obscured AGN. *ACSA* data show a flat power-law emission with a strong Fe K line complex around 6.4 keV (e.g. Mitsuda 1995; Iwasawa & Comastri 1998), suggesting what is observed is the reflection emission from an obscured AGN. *BeppoSAX* results were used to argue that it is the AGN that dominates the energy output (Vignati et al. 1999). Moreover, *Chandra* imaging spectroscopy observations disentangle the contribution to the hard X-ray luminosity from two AGNs in the center of NGC 6240 (Komossa et al. 2003). The Fe K line complex is resolved into three distinct narrow lines in *XMM-Newton* observations (Boller et al. 2003): (i) the neutral Fe Kα line (6.4 keV); (ii) an ionized line at 6.70 keV; (iii) an ionized line at 7.0 keV (a blend of the Fe XXVI and the Fe Kβ).

However, previous X-ray investigations have not included the systematic study of the different spatial regions of NGC 6240. Though the X-ray structures are known to be strongly dependent on energy, the nature of the extended emission, possibly including individual spatial components, are less well defined than that of the nuclear sources. One systematic study is indeed required in order to determine whether there is strong evidence for spatial variations in physical properties (e.g. temperture, metal abundance, etc.) for the different spatial regions. Such a study is particularly important to the inner region because of the more inner region may have more different components which overlap spatially. The most outer region is expected to only have one simple component, which is likely to be projected onto the inner regions. Only when the physical nature of the most outer region is reliably determined, the inner regions can be systematically studied in the next step in a consistent manner. This is essential to exploit the complex physical features of X-ray emission in NGC 6240.

The high spatial resolution and simultaneous spectroscopic data of NGC 6240 taken with the *Chandra* Advanced CCD Imaging Spectrometer (ACIS) are analysed in this chapter. The different contributing components are separated, and the individual regions for the spectral analysis are specified. We then construct the suited models and fit the spectra individually. Considering that quite a lot of information has been yielded by multi-wavelength observations, we also compare X-ray with non-X-ray characteristic properties to study the physical nature of these components.

For consistency with previous analysis, we adopt a distance of 144 Mpc ($H_o = 50$ km s^{-1} Mpc^{-1}) for NGC 6240. At this distance, 1″ corresponds to a physical distance of 700 pc. The distance D is ~ 100 Mpc if we use $H_o = 75$ km s^{-1} Mpc^{-1}.

We list some results obtained from previous multi-wavelengths observations in Section 2.1.1, and describe the *Chandra* ACIS-S observation in Section 2.1.2. In Section 2.2, we present the imaging analysis including isolating the different components and specifying the regions. The spectral properties of these individual regions are derived in Section 2.3. We discuss the main results and summarize the conclusions in Section 2.4 and 2.5, respectively.

2.1.1 Previous observations

As mentioned above, NGC 6240 has been observed intensely at multi-wavelengths. Here I list some previous results.

NGC 6240 shows a highly disturbed morphology (Fosbury & Wall 1979), and optical images of NGC 6240 revealed two bright peaks with a separation of 1.8″ (Fried & Schulz 1983). It is widely accepted that NGC 6240 is a system of two merging galaxies. Ground-based optical observations of NGC 6240 imply a starburst associated with a starburst-driven superwind cavity in which shocked clouds produce the LINER-like lines.

In the radio observations of NGC 6240 with the Very Large Array (VLA), no solid evidence for the existence of AGN activity was found by Colbert et al. (1994). A MERLIN (the Multi-Element Radio Linked Interferometer Network) study shows that NGC 6240 contains a double nucleus (Beswick et al. 2001). The recent Very Long Baseline Array (VLBA) radio observations reveal three compact sources (Gallimore & Beswick 2004), two associated with hard X-ray sources (Komossa et al. 2003).

IR Observations of NGC 6240 suggest that it appears to starburst-dominated (Genzel et al. 1998; Lutz et al.1999; Imanishi & Dudley 2000). The high-resolution near-infrared integral field spectroscopy by Tecza et al. (2000) indicates that red supergiants dominating the K-band light is formed in starbursts with an age of 1.5-2.5 $\times$ 10^7 yr and therefore the entire bolometric luminosity of NGC 6240 can be explained by the starburst. It is worth noting that the IR results contradict the above-mentioned X-ray results.

The optical emission-line nebula is interpreted as the evidence of starburst-driven superwinds by Heckman et al.(1987, 1990). *Hubble Space Telescope* (*HST*) WFPC2 Hα image (Gerssen et al. 2004) shows extended filaments and loop-like structures, which is correlated with most of the X-ray emission (Lira et al. 2002; Komossa et al. 2003). The correlation between Hα and X-rays supports the scenario of starburst-driven superwinds in NGC 6240, which offers a plausible explanation for both optical and X-ray emission.

2.1.2 Chandra observations and data reduction

This study is based on Chandra observations (OBSID 1590) of NGC 6240, obtained on 2001 July 29 with a total exposure time of 37.16 ks. The galaxy was placed on the back-illuminated chip ACIS-S3 (chip 7). The first results from these observations have

been reported by Komossa et al. (2003). The initial processing of the raw data was carried out by the *Chandra X-ray Center* (CXC), with the processing pipeline software (version 6.2.2). In the following data reduction, I mainly used the CIAO software [1] tools to analyze the "Level 2" event files, which are filtered on good time intervals, resulting in an effective exposure time of 37.00 ks. I examined the light curves extracted from an area of 5.6 arcmin^2 within the energy range of 0.3-10.0 keV and found no significant flares. Therefore, it was not necessary to further clean the data to remove periods of high background levels, and the data within the standard good time intervels of 37.00 ks were used.

I filtered the raw data to include events within energies of 0.5-8.0 keV. The counts below 0.5 keV were ignored, because there is the large uncertainty of the quantum efficiency at energies below this value and few photons are detected. The upper bound of 8.0 keV was chosen, as the effective area of the High Resolution Mirror Assembly (HRMA) drops and the particle background rises sharply above 8.0 keV. I also used XIMAGE [2], a multi-mission X-ray image display and analysis program, to plot images in the imaging analysis. For the spectral analysis, the FTOOLS "grppha" was used to group the data into bins with at least 15 counts for χ^2 fitting. Then, the data were fitted with the X-ray spectral fitting tool XSPEC[3].

The redshift of NGC 6240 is 0.02448, from NASA/IPAC Extragalactic Database (NED)[4]. The Galactic column density in the direction of NGC 6240 $N_{\rm H,Gal}$= 5.78 $\times$ 10^{20} cm^{-2} is calculated according to the position of NGC 6240[5].

2.2 Imaging analysis

2.2.1 Morphology and different contributing components

The multi-color image in soft (red), medium (green), and hard (blue) X-rays bands (taken from Fig. 3 by Komossa et al. 2003) is shown in Figure 2.1. Besides two point-like AGNs, extended "butterfly-like" structure, extending out to 15″ is present in this image.

To investigate how the morphology of diffuse emission varies with energy, unbinned images are extracted from the events file in four carefully chosen bands: 0.5-1.0 keV, 1.0-1.5 keV, 1.5-2.0 keV, and 2.0-2.5 keV. The four images were adaptively smoothed by the CIAO task "csmooth". This tool smoothes a two-dimensional image with a circular Gaussian kernel of varying size and employs a signal-to-noise (S/N) criterion to determine the smoothing scale[6].

This S/N criterion takes the background of the raw image into account. It leads to significantly improved noise suppression in the case of large-scale features embedded in high background (which may be another really physical feature at even larger scale). Both the minimum and maximum S/N ratios above the background required under the

[1] http://cxc.harvard.edu/ciao/
[2] http://heasarc.gsfc.nasa.gov/docs/xanadu/ximage/ximage.html
[3] http://heasarc.gsfc.nasa.gov/docs/xanadu/xspec/index.html
[4] http://nedwww.ipac.caltech.edu/
[5] http://heasarc.gsfc.nasa.gov/docs/tools.html
[6] see CIAO Manuals: Transformation, Convolution, and Deconvolution.

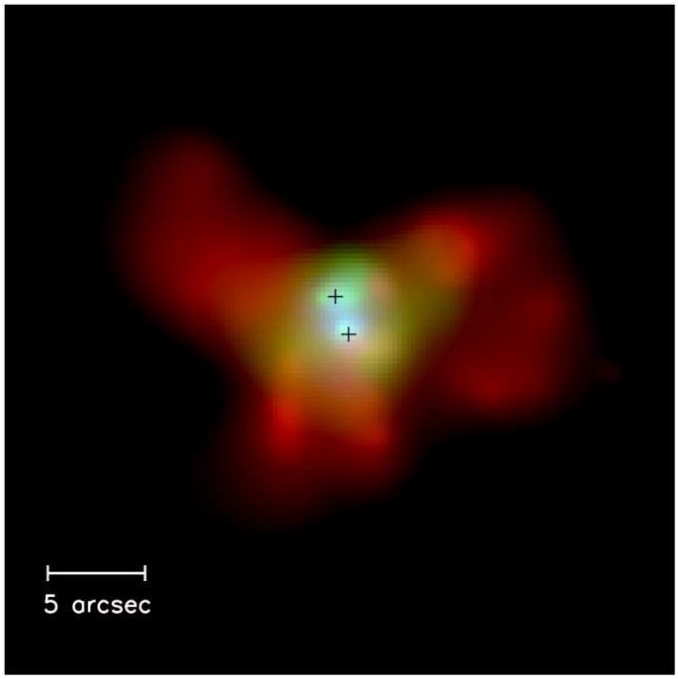

Figure 2.1: The *Chandra* multi-color images of NGC 6240 in soft (0.5-1.5 keV, red), medium (1.5-5.0 keV, green) and hard (5.0-8.0 keV, blue) X-ray bands, respectively. (taken from Komossa et al. 2003, see text).

kernel are needed to be specified, in order to ensure the statistically significant structure is not over-smoothed to a level of significance much higher than the minimum value. The adaptively smoothed images are used only for presentation and definition of the extraction regions. All spectral analyses were preformed by extracting photons from the individual regions of the events file.

Figure 2.2 shows the adaptively smoothed image of the 0.5-1.0 energy band ACIS-S image with a large image size up to 4 arcmin^2, which represents diffuse emission with a wide variety of spatial scales. This spectacular image shows a low surface brightness soft halo in the region (green and blue) surrounding the bright "butterfly-like" structure, extending out to at least 42 kpc (60″ at D = 144 Mpc) from the nuclei of NGC 6240. The large-scale emission may be lower intensity than that of the inner bright extent, as suggested by the varied range of colors.

The bright "butterfly-like" structure is the most striking feature of the diffuse soft emission within 14 kpc (20″) which predominates in the 0.5-2.5 keV energy band. Figure 2.3 shows that the energy-dependent feature includes three 10 kpc size (15″) loop-like structures, extending northeast, northwest and south, respectively.

Southwest of the southern nucleus, a spatially extended, "jet-like" structure appears above 1 keV and it is the strongest feature in 1.0-1.5 keV (Komossa et al. 2003). The phrase "jet-like" is used here only to describe the morphology of this feature, without a implication on its true nature. Figure 2.4 is the small-scale energy (0.5-1.5 keV) image, indicating the spatially resolved structure. It seems to be related with a region of increased Hα emission (see Figure 2.5). The hard X-ray (5.0-8.0 keV) emission is

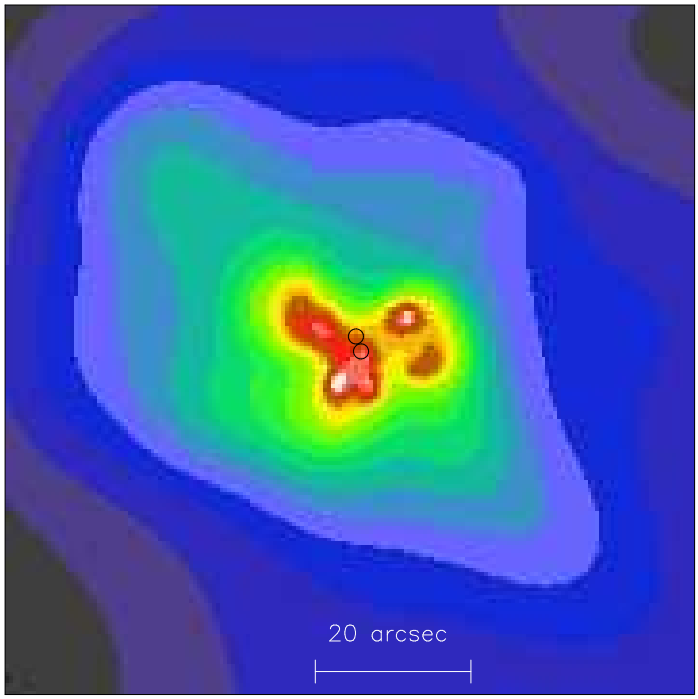

Figure 2.2: Wide-field adaptively smoothed image of the diffuse emission. The color scale was selected to highlight the low surface brightness diffuse emission (in green and blue) with large scales. The black circles mark the optical positions of the two nuclei in the center of NGC 6240.

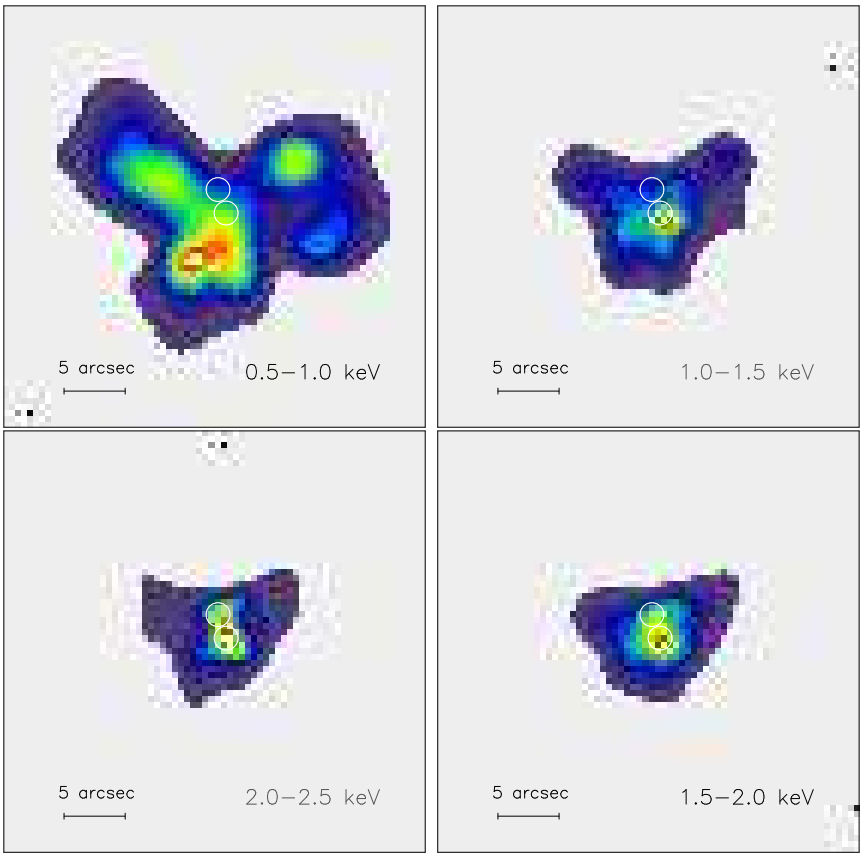

Figure 2.3: Adaptively smoothed images of NGC 6240 in selected energy bands: 0.5-1.0 keV, 1.0-1.5 keV, 1.5-2.0 keV, and 2.0-2.5 keV bands (in clockwise order). The white circles mark the optical positions of the two nuclei of NGC 6240.

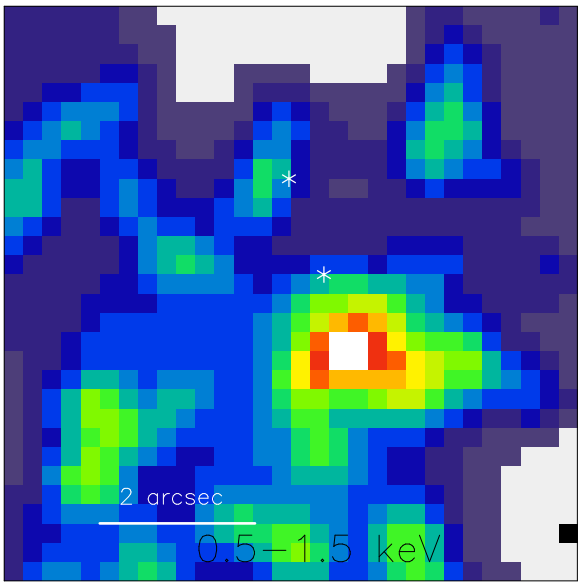

Figure 2.4: An Adaptively smoothed image (in 0.5-1.5 energy band) of the "jet-like" structure in NGC 6240. The white stars mark the positions of two nuclei. Close to the southern nucleus, the white, red, orange, and yellow colours represent the "jet-like" structure.

highly concentrated around the nuclear areas. More information is shown in Section 2.2.2.

The CIAO tool, wavedetect[7] was used to search the point sources in the *Chandra* ACIC-S images of NGC 6240. Though a few point sources within a radius of 2′ were detected, none except for the two nuclei was found within the X-ray bright, "butterfly-shaped" extent of the galaxy. It is possible that the putative point sources are too weak to be detected where the local background due to diffuse emission is high. Therefore, the lack of the detection of the supposed point sources is not unreasonable when they are embedded in bright diffuse emission (see Section 2.4.3 for a further discussion).

2.2.2 Specification of individual regions

According to the presented smoothed images, there are different components in X-ray emission of NGC 6240, which are clearly identified in the smoothed images. To spatially isolate the different contributing components, several individual regions are carefully chosen in Figure 2.6. We have chosen the projected radius of r=20″ (14 kpc) as dividing line between what is termed as the halo component and the bright extended regions. All the regions, but the halo region, are marked in Figure 2.6 with the abbreviations. These regions are defined below.

Northern nucleus (N): A circular region with a radius of 1.″0, centered at α= 16^h52^m $58.^s919$, δ=02°24′04.″98.

[7]The method used by *Wavedetect* correlates the data with a wavelet function. Each pixel's correlation value is compared with the expected distribution of values; if the value is an extreme outlier with this distribution, the pixel is assumed to be associated with a source. See http://cxc.harvard.edu/ciao/download/doc/detect_manual/ for more details.

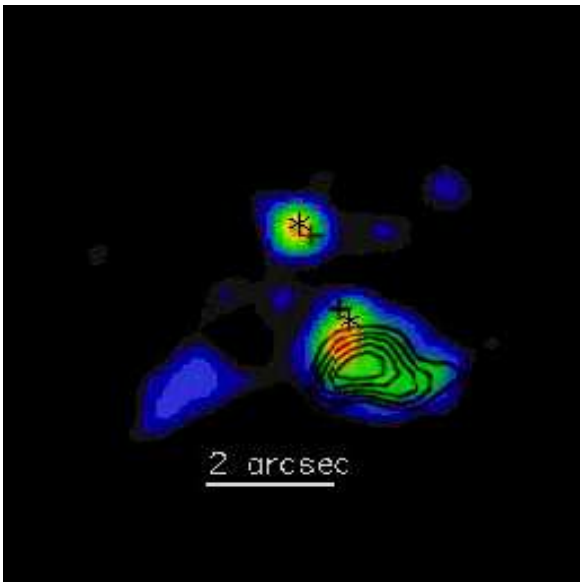

Figure 2.5: Overlay of X-ray contours on Hα intensity image for the "jet-like" emission of NGC 6240 (in 0.5-1.5 keV band). Contour levels are drawn at 0.509, 0.570, 0.634, 0.696, 0.759 $\times$ 10^{-3} counts s^{-1} $arcsec^{-2}$. The two X-ray nuclei are marked by thick crosses and the optical nuclei are marked by asterisks. The white bar represents 2″.

Southern nucleus (S): A circular region with a radius of 1.″0, centered at α= 16^h52^m $58.^s875$, δ=02°24′03.″06.

"Jet-like" structure (J): A 2.″5 $\times$ 1.″7 rectangular region centered 1.″8 southeast of the southern nucleus (α= $16^h52^m58.^s78$, δ=02°24′01.″90) with the shorter side in P.A. = 51°.

Region 1 (R1): An elliptical region northwest of the nuclei centered at α= $16^h52^m58.^s4$, δ=02°24′06.″6, along P.A. = 47°, with ellipse radii of 5.″8 and 8.″7, respectively.

Region 2 (R2): An elliptical region northeast of the nuclei centered at α= $16^h52^m59.^s.4$, δ=02°24′09″.4, along P.A. = 49°, with ellipse radii of 6.″9 and 7.″5, respectively.

Region 3 (R3): An elliptical region southwest of the nuclei centered at α= $16^h52^m59.^s0$, δ=02°23′57.″4, along P.A.= 143°, with ellipse radii of 6.″1 and 4.″2, respectively.

The Extended Region (E): A circular region with a radius of 20″, centered on the southern nucleus, *excluding* the regions of two nuclei and the "jet-like" structure, and including Region 1, 2, and 3.

Halo : an annulus aperture with inner and outer radii, 20″ and 60″, respectively.

We adopt three bands for the estimates of count rate for the regions defined above: soft (0.5-1.5 keV), medium (1.5-5.0 keV) and hard (5.0-8.0 keV). For each region, the angular size, the area, the observed background subtracted count rate are listed in Table 2.1.

The total counts in 5.0-8.0 keV band of the Extended Region is more than the sum of Region 1, 2 and 3. The "extra" counts are most likely located in the area between Regions 1, 2 and 3, but spatially spread over the center of NGC 6240 extending further than the above defined regions of two nuclei and the jet-like structure. On one hand,

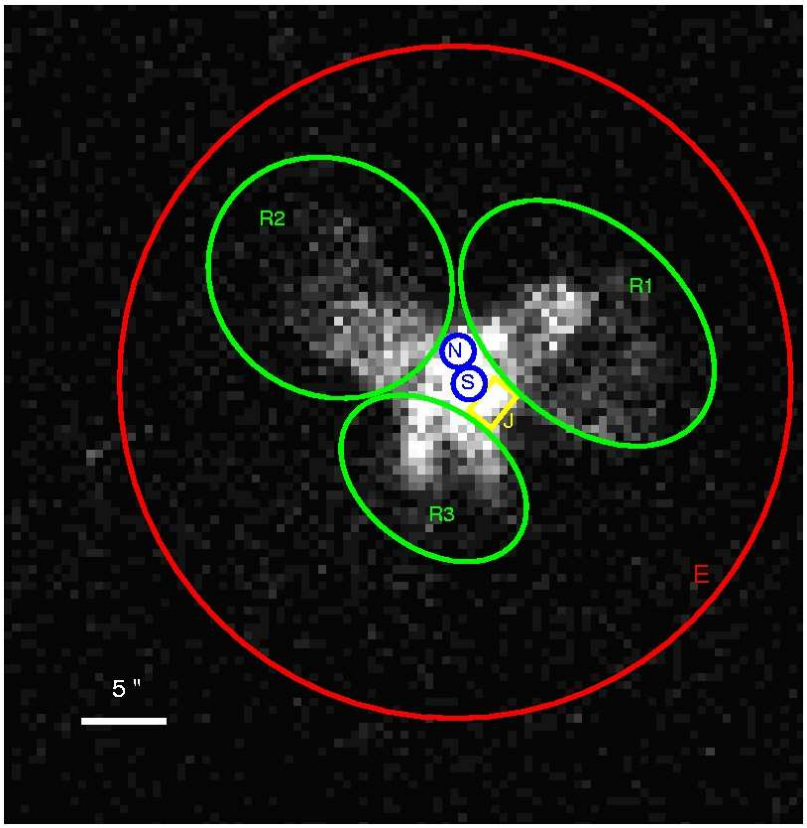

Figure 2.6: Individual regions of NGC 6240 are marked in the raw image of NGC 6240 (see text). The white bar represents 5".

this may be mainly due to the point spread function (PSF) of *Chandra* HRMA which has a broad low-level wing at high X-ray energies. Therefore, the unresolved nuclear emission can be spread out by the mirror PSF, and X-ray photons at higher energies can be located outside the two nuclear circle regions and the jet-like region. (For example, a 1-arcsec-diameter circle encloses an encircled energy of $\sim 85\%$ at 6.4 keV.) Thus, the Extended Region could have "extra" counts in 5.0-8.0 keV band due to the contamination by the wings of PSF.

On the other hand, a real extension of the nuclear emission can account for hard X-ray emission arising at a scale of several arcseconds, because of the scattered nuclear emission by the dense molecular clouds. Considering the distributions of the counts in the 5.0-8.0 keV range, We speculated that the highly concentrated hard X-ray emission is due to the spread-out/scattered nuclear emission. Spectral analysis for the Extended Region in Section 2.3.4 will further support this speculation.

Table 2.1: Count rates for each region. Col.(1): The individual regions as defined in the text. Col.(2) Total area of each region in units of arcsec^2. Col.(3)-(8): Background-subtracted count rates, and total number of counts in soft, medium, and hard energy bands.

		Soft 0.5-1.5 keV		Medium 1.5-5.0 keV		Hard 5.0-8.0 keV	
Region	Area	Total Counts	Counts s^{-1}	Total Counts	Counts s^{-1}	Total Counts	Counts s^{-1}
(1)	(2)	(3)	(4)	(5)	(6)	(7)	(8)
Northern nucleus	2.969	87	0.00237±0.00025	299	0.00815±0.00047	107	0.00291±0.00028
Southern nucleus	2.969	177	0.00482±0.00036	410	0.01117±0.00055	236	0.00643± 0.00042
Jet-like structure	4.223	196	0.00534±0.00038	240	0.00654±0.00042	16	0.00043±0.00011
Region 1	160.228	1220	0.03326±0.00096	600	0.01635±0.00067	37	0.00102±0.00017
Region 2	163.329	1122	0.03058±0.00092	362	0.00986±0.00052	9	0.00026±9.85E-5
Region 3	80.572	1158	0.03157±0.00093	427	0.01164±0.00056	18	0.00050±0.00012
The Extended Region	1246.497	4603	0.12547±0.00187	2096	0.05711±0.00126	147	0.00400±0.00036
Halo	10054.595	1320	0.03599±0.00147	168	0.00459±0.00074	8	0.00023±0.00060

Table 2.2: The estimate of astrometric accuracy for the observations. Three point-like sources detected in the *Chandra* X-ray images, within 6′ from NGC 6240 have optical counterparts. The *Chandra* X-ray source coordinates (Right Ascension α and Declination δ) are given in Col. (2) and (3). Col.(4) and (5) list the positional differences ($\Delta\alpha$ and $\Delta\delta$) with respect to the optical coordinates. Finally, Col.6 gives the radial offsets.

Sources	α(J2000)	δ(J2000)	$\Delta\alpha$	$\Delta\delta$	Radial Offset
	hh:mm:ss	dd:mm:ss	″	″	″
(1)	(2)	(3)	(4)	(5)	(6)
1	16:53:09.739	02:23:33.74	-0.468	-0.514	0.557
2	16:53:04.669	02:21:17.71	-0.540	-0.429	0.689
3	16:52:38.160	02:22:02.00	-0.432	-0.549	0.691

2.2.3 Metallicity map

A metallicity map of the diffuse emission is presented in Figure 2.7. The Fe L complex (0.7-1.1 keV) contours are plotted over the smoothed oxygen emission (0.5-0.7 keV). The abundance of these two elements have a similarity that both of them are mainly distributed in the bright "butterfly-like" extended regions, such as R1, R2, and R3 regions (as in Section 2.2.2). But it seems that it matches badly with the small-scale regions in the center. Because of the weakness of oxygen emission, it does not allow for the detailed comparison of these two metal abundances within the different small-scale regions.

2.2.4 X-ray/optical counterparts and the absolute astrometric accuracy

In order to check the absolute astrometric accuracy, I searched optical counterparts from the online Digitized Sky Survey (DSS) corresponding to the *Chandra* X-ray sources within 6′ from the galaxy. Three optical sources are identified to be the counterparts of X-ray point-like sources detected in the *Chandra* X-ray image. It suggests there is a systematic shift between X-ray and optical images. Table 2.2 lists the X-ray coordinates (Right Ascension α and Declination δ) of the three sources, the positional differences with respect to the optical coordinates ($\Delta\alpha$ and $\Delta\delta$ in arcsec) and the radial offsets[8] (in arcsec). This gives an estimate of absolute astrometric accuracy of these observations, to $\sim$0.7 arcsec, consistent with the latest estimates from the calibration team of CXC[9] (on 9 June 2006).

[8]The offset is simply the distance from X-ray source centroid to the measured position of the optical counterpart.

[9]http://cxc.harvard.edu/cal/ASPECT/celmon/

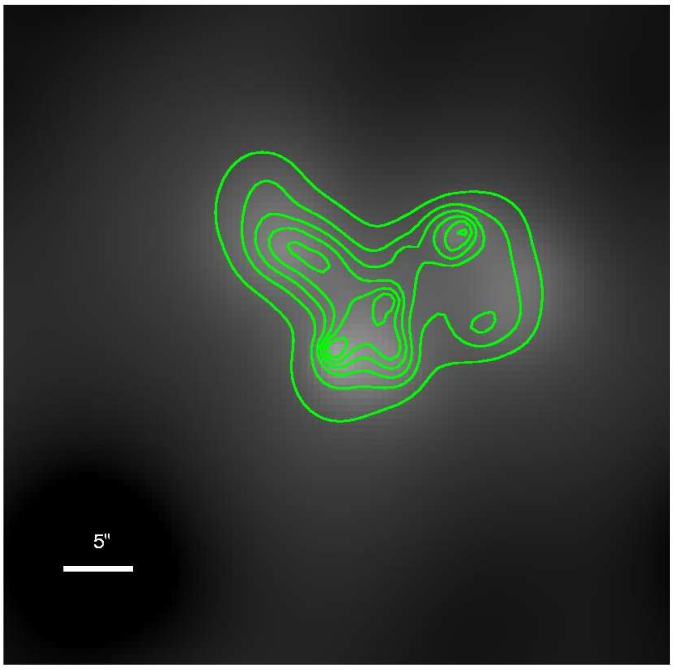

Figure 2.7: Metallicity-contour overlay of the diffuse emission of NGC 6240. This shows adaptively smoothed oxygen emission image (0.5-0.7 keV, gray) with iron (0.7-1.1 keV, contours). Contour levels are drawn at 0.0049, 0.049, 0.112, 0.199, 0.322, 0.494, 0.736, and 1.074 $\times$ 10^{-3} counts s^{-1} $arcsec^{-2}$. The white bar represents 5".

2.3 Spectral analysis

After revealing the energy-dependent X-ray morphology of NGC 6240 and spatially identifying different components in distinguishable regions, *Chandra* high spatial resolution imaging spectroscopy is used to resolve the spatial variations in the spectral features of X-ray emission and analyze the spectroscopically complex emission of the galaxy. We are no longer limited to only fitting spectra of the entire galaxy emission, which is a sum of a lot of different components including all diffuse emission and AGNs emission. We made use of the spatial information yielded by *Chandra* to construct suited models for the spectra of the spatially resolved regions and fit these spectra separately.

2.3.1 Spectral fitting descriptions

Based on the spatial features revealed in the imaging analysis, a systematical method for the spectral analysis is adopted to determine the properties of X-ray multi-components of NGC 6240. Considering the spectral complexity of X-ray emission (e.g. multi-components do spatially overlap in the central region of NGC 6240), the spectral analysis should begin with the simple halo component, which only consists of one component. After well determining the spectral properties of the halo emission, systematical spectral analysis of the inner components can be carried out proceeding towards more central areas, such that each component can be identified in the spectral

fitting. Such spectral decomposition is essential to study the physical nature of the individual components. This systematical method is also a prerequisite for avoiding unphysical, yet statistically acceptable fitting of the complex spectra.

A schematic illustration is shown in Figure 2.8 to clarify this method: two active galactic nuclei and the "jet-like" structure (red) are enclosed by "butterfly-shaped", extended diffuse emission (blue); in addition, a weak outspread halo component (yellow) with low surface brightness exists outside the diffuse emission. Along our line of sight, the outer halo component can be observed alone in the areas distant from the center (e.g. $\geq$ 14 kpc or $20''$) without being affected by radiation of the inner components. In contrast, the more central areas, such as bright extended emission and two nuclei, are observed together with the halo component, since the photons of these components penetrate the halo region before they are "captured" by *Chandra*.

In the spectral analysis, a large annular source-free region, surrounding the halo region and centered on the nuclei is used for the background.

Spectral models

Previous observational results from starbursts as well as AGNs prompt the physical models we will apply to spectral data. Here, I give a brief description of the models I consider, and the detailed applications are depicted in the following sections.

X-ray emission from starbursts includes both thermal and non-thermal components. Diffuse thermal plasma mainly contributes at soft X-rays. On the assumption of collisional ionization equilibrium (CIE), one of the commonly used thermal plasma models to fit the soft X-ray components of superwinds is the MEKAL model in XSPEC. With a solar abundance photoelectric absorption model (Morrison & McCammon 1983), the thermal plasma model is determined by the following parameters: equivalent hydrogen column density $N_{\rm H}$, plasma temperature kT, metal abundances relative to solar abundances[10] ($Z_{\odot}$) and normalization. The VMEKAL model allows us to consider variations in metal abundances for thermal plasma. The non-thermal components are due to the X-ray binaries, which produce power-law continuum in hard X-rays.

The mean X-ray continuum of AGNs was best modelled by a power-law with photon index $\Gamma \sim 1.9$ (Nandra & Pounds 1994), which is determined by *Ginga* observations for Seyfert galaxies, assuming the Seyfert 1 and 2 galaxies contain identical nuclei (Antonucci & Miller 1985). In the recent X-ray spectral survey with *XMM-Newton* of nearby Seyfert galaxies taken from the Ho et al. (1997) sample, Cappi et al. (2006) present the results of 27 Seyfert galaxies (9 of Seyfert 1, 18 of Seyfert 2) and find the values of the power-law indices of 1.56$\pm$0.04 for Seyfert 1s and 1.61$\pm$0.06 for Seyfert 2s. From a detailed X-ray spectral analysis of a sample at higher redshifts using *XMM-Newton*, Mateos et al. (2005) obtain the best-fit average spectral power-law index to be 1.89$\pm$0.03 for Seyfert 1 and 1.71$\pm$0.03 for Seyfert 2. In this analysis, I adopt the most commonly used value of $\Gamma = 1.9$ for the photon index of the intrinsic power-law component.

The existence of the heavily obscured AGNs can be inferred from the presence of a strong Fe Kα line complex around 6.4 keV and a reflection spectrum. In this case, the

[10] Abundances in XSPEC are from Anders & Grevesse (1989).

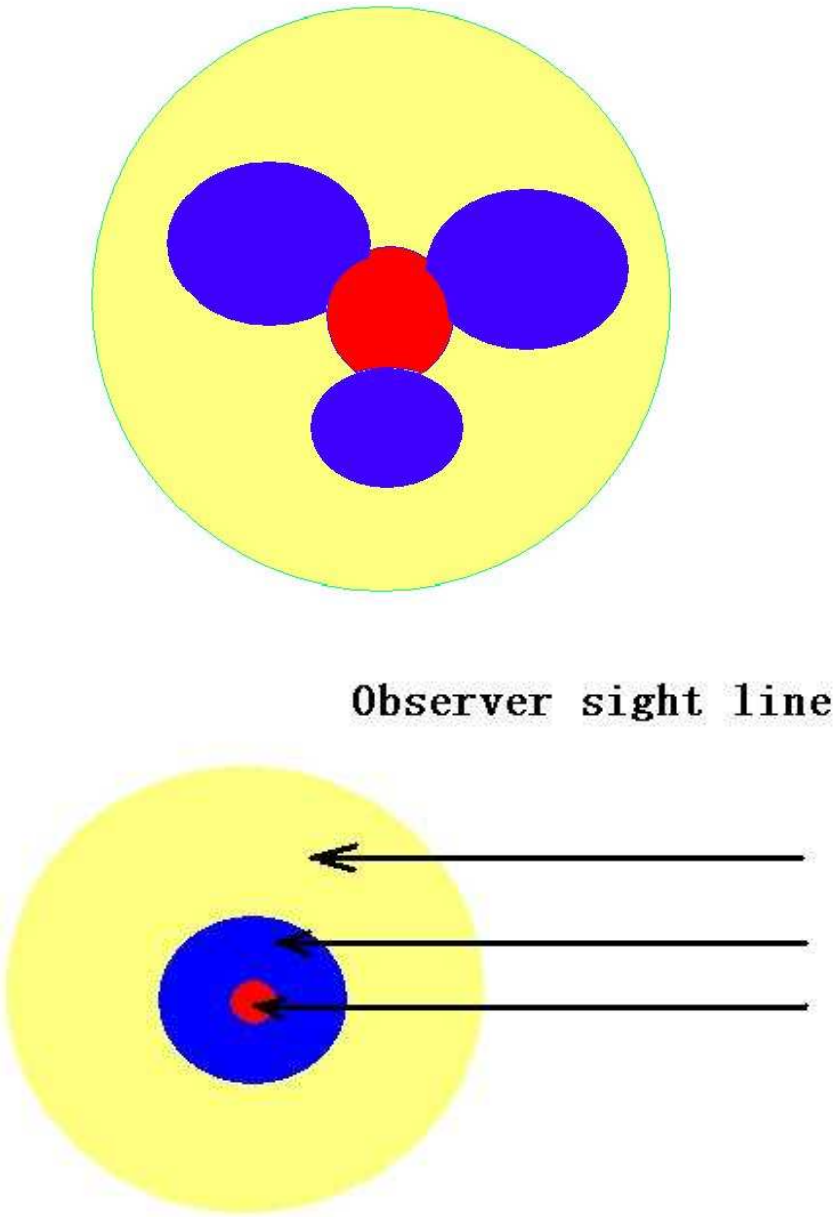

Figure 2.8: A schematic illustration of multi-component emission in NGC 6240 (see the text for details).

spectra become flat and much more complex than a single absorbed power-law, and the photo-electric cutoff does not quantify the *real* nuclear absorption any longer. In the XSPEC spectral fitting package, the PEXRAV model is available to describe the spectra reflected from neutral, optically thick material (Magdziarz & Zdziarski 1995). We fix some parameters to the default typical values: the abundances are assumed to be the solar abundances; the cosine of inclination angle is set to 0.45; and the cutoff energy is frozen at 100 keV. The reflection scaling factor R is set to be the free parameter, which indicates the relative amount of reflection compared to the directly-viewed intrinsic power-law. Since PEXRAV does not include any line emission, a Gaussian model is included to model the neutral Fe Kα line at 6.4 keV, (Mushotzky et al. 1993 and references therein). The width of the Gaussian is usually fixed at 0.01 keV and the normalization is allowed to vary.

2.3.2 Halo emission

As mentioned in Section 2.2, at larger radii, Figure 2.2 shows a low surface brightness halo in the region surrounding bright "butterfly-shaped" emission. The photons of this halo emission were extracted from an annulus region which is defined in Section 2.2.2. Spectral fitting was only performed to data within the energy band 0.5-2.5 keV, given the count rates for halo region are extremely low at higher energies (see Table 2.1). Had I included the spectral data at higher energies in spectral fitting of the halo component, I would have gotten lower values of the best-fit reduced χ^2. Excluding spectral data outside the energy range of 0.5-2.5 keV is appropriate in order to maintain an adequate S/N for the spectral fitting.

The spectrum of the halo component can be fitted by a thermal plasma model MEKAL. The column density is frozen at the Galactic Column Density[11] $N_{\rm H,Gal}$= $5.78\times10^{20}{\rm cm}^{-2}$, since it is not well constrained with the present spectral data. If the metal abundance was initialized by solar abundance, reduced $\chi^2 = 1.59$ was obtained. From the fitting, I found the spectral data of the halo component are sensitive to the parameter of metal abundances. Allowing the abundance to vary did substantially improve the fitting with $\chi^2_{red} = 1.07$ (for 63 d.o.f.). The best-fit abundance is low, with $\mathbf{Z} = 0.10^{+0.06}_{-0.04}$ Z$_\odot$, and the fitted temperature is $k\mathbf{T}= 0.61^{+0.04}_{-0.06}$ keV (see Table 2.3 and Figure 2.9). The flux calculated from this best-fit model is 2.0×10^{-13} ergs cm^{-2} s^{-1}. This corresponds to a luminosity $L_X = 4.8 \times 10^{41}$ ergs s^{-1}.

Before the spectral fitting is performed systematically inwards for more central regions, the investigation of spatial homogeneity for the halo area should be carried out. Only if the halo emission is spatially constant throughout the complete halo area, the best-fit model can be fixed when turning systematically to inner components.

To investigate whether the halo emission is spatially constant, I divided the complete halo area into three rings. The inner and outer radii for each ring are shown in Table 2.3. The background region is the same as for the complete halo region.

The single-temperature spectral model MEKAL provided statistically acceptable fits to the spectra of three rings (see Table 2.3). Fitted temperatures were typically kT$\sim$0.6 keV, the extremes being 0.53 keV and 0.65 keV. Best-fit metal abundances are

[11] http://heasarc.gsfc.nasa.gov/docs/tools.html

always low, typically $\mathbf{Z} = 0.10\ Z_{\odot}$. Note that they are very similar to the temperature and metal abundance of the complete halo component. Given the lack of significant spatial variation for the halo emission, the spectral properties can be reasonably assumed to be constant. In our spectral analysis, since the outspread halo component is assumed to be projected onto the inner regions, the best-fit temperature $kT \sim 0.6$ keV and metal abundance $\mathbf{Z} = 0.10\ Z_{\odot}$ of the halo component were fixed for the remainder of the spectral analysis. We noted that the normalization per square arcsec (the ratio of Normalization to Area, in Table 2.3, hereafter Norm/Area) of Ring 1 is about 4 times larger than Ring 2, and 8 times larger than Ring 3; i.e. the Norm/Area ratio is increasing from the outermost ring (Ring 3) towards the innermost ring (Ring 1). For one side, the Norm/Area is a measured quantity which is a projection of the gas sphere of the halo component onto the detector area, and therefore there is an increase in Norm/Area of the different sections of the sphere. On the other side, the normalization is proportional to the volume integral of the square of the density, and thus the increased Norm/Area may be also related with the increase density in the halo region. Though I can not draw any strong conclusion based on only three points, Table 2.3 suggests a trend between the values of Norm/Area and the distances from the halo rings to the center of NGC 6240.

Table 2.3: Spectral model fits to the halo emission of NGC 6240. Col.(1): Region name. Ring 1, 2 and 3 have been split off from the complete halo region. See text for details. Col.(2) and (3): The inner and outer radii of annuli. Col.(4): Total area, in units of arcsec^2. Col.(5) Gas temperatures in keV. Col.(6) Metal abundance relative to the Anders & Grevesse 1989 solar abundance. Col.(7): Model component normalization. where $K = (10^{-14}/(4\pi(D_A(1+z))^2)) \int n_e n_H dV$. D_A is the angular size distance to the source (cm), n_e and n_H are the electron and H densities (cm^{-3}). Col.(8): Fit statistics: the reduced χ^2 (χ^2_{red}) and the number of degrees of freedom.

Region	Inner Radius	Outer Radius	Area	kT	**Z**	K	χ^2_{red} (d.o.f.)
(1)	(2)	(3)	(4)	(5)	(6)	(7)	(8)
The complete halo	20″	60″	10054.595	$0.58^{+0.04}_{-0.06}$	$0.10^{+0.06}_{-0.04}$	$3.95^{+1.19}_{-0.90}$E-4	1.07(63)
Ring 1	20″	34″	2375.234	$0.53^{+0.09}_{-0.06}$	$0.06^{+0.07}_{-0.03}$	$3.42^{+1.23}_{-1.38}$E-4	0.98(41)
Ring 2	34″	48″	3607.080	$0.56^{+0.07}_{-0.09}$	$0.13^{+0.19}_{-0.07}$	$1.29^{+1.06}_{-1.29}$E-4	0.61(34)
Ring 3	48″	60″	4072.272	$0.65^{+0.08}_{-0.08}$	$0.13^{+0.07}_{-0.07}$	$6.62^{+6.18}_{-6.62}$E-5	1.08(31)

2.3.3 Three loops: Region 1, 2 and 3

The intensity images (Figure 2.2 and 2.3) show that models of emission from three giant loops or bubbles (Region 1, 2 and 3) with brighter surface brightness requires additional components, in addition to the projected halo component. The temperature and metal abundances of the halo component are fixed at 0.6 keV and 0.1 $\mathbf{Z}_{\odot}$, respectively. The additional components are most likely to be from the starburst emission, related with the starburst-driven superwinds. Thus, the composite model of emission from Region 1, 2 and 3 can be written as:

$$wabs_{gal} * [\ \underbrace{mekal_{halo}}_{Halo\ component} + \underbrace{wabs_R * model_R}_{individual\ Region\ components}\ ],$$

where wabs_{gal} is the absorption of the halo component (fixed to the Galactic column density $N_{\mathrm{H,Gal}}$), mekal_{halo} denotes the halo MEKAL component, wabs_R is the fitted intrinsic absorption, and Model_R represents the additional component(s) contributed from Region 1, 2 and 3. More detailed descriptions of the Model_R are described as follow.

Thermal model fits

At the beginning of the spectral analysis, a single-temperature thermal plasma code (VMEKAL) is considered, that means

$$Model_R = vmekal.$$

The VMEKAL model allows us to search for variations in metal abundances. Due to the spectral resolution of the present data and the weakness of unresolved emission lines, it is rather hard to constrain many of the elemental abundances. Oxygen and iron abundances are likely to be the best constrained in *Chandra* ACIS spectra of soft thermal X-ray emission. Following Strickland et al. (2004), I tied metal abundance of Mg, Si, Ne, S and Ar with respect to hydrogen to tract the fitted O abundance, and referred to this set of elements as α-elements $\mathbf{Z}_{\alpha}$. I also constrained the Fe abundance to Ni, Ca, Al and Na and referred to $\mathbf{Z}_{Fe}$.

I note that the normalizations or the values of Norm/Area of the projected component can not be well determined for the inner regions. And they have a significant interaction with the parameters of other components, for example, the parameters of the thermal component. The closer to the center, the larger the values of Norm/Area. Thus the Norm/Area of Ring 1 (see Section 2.3.2) could be taken as the lower limit of Norm/Area of three loops. In the spectral fitting, the values of Norm/Area of the projected halo component for Region 1, 2 and 3 are assumed to be 1, 4, 6, and 8 times of the Norm/Area of Ring 1, named after Case I, II, III, IV. The spectral results are given in Table 2.4, 2.5, and 2.6. However, none of them supplied acceptable fits. Substantial positive residuals are obvious at the hard X-ray band (above 2 keV) of the spectra of three regions, which indicates more components are required by the spec-

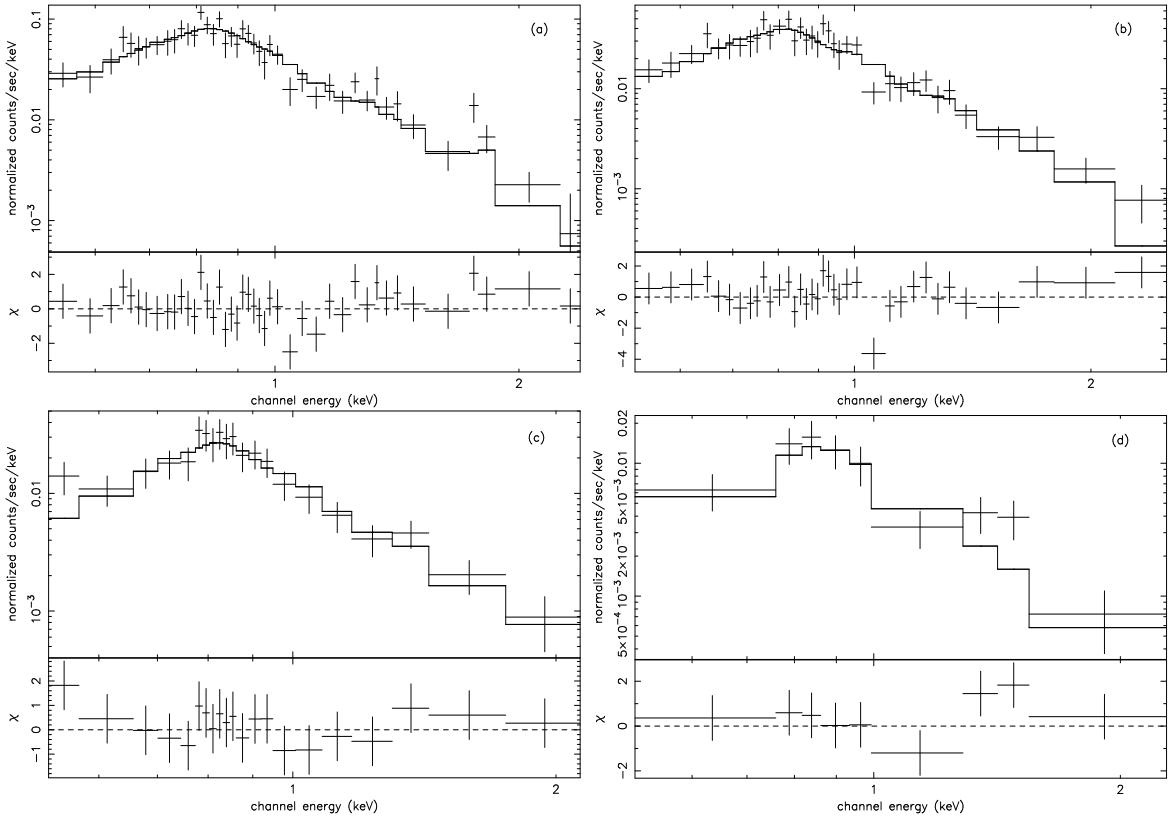

Figure 2.9: The best spectral model fits to the halo spectra of NGC 6240. There are four 2-panel data plots: (a) for the complete halo, (b) for Ring 1, (c) for Ring 2, and (d) for Ring 3. Each data plot has a logarithmic x-axis of channel energy in units of keV. The upper panel of each data plot illustrates the data (the crosses) and the folded model (the solid line) with a logarithmic y-axis in units of count rates per keV. The horizontal bars of the crosses show how the bins are added together in the plots. Bins in the plots are combined until they have a significant detection at least as large as 3σ, but no more than 50 bins are combined. The vertical bars of the crosses represent the error bars in the measurements. To calculate the error bars, the default argument "quad" is used, which sums in quadrature the errors on the original bins. In order to indicate the deviations of data from the model, every lower panel plots the residuals in terms of sigmas with bars of size one.

Table 2.4: Thermal model fits to Region 1 of NGC 6240. Col.(1): Case name. Four different cases fixed normalizations of the halo component given in Column (2) (see the text for more details). Col. (2): the assumed normailizations K_{halo} of the halo thermal component (mekal$_{halo}$), where K_{halo}=$(10^{-14}/(4\pi(D_A(1+z))^2))\int n_e n_H dV$. D_A is the angular size distance to the source (cm), n_e and n_H are the electron and H densities (cm^{-3}). Col.(3): The intrinsic hydrogen column density (wabs$_R$) for Region 1 in units of 10^{22} cm^{-2}. Col.(4): Gas temperatures for vmekal models in keV. Col.(5): $\mathbf{Z}_\alpha$ refers to the abundance of the oxygen group, relative to the Anders & Grevesse 1989 solar abundance. Col.(6): $\mathbf{Z}_{Fe}$ refers to that of the iron group. Col.(7): The normalizations K_{vmekal} of the VMEKAL model. Col.(8): Fit statistics: reduced χ^2 (χ^2_{red}). The number of degrees of freedom (d.o.f.) is 82.

Case	K_{halo}	$N_{\rm H}$	$k{\rm T}_{vmekal}$	$\mathbf{Z}_\alpha$	$\mathbf{Z}_{Fe}$	K_{vmekal}	χ^2_{red}
(1)	(2)	(3)	(4)	(5)	(6)	(7)	(8)
I	2.30E-5	$0.08^{+0.04}_{-0.08}$	$1.38^{+1.52}_{-0.13}$	$0.32^{+0.17}_{-0.22}$	$0.05^{+0.04}_{-0.04}$	$4.65^{+1.00}_{-2.60}$E-4	1.99
II	9.20E-5	$0.15^{+0.02}_{-0.15}$	$1.41^{+2.19}_{-0.11}$	$0.33^{+0.22}_{-0.11}$	$0.04^{+0.04}_{-0.04}$	$4.64^{+0.46}_{-2.25}$E-4	1.74
III	1.40E-4	$0.24^{+0.05}_{-0.24}$	$1.32^{+1.92}_{-0.07}$	$0.41^{+0.18}_{-0.28}$	$0.06^{+0.04}_{-0.06}$	$4.62^{+0.71}_{-2.73}$E-4	1.66
IV	1.84E-4	$0.35^{+0.11}_{-0.34}$	$1.31^{+2.62}_{-0.05}$	$0.45^{+0.18}_{-0.31}$	$0.09^{+0.05}_{-0.09}$	$4.66^{+0.74}_{-2.97}$E-4	1.58

tral data. Thus, the single-phase thermal plasma models can not provide statistically unacceptable fits to the spectra of Region 1, 2 and 3.

Numerical models of superwinds by Suchkov et al. (1994) predict that the observed hard X-ray emission from starbursts is not associated with the thermal emission. Strickland & Stevens (2000) reiterate that thermal plasma with high temperatures (above 3 keV) has low density and it can not radiate effectively. Strickland et al. (2000) further emphasize the very hot components of starburst driven superwinds may be difficult to detect. Taken together, the X-ray emission at higher energies from starbursts is not due to thermal emission from the starburst-driven superwinds (Strickland et al.2000). Therefore, it is most likely that the non-thermal component contributes to the hard X-ray emission from starbursts (see below for more details).

Thermal plus non-thermal model fits

Persic & Raphaeli (2002) have quantitatively assessed the systematic studies of X-ray emission of starburst galaxies and revealed that X-ray binaries are the main contributors in the 2-10 kev energy range. This suggests that the hard components of starburst galaxies may result from the integrated emission of X-ray binaries. Since the "butterfly-shaped" extended emission of NGC 6240 is related with superwinds driven by starbursts, it is possible that many X-ray binaries are "hidden" in thermal plasma and not detected. The upper limit of the luminosities of such "hidden" point-like sources is estimated in Section 2.4.3. Here, I assumed the hard emission above 2 keV is due to the contribution of undetected X-ray binaries to the integrated spectrum.

Table 2.5: Thermal model fits to Region 2 of NGC 6240. Col.(1)-(8): Columns are the same as in Table 2.4 The number of degree of freedom (d.o.f.) is 63.

Case	K_{halo}	$N_{\rm H}$	$k{\rm T}_{vmekal}$	$\mathbf{Z}_{\alpha}$	$\mathbf{Z}_{Fe}$	K_{vmekal}	χ^2_{red}
(1)	(2)	(3)	(4)	(5)	(6)	(7)	(8)
I	2.30E-5	$0.12^{+0.03}_{-0.10}$	$0.86^{+0.35}_{-0.08}$	$0.62^{+0.31}_{-0.50}$	$0.15^{+0.02}_{-0.10}$	$3.11^{+0.61}_{-0.72}$E-4	1.55
II	9.20E-5	$0.11^{+0.04}_{-0.06}$	$1.05^{+0.08}_{-0.09}$	$0.62^{+0.27}_{-0.22}$	$0.16^{+0.05}_{-0.05}$	$2.59^{+0.21}_{-0.22}$E-4	1.27
III	1.40E-4	$0.13^{+0.03}_{-0.08}$	$1.32^{+0.04}_{-0.38}$	$0.54^{+0.73}_{-0.24}$	$0.19^{+0.10}_{-0.09}$	$2.38^{+1.57}_{-0.25}$E-4	1.26
IV	1.84E-4	$0.18^{+0.06}_{-0.09}$	$1.41^{+0.10}_{-0.48}$	$0.67^{+1.38}_{-0.25}$	$0.26^{+0.11}_{-0.12}$	$2.06^{+1.94}_{-0.29}$E-4	1.25

Table 2.6: Thermal model fits to Region 3 of NGC 6240. Col.(1)-(8): Columns are the same as in Table 2.4 The number of degree of freedom (d.o.f.) is 70.

Case	K_{halo}	$N_{\rm H}$	$k{\rm T}_{vmekal}$	$\mathbf{Z}_{\alpha}$	$\mathbf{Z}_{Fe}$	K_{vmekal}	χ^2_{red}
(1)	(2)	(3)	(4)	(5)	(6)	(7)	(8)
I	1.15E-5	$0.07^{+0.01}_{-0.07}$	$1.18^{+0.20}_{-0.36}$	$0.22^{+0.42}_{-0.13}$	$0.09^{+0.04}_{-0.03}$	$4.20^{+0.33}_{-1.20}$E-4	1.92
II	4.60E-5	$0.14^{+0.02}_{-0.13}$	$1.06^{+0.34}_{-0.16}$	$0.40^{+0.37}_{-0.19}$	$0.10^{+0.04}_{-0.06}$	$4.03^{+1.37}_{-1.13}$E-4	1.81
III	6.90E-5	$0.15^{+0.03}_{-0.12}$	$1.03^{+0.39}_{-0.08}$	$0.50^{+0.14}_{-0.27}$	$0.10^{+0.05}_{-0.06}$	$3.68^{+0.53}_{-1.17}$E-4	1.76
IV	9.20E-5	$0.17^{+0.03}_{-0.15}$	$1.08^{+0.63}_{-0.12}$	$0.48^{+0.55}_{-0.25}$	$0.11^{+0.05}_{-0.08}$	$3.66^{+1.25}_{-1.46}$E-4	1.74

A simple, spectrally hard power-law component was introduced to represent X-ray emission of X-ray binaries, since it shows no prominent line emission.

Thus, the thermal component (VMEKAL) provides the observed line emission, while the non-thermal (power-law) component accounts for much of the continuum at energies higher than 3 keV. So the composite model of $Model_R$ can be expressed as:

$$Model_R = vmekal + pl.$$

Again, the temperature and metal abundances of the halo component that is assumed to be projected onto the three loop regions, are fixed at 0.6 keV and 0.1 $\mathbf{Z}_{\odot}$, respectively. As mentioned above, the normalizations of this halo component have significant interaction with other parameters, such as intrinsic absorptions, temperatures and abundances of VMEKAL model, etc., (Once again, the values of Norm/Area of the projected halo component for Region 1, 2 and 3 are assumed to be 1, 4, 6, and 8 times of the Norm/Area of Ring 1 in the spectral fitting, named after Case I , II, III and IV.) The lower normalizations of the projected halo component (K_{halo} in Table 2.7, 2.8, and 2.9) are simply compensated by lower temperatures ($k\mathrm{T}_{vmekal}$) and higher normalizations of VMEKAL (K_{vmekal}). K_{halo} also have an effect on the fitting results of intrinsic absorption and the parameters of the power-law components. For example, trade-off between the normalizations of the halo component and the parameters of other components for Case I and III of Region 3 (see Table 2.9) is illustrated in Figure 2.10. Taken at face value, it is hard to distinguish Case I from Case III from spectral results.

In summary, X-ray spectra data of Region 1, 2, and 3 require a hot thermal plasma component (VMEKAL model) plus a non-thermal power-law model. The hot thermal plasma component has a typical temperature between 0.8 and 1.2 keV. It should be considered as a simplification of the reality, which is probably more complicated, with a multi-temperature medium (Strickland & Stevens 2000) accounting for soft X-ray emission at energies E$\leq$ 2 keV. Taken as a whole, the derived intrinsic hydrogen column densities, $\mathbf{Z}_{\alpha}/\mathbf{Z}_{Fe}$, and the temperatures of VMEKAL models, are found to be similar for the spectral fits of Region 1, 2, and 3. The X-ray derived column density lies in between 1.0 and 3.0$\times$ 10^{21} cm^{-2}. According to optical measurements of the extinction towards the extended regions (including R1, 2, and 3) of $\mathrm{A}_V \sim 1$ mag (Thronson et al. 1990), I estimated the expected column density $N_{\mathrm{H}} \sim 2.0\times$ 10^{21} cm^{-2}, by using the relation between N_{H} and A_V (Bohlin et al. 1978). The X-ray derived column densities are roughly consistent with the expected column density N_{H} of the extended regions. The α-elements are comparatively more prominent than iron-group elements for Region 1, 2 and 3. The measured value of $\mathbf{Z}_{\alpha}/\mathbf{Z}_{Fe}$ lies in the range between 3.1 and 5.2 $\mathbf{Z}_{\alpha,\odot}/\mathbf{Z}_{Fe,\odot}$. For the non-thermal power-law components, the extremes of best-fit photon indices yielded by this composite model fits are between 1.0 and 1.6. The more detailed X-ray properties of thermal and non-thermal components will be discussed in Section 2.4.2. The model-derived absorption-corrected X-ray fluxes and luminosities for the fits of Case IV for Region 1, 2 and 3 are given in Table 2.10, and spectra are shown in Figure 2.11, 2.12, and 2.13, since for each region Case IV provides better or compatible fits.

Table 2.7: Thermal (vmekal) plus nonthermal (power-law) model fits to Region 1 of NGC 6240. Col.(1): Case name. Four different cases fixed normalizations of the halo component given in Column (2) (see the text). Col.(2): The assumed normalizations K_{halo} of the halo thermal component (mekal$_{halo}$), where K_{halo}=$(10^{-14}/(4\pi(D_A(1+z))^2))\int n_e n_H dV$. D_A is the angular size distance to the source (cm), n_e and n_H are the electron and H densities (cm^{-3}). Col.(3): The intrinsic hydrogen column density (wabs$_R$) for Region 1 in units of 10^{22} cm^{-2}. Col.(4): Gas temperatures for vmekal models in keV. Col.(5): $\mathbf{Z}_\alpha$ refers to the abundance of the oxygen group, relative to the Anders & Grevesse 1989 solar abundance. Col.(6): $\mathbf{Z}_{Fe}$ refers to that of the iron group. Col.(7): The normalizations K_{vmekal} of the VMEKAL model. Col.(8) is the photon index of the power-law Γ, where $F \propto E^{-\Gamma}$. Col.(9): The power-law normalization K_{PL} in units of photons s^{-1} keV^{-1} cm^{-2} at E = 1keV. Col.(10): Fit statistics: reduced χ^2 (χ^2_{red}) and the number of degrees of freedom.

Case	K_{halo}	$N_{\rm H}$	$k\Gamma_{vmekal}$	$\mathbf{Z}_\alpha$	$\mathbf{Z}_{Fe}$	K_{vmekal}	Γ	K_{PL}	χ^2_{red} (d.o.f.)
(1)	(2)	(3)	(4)	(5)	(6)	(7)	(8)	(9)	(10)
I	2.30E-5	$0.10^{+0.17}_{-0.03}$	$0.93^{+0.07}_{-0.37}$	$0.31^{+0.23}_{-0.12}$	$0.07^{+0.02}_{-0.05}$	$4.15^{+2.40}_{-0.44}$E-4	$1.17^{+1.51}_{-0.27}$	$1.59^{+3.55}_{-0.39}$E-5	1.23(80)
II	9.20E-5	$0.14^{+0.16}_{-0.05}$	$1.01^{+0.09}_{-0.36}$	$0.46^{+0.27}_{-0.18}$	$0.09^{+0.03}_{-0.06}$	$3.40^{+1.18}_{-0.48}$E-4	$1.13^{+1.30}_{-0.21}$	$1.46^{+2.45}_{-0.44}$E-5	1.19(80)
III	1.38E-4	$0.20^{+0.25}_{-0.08}$	$1.11^{+0.14}_{-0.47}$	$0.47^{+0.36}_{-0.31}$	$0.09^{+0.09}_{-0.06}$	$3.35^{+2.28}_{-0.65}$E-4	$1.10^{+1.38}_{-0.25}$	$1.26^{+3.31}_{-0.86}$E-5	1.09(80)
IV	1.84E-4	$0.25^{+0.44}_{-0.07}$	$1.21^{+0.11}_{-0.67}$	$0.53^{+0.46}_{-0.37}$	$0.12^{+0.16}_{-0.08}$	$3.08^{+0.43}_{-2.17}$E-4	$1.07^{+1.42}_{-0.84}$	$1.18^{+0.42}_{-0.78}$E-5	1.06(80)

Table 2.8: Thermal (vmekal) plus non-thermal (power-law) model fits to Region 2 of NGC 6240. Col.(1)-(10): Columns are the same as in Table 2.7.

Case	K_{halo}	$N_{\rm H}$	$k{\rm T}_{vmekal}$	$\mathbf{Z}_{\alpha}$	$\mathbf{Z}_{Fe}$	K_{vmekal}	Γ	K_{PL}	χ^2_{red} (d.o.f.)
(1)	(2)	(3)	(4)	(5)	(6)	(7)	(8)	(9)	(10)
I	2.30E-5	$0.11^{+0.04}_{-0.07}$	$0.83^{+0.07}_{-0.12}$	$0.61^{+0.33}_{-0.29}$	$0.16^{+0.04}_{-0.06}$	$2.65^{+0.55}_{-1.33}$E-4	$1.56^{+0.72}_{-0.41}$	$1.10^{+2.18}_{-0.30}$E-5	0.95(61)
II	9.20E-5	$0.10^{+0.07}_{-0.06}$	$0.97^{+0.09}_{-0.23}$	$0.61^{+0.59}_{-0.31}$	$0.17^{+0.06}_{-0.09}$	$2.29^{+0.61}_{-0.98}$E-4	$1.15^{+1.28}_{-0.66}$	$4.97^{+11.97}_{-3.53}$E-6	0.94(61)
III	1.38E-4	$0.15^{+0.08}_{-0.07}$	$0.99^{+0.10}_{-0.16}$	$0.91^{+0.69}_{-0.47}$	$0.23^{+0.10}_{-0.11}$	$1.76^{+0.54}_{-0.84}$E-4	$1.20^{+1.18}_{-0.56}$	$5.56^{+12.04}_{-4.60}$E-6	0.89(61)
IV	1.84E-4	$0.28^{+0.14}_{-0.15}$	$1.00^{+0.08}_{-0.13}$	$0.92^{+1.42}_{-0.41}$	$0.30^{+0.30}_{-0.16}$	$1.82^{+0.91}_{-1.12}$E-4	$1.18^{+1.02}_{-0.90}$	$5.28^{+11.02}_{-4.80}$E-6	0.89(61)

Table 2.9: Thermal (vmekal) plus nonthermal (power-law) model fits to Region 3 of NGC 6240. Col.(1)-(10): Columns are the same as in Table 2.7.

Case	K_{halo}	$N_{\rm H}$	$k\Gamma_{vmekal}$	$\mathbf{Z}_{\alpha}$	$\mathbf{Z}_{Fe}$	K_{vmekal}	Γ	K_{PL}	χ^2_{red} (d.o.f.)
(1)	(2)	(3)	(4)	(5)	(6)	(7)	(8)	(9)	(10)
I	1.15E-5	$0.13^{+0.05}_{-0.10}$	$0.77^{+0.12}_{-0.09}$	$0.42^{+0.43}_{-0.14}$	$0.10^{+0.06}_{-0.04}$	$3.93^{+0.67}_{-1.77}$E-4	$1.18^{+0.50}_{-0.50}$	$1.04^{+0.40}_{-0.73}$E-5	1.05(68)
II	4.60E-5	$0.14^{+0.05}_{-0.09}$	$0.82^{+0.14}_{-0.10}$	$0.46^{+0.47}_{-0.18}$	$0.11^{+0.05}_{-0.05}$	$3.49^{+0.74}_{-1.71}$E-4	$1.11^{+0.56}_{-0.48}$	$0.93^{+0.47}_{-0.53}$E-5	1.04(68)
III	6.90E-5	$0.13^{+0.08}_{-0.07}$	$0.87^{+0.13}_{-0.14}$	$0.50^{+0.40}_{-0.22}$	$0.11^{+0.04}_{-0.05}$	$3.12^{+0.70}_{-1.34}$E-4	$1.02^{+0.66}_{-0.57}$	$0.79^{+0.21}_{-0.42}$E-5	1.04(68)
IV	9.20E-5	$0.16^{+0.06}_{-0.09}$	$0.85^{+0.17}_{-0.13}$	$0.51^{+0.51}_{-0.19}$	$0.11^{+0.09}_{-0.05}$	$3.14^{+0.86}_{-1.43}$E-4	$1.07^{+0.52}_{-0.47}$	$0.85^{+1.15}_{-0.53}$E-5	1.04(68)

Table 2.10: Observed X-ray fluxes and luminosities of Region 1, 2 and 3 in NGC 6240, derived from Case IV for each region.

	Flux			Luminosity		
	10^{-13} ergs cm^{-2} s^{-1}			10^{41} ergs s^{-1}		
Region	0.5-10keV	0.5-2keV	2.0-10keV	0.5-10 keV	0.5-2keV	2.0-10keV
1	4.78	2.93	1.85	11.19	6.86	4.33
2	3.59	2.86	0.72	8.40	6.69	1.69
3	3.84	2.61	1.23	8.99	6.11	2.88

2.3.4 The Extended Region

Based on the spectral analysis of Region 1, 2, and 3, the general spectral features of the complete extended region (see the definition in Section 2.2.2) is also explored. Figure 2.6 shows that the Extended Region encloses the inner 20″ region, excluding the two nuclei and the "jet-like" structure and including the three sub-regions (three loops: Region 1, 2, and 3).

As indicated above, the composite models including the projected halo MEKAL, the thermal VMEKAL and non-thermal power-law components, provided acceptable fits to the spectral data of Region 1, 2 and 3. Therefore, the sum of all the best-fit composite models (totally 9 components with individual column densities) of the three sub-regions should be mathematically added together, and considered as the combined spectral model of the complete extended region. The parameters, such as temperatures, metal abundances, and the photon indices are fixed at the best-fit values. Only the normalizations of each component are allowed to vary freely, since it is possible that some photons are lost because the regions for extraction do not border precisely. However, this combined model can not give an excellent description of the spectral data of the complete extended emission. For example, the positive residuals were clearly seen between 6 and 7 keV.

Next, I consider the additional component that is required by the data. Note that a number of X-ray photons at higher energies are located outside the two nuclear circles, which is probably due to the spread-out/scattered nuclear emission (see Section 2.2.2). So in addition to the multi-components of Region 1, 2 and 3, the spread-out/scattered nuclear emission also have contributions to the whole spectra. This component is considered to be fitted with an absorbed power-law model with photon index $\Gamma \sim 1.9$. The obvious excesses were clearly present between 6 and 7 keV when the spectra were fitted by a single power-law, indicating the presence of an iron line. A Gaussian line model is also added to represent this line-like feature.

On the whole, the combined spectral model of the complete extended region should be the sum of the projected halo component, all spectral components of the three sub-regions, and the spread-out/scattered nuclear emission component. Then, the

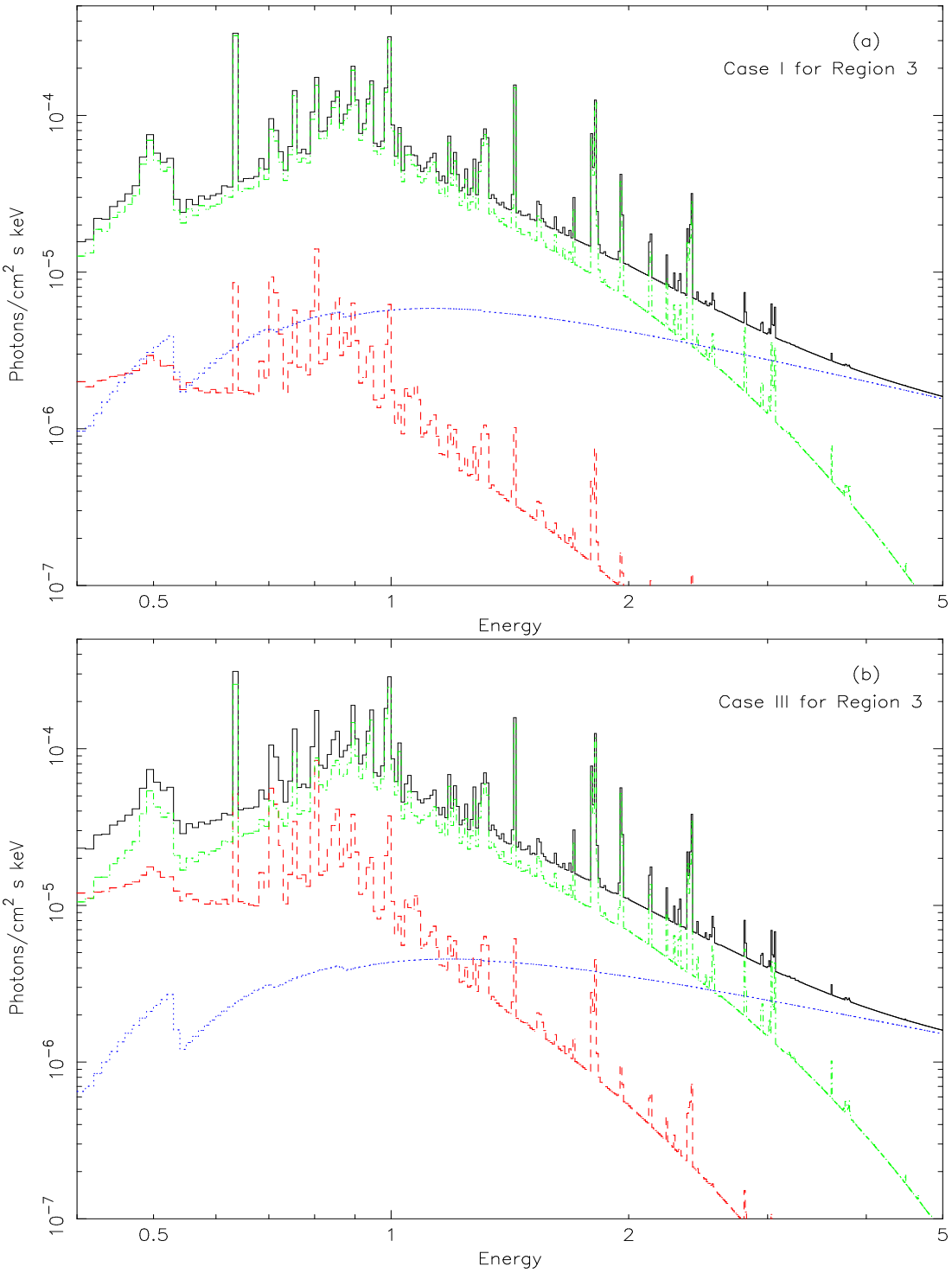

Figure 2.10: Trade-off between the normalization of the (projected) halo thermal component and the normalization and temperature of VMEKAL model for Region 3. The red, green and blue lines denote the halo thermal, VMEKAL model and power-law component, respectively, for two different cases in Table 2.9: (a) Case I and (b) Case III. For the resultant spectral fits, one is hard to be distinguished from the other.

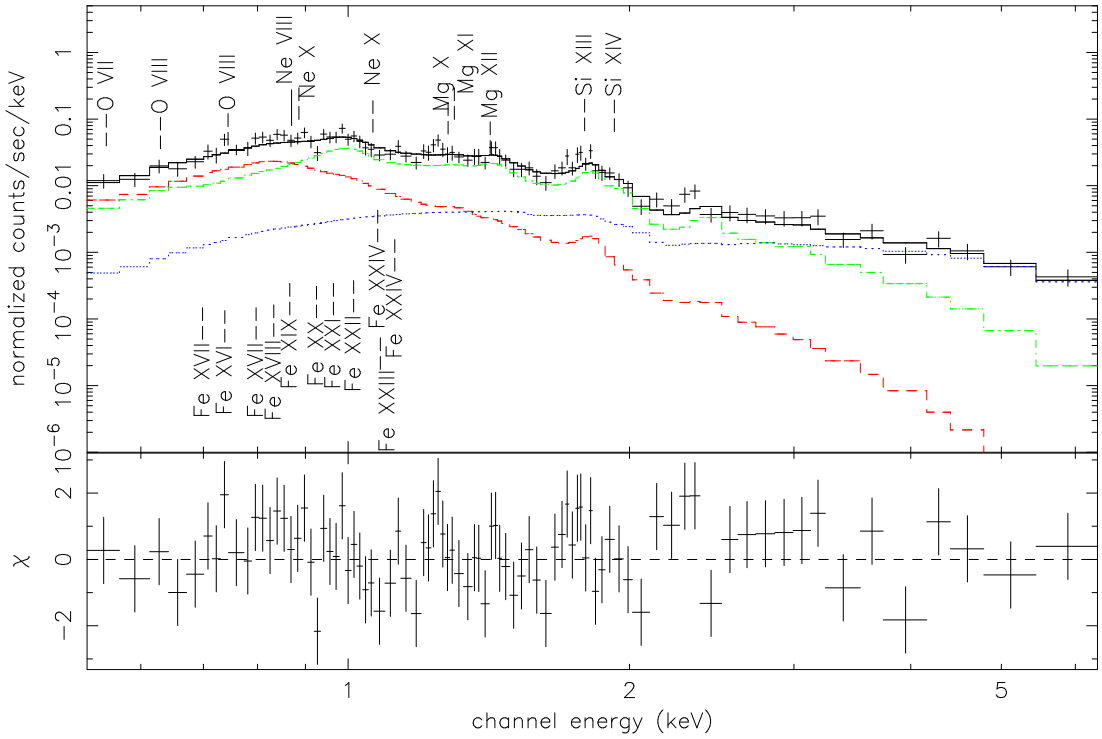

Figure 2.11: The spectrum of Region 1 of NGC 6240. The red, green and blue lines represent the halo thermal component, the VMEKAL model and power-law component, respectively. The energies of prominent lines of O, Ne, Mg, and Si are marked. The Fe L lines are largely blended around 1 keV.

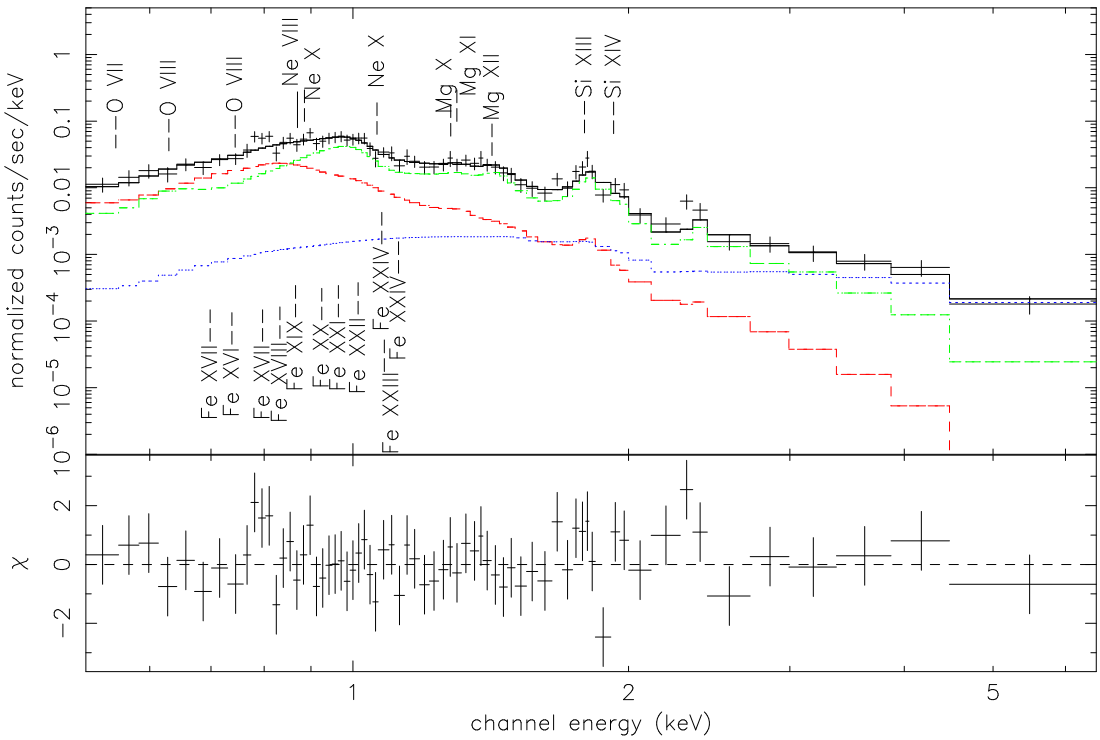

Figure 2.12: The spectrum of Region 2 of NGC 6240. The lines and marks are the same as in Figure 2.11.

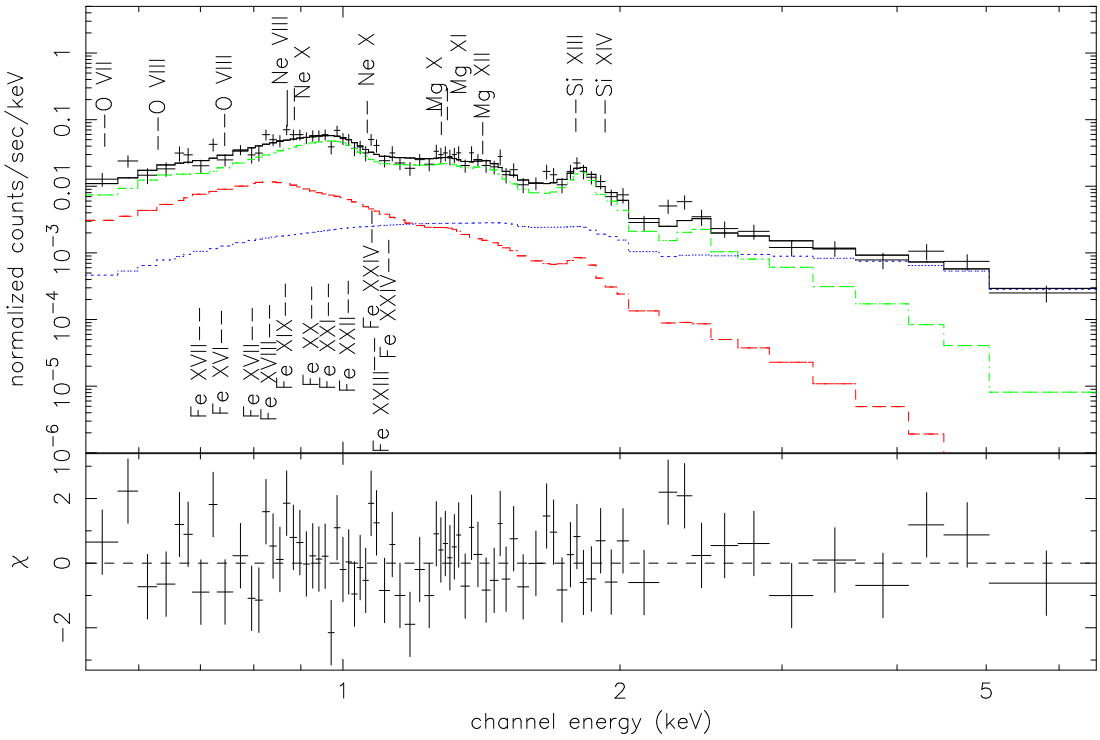

Figure 2.13: The spectrum of Region 3 of NGC 6240.The lines and marks are the same as in Figure 2.11.

combined spectral model can be written as:

$$wabs_{gal} * [\ \underbrace{mekal_{halo}}_{Halo\ component} + \underbrace{wabs_{R1}(vmekal_{R1} + pl_{R1})}_{Region\ 1\ components} +$$
$$\underbrace{wabs_{R2}(vmekal_{R2} + pl_{R2})}_{Region\ 2\ components} + \underbrace{wabs_{R3}(vmekal_{R3} + pl_{R3})}_{Region\ 3\ components} +$$
$$\underbrace{wabs_{s}(pl_{s} + zgauss)}_{Spread-out/scattered\ nuclear\ emission}\ ].$$

The line emission is located at a (redshift-corrected) energy E = $6.39^{+0.10}_{-0.07}$ keV (see Figure 2.14 and Table 2.11). The energy of the iron line is consistent with neutral Fe Kα emission. It backs up the speculation that the hard X-ray emission is due to spread-out/scattering of dense cold gas, since the strong 6.4 keV iron line observed here can not be produced by the starburst components and is only due to fluorescence.

The best-fit column density of the spread-out/scattered nuclear emission $N_{\rm H} \sim 10^{22}$ cm^{-2} corresponds to a reddening $A_V = 5$, which is consistent with the optical estimate for the central core of NGC 6240 (Thronson et al. 1990).

As a consistency check, I compared the best-fit normalizations of all the spectral components determined separately for the three sub-regions in Section 2.3.3 with the corresponding normalizations derived from the combined spectral fitting for the complete extended region in this sub-section. As I expected, there are two differences: (1) for the halo component, the sum of the normalizations of all the halo MEKAL components projected onto Region 1, 2 and 3 (calculated from Case IV in Table 2.7, 2.8, and 2.9), is lower than the normalization of the halo MEKAL component projected onto the complete extended region (K_{halo} in Table 2.11). (2) for Region 1, 2 and 3 components, the normalizations of the VMEKAL and power-law models determined separately for Case IV in Table 2.7, 2.8, and 2.9, are a bit below the corresponding normalizations in Table 2.11. The main causes of the differences may be (1) the summed area of three sub-regions (Region 1, 2 and 3) is smaller than that of the complete extended region (see Table 2.1), and (2) the three sub-regions do not border precisely and then some photons are lost.

In general, the results presented here demonstrate that the combined spectral model gives a fair representation of the complete extended emission, and the combined spectral fit for complete extended emission is consistent with the previous spectral fits done separately for Region 1, 2 and 3.

2.3.5 The binary AGN emission

It has been repeatedly announced that the X-ray emission below 10 keV from the nuclei is scattered emission from the AGN (e.g. Mitsuda 1995; Schulz et al. 1998; Komossa et al. 1998; Iwasawa & Comastri 1998). The intrinsic AGN emission of NGC 6240 can be seen only at energies higher than 10 keV (Vignati et al. 1999; Ikebe et al. 2000).

Table 2.11: Spectral model fits to the Extended Region of NGC 6240, with χ^2_{red} (d.o.f.) = 1.14 (116). The combined spectral model of this complete region includes five component parts: (1) the projected halo component; (2) Region 1 components; (3) Region 2 components; (4) Region 3 components; and (5) the spread-out/scattered nuclear emission. All the parameters of the halo, Region 1, 2, and 3 components are fixed to the best-fit values which are previously determined, except the normalizations. The normalizations are allowed to vary freely. For the spread-out/scattered nuclear emission, the power-law photon index is fixed to 1.9 and the line width of the gaussian line is fixed to 0.01 keV.

Components	Fixed Parameters	Fitted Parameters
(1)	(2)	(3)
Halo component		
wabs	$N_{\rm H} = 5.78 \times 10^{20}$ cm^{-2}	
mekal	$k\Gamma_{halo} = 0.6$ keV	$K_{halo} = 6.59^{+0.59}_{-0.56}$E-4
	$\mathbf{Z} = 0.1\ \mathbf{Z}_{\odot}$	
Region 1 Components		
wabs	$N_{\rm H} = 0.25 \times 10^{22}$ cm^{-2}	
vmekal	$k\Gamma = 1.21$ keV	$K_{R1} = 5.02^{+0.68}_{-1.43}$E-4
	$\mathbf{Z}_{\alpha} = 0.53\ \mathrm{Z}_{\odot}$	
	$\mathbf{Z}_{Fe} = 0.12\ \mathrm{Z}_{\odot}$	
pl	$\Gamma = 1.07$	$K_{R1} = 2.04^{+0.74}_{-1.24}$E-5
Region 2 Components		
wabs	$N_{\rm H} = 0.28 \times 10^{22}$ cm^{-2}	
vmekal	$k\Gamma = 1.00$ keV	$K_{R2} = 2.00^{+0.58}_{-1.18}$E-4
	$\mathbf{Z}_{\alpha} = 0.92\ \mathrm{Z}_{\odot}$	
	$\mathbf{Z}_{Fe}$ - 0.30 $\mathrm{Z}_{\odot}$	
pl	$\Gamma = 1.18$	$K_{R2} = 1.05^{+0.85}_{-0.40}$E-5
Region 3 Components		
wabs	$N_{\rm H} = 0.16 \times 10^{22}$ cm^{-2}	
vmekal	$k\Gamma = 0.85$ keV	$K_{R3} = 3.50^{+0.95}_{-1.80}$E-4
	$\mathbf{Z}_{\alpha} = 0.51\ \mathrm{Z}_{\odot}$	
	$\mathbf{Z}_{Fe} = 0.11\ \mathrm{Z}_{\odot}$	
pl	$\Gamma = 1.07$	$K_{R3} = 1.54^{+0.71}_{-0.41}$E-5
Spread-out/scattered nuclear emission		
wabs		$N_{\rm H} = 1.48^{+6.76}_{-1.48} \times 10^{22}$ cm^{-2}
pl	$\Gamma = 1.9$	$K = 0.93^{+5.66}_{-0.93}$E-5
zgauss	σ=0.01 keV	E= $6.39^{+0.10}_{-0.07}$ keV
		$K_{line} = 5.42^{+3.08}_{-1.84}$E-6

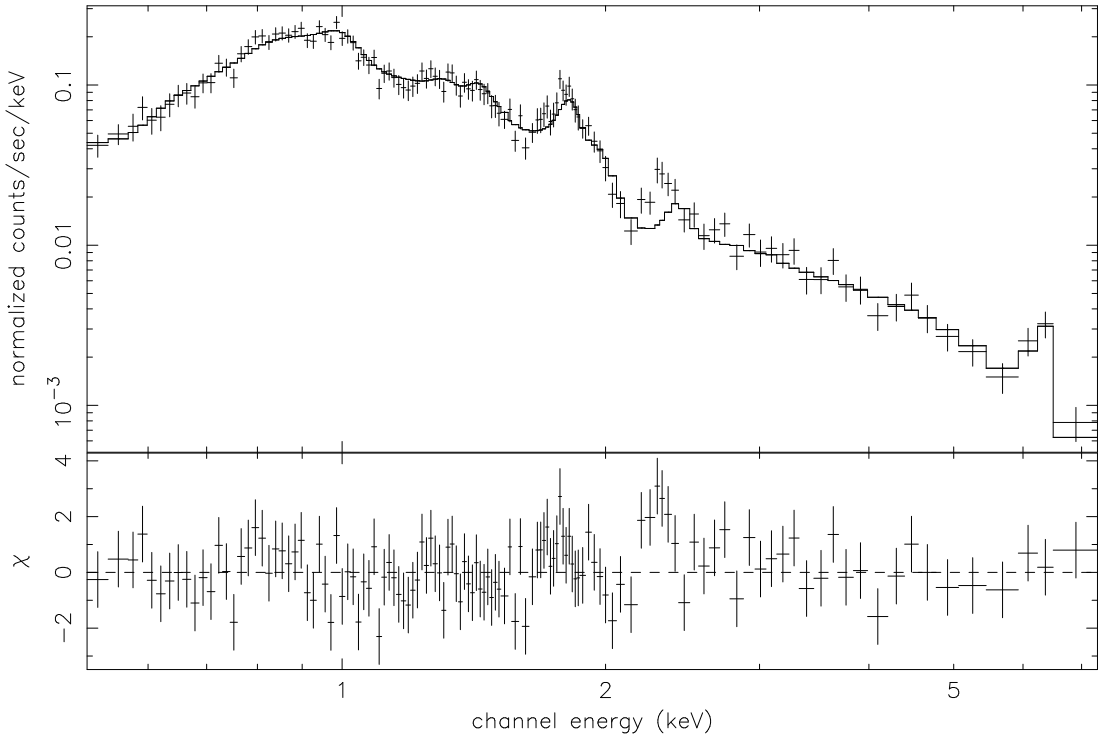

Figure 2.14: The spectrum of the complete Extended Region.

Table 2.12: Spectral model fits to the northern nucleus of NGC 6240, with χ^2_{red} (d.o.f.) = 0.37(94). The components for the composite model are described in the text.

Components	Fixed Parameters	Fitted Parameters
(1)	(2)	(3)
wabs		$N_{\rm H} = 1.12^{+1.82}_{-1.12} \times 10^{22}$ cm^{-2}
Thermal Component		
vmekal		kT $= 1.13^{+2.29}_{-1.02}$ keV
	$\mathbf{Z}_{\alpha} = 1$ Z$_{\odot}$	$\mathbf{Z}_{Fe} = 0.28^{+0.27}_{-0.21}Z_{\odot}$
		$K_{VMEKAL} = 8.36^{+12.24}_{-7.50}$E-5
Cold reflection component		
wabs		$N_{\rm H} = 1.13^{+5.22}_{-1.13} \times 10^{22}$ cm^{-2}
prxrav	$\Gamma = 1.9$	$R = 36^{+564}_{-29}$
		$K_{PEXRAV} = 3.12^{+2.64}_{-2.01}$E-5
zgauss	E= 6.40 keV	$K_{line} = 5.79^{+2.12}_{-2.09}$E-6
	σ=0.01 keV	

Table 2.13: Spectral model fits to the southern nucleus of NGC 6240. The components for the composite model are described in the text.

Model A:		χ^2_{red} (d.o.f.) = 1.01 (65)
Components	Fixed Parameters	Fitted Paramenters
(1)	(2)	(3)
wabs		$N_{\rm H} = 0.93^{+0.37}_{-0.73} \times 10^{22}$ cm^{-2}
Thermal Component		
vmekal		$k\Gamma = 1.09^{+0.61}_{-0.18}$ keV
	$\mathbf{Z}_{\alpha} = 1$ Z$_{\odot}$	$\mathbf{Z}_{Fe} = 0.44^{+0.17}_{-0.15}$ Z$_{\odot}$
		$K_{VMEKAL} = 1.39^{+0.50}_{-0.59}$E-4
Cold reflection component		
wabs		$N_{\rm H} = 1.45^{+2.71}_{-1.45} \times 10^{22}$ cm^{-2}
prxrav	$\Gamma = 1.9$	$R = 469^{+406}_{-409}$
		$K_{pexrav} = 6.73^{+5.27}_{-6.71}$E-6
zgauss	E= 6.40 keV	$K_{line} = 9.46^{+2.54}_{-2.55}$E-6
	σ=0.01 keV	

Model B:		χ^2_{red} (d.o.f.) = 0.84 (62)
Components	Fixed Parameters	Fitted Parameters
(1)	(2)	(3)
wabs		$N_{\rm H} = 0.81^{+0.46}_{-0.49} \times 10^{22}$ cm^{-2}
Thermal Component		
vmekal		$k\Gamma = 1.06^{+0.23}_{-0.17}$ keV
	$\mathbf{Z}_{\alpha} = 1$ Z$_{\odot}$	$\mathbf{Z}_{Fe} = 0.40^{+0.15}_{-0.15}Z_{\odot}$
		$K_{VMEKAL} = 1.09^{+0.61}_{-0.58}$E-4
Cold reflection component		
wabs		$N_{\rm H} = 1.29^{+4.89}_{-1.29} \times 10^{22}$ cm^{-2}
prxrav	$\Gamma = 1.9$	$R = 189^{+1823}_{-146}$
		$K_{prxrav} = 1.39^{+1.61}_{-1.39}$E-5
zgauss	E= 6.40 keV	$K_{line1} = 9.59^{+2.51}_{-2.50}$E-6
	σ=0.01 keV	
Warm scattered component		
pl	$\Gamma = 1.9$	$K_{pl} = 6.69^{+19.21}_{-6.69}$E-6
zgauss	E= 6.70 keV	$K_{line2} = 3.71^{+2.16}_{-2.20}$E-6
	σ=0.01 keV	
zgauss	E= 6.96 keV	$K_{line3} = 2.58^{+2.04}_{-2.00}$E-6
	σ=0.01 keV	

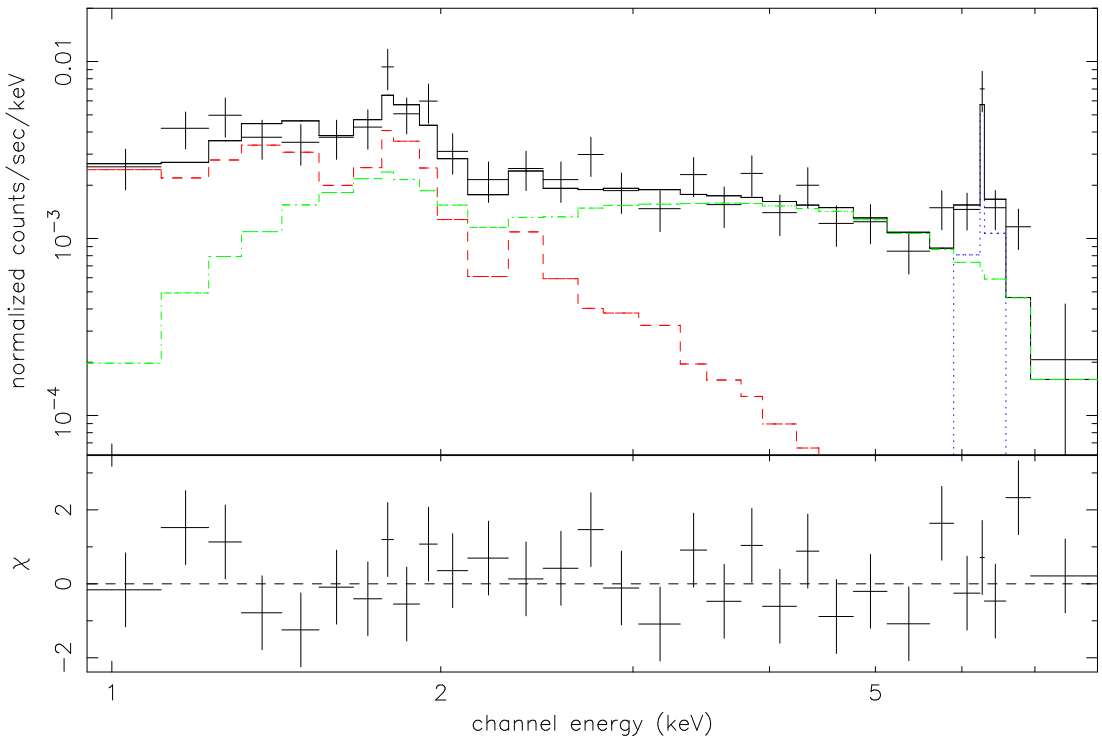

Figure 2.15: The spectrum of the northern nucleus of NGC 6240. The red line shows the projected thermal component (VMEKAL). The green line represents the cold reflection component (PEXRAV). The blue line denotes the Gaussian line (Fe Kα line at 6.4 keV).

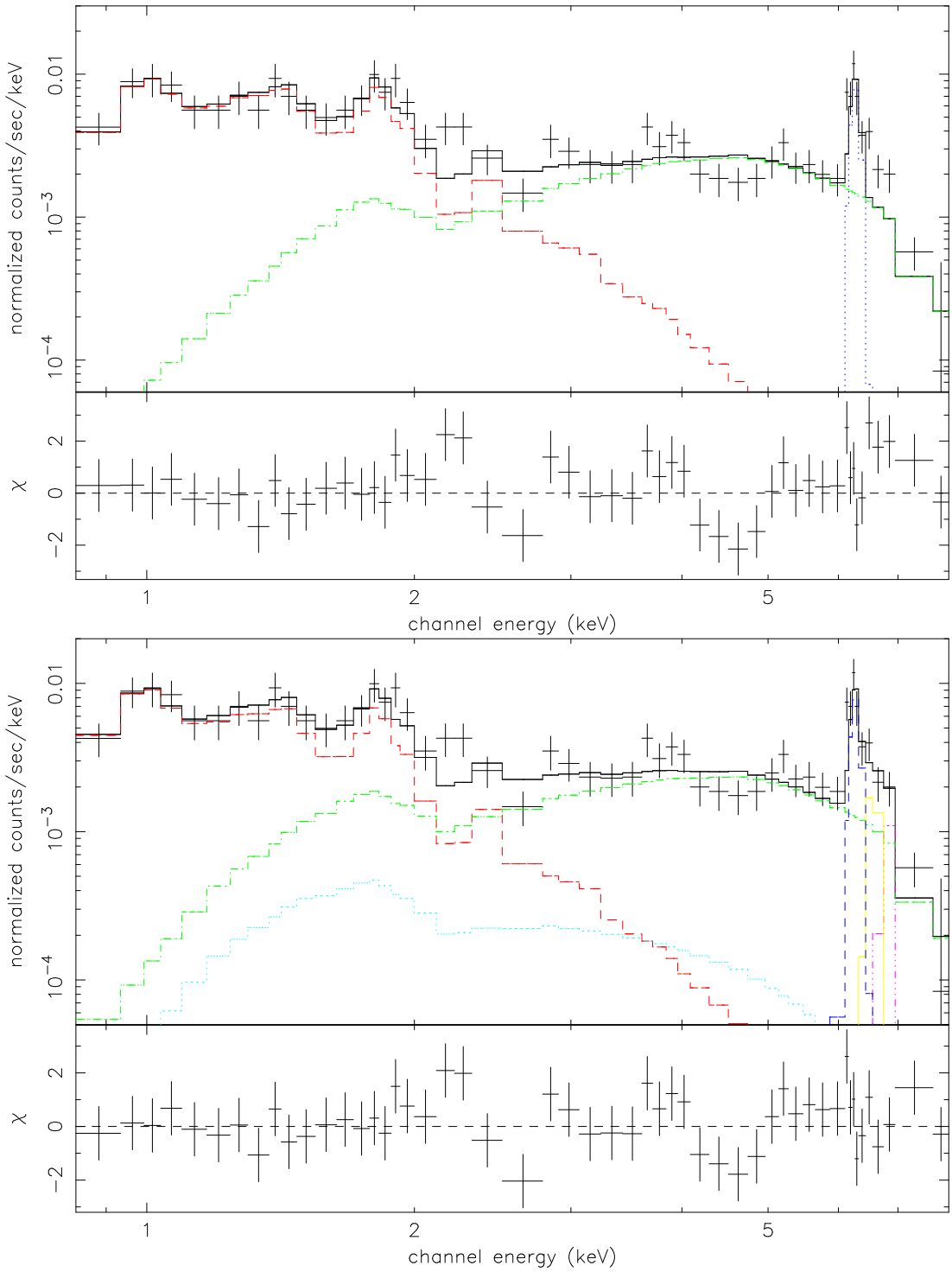

Figure 2.16: The spectra of the southern nucleus of NGC 6240. *Upper*: Model A; and *Lower*: Model B. The light blue line represents the warm scattered component. The yellow and magenta lines denote the Gaussian lines (at 6.7 keV and 6.97 keV, respectively). Other lines are the same as in Figure 2.15.

Komossa et al. (2003) reported the discovery of two Compton-thick X-ray sources in NGC 6240. Both of them are characterized by a relatively flat continuum above 3 keV and strong neutral Fe Kα line.

Following the results mentioned above, I tried to fit the spectra of the northern and southern nuclei with a composite model including both thermal plasma and cold reflection components from neutral material. The XSPEC reflection model, "pexrav" (Magdziarz & Zdziarski 1995) was used to represent the reflected emission for spectral data. Several input parameters of this model are set to the default values: (1) cosine of inclination angle: $\cos(i) = 0.45$, (2) cutoff energy of the illuminating power-law spectrum: $E_c = 100$ keV, (3) $Z = Z_\odot$ and $Z_{Fe} = Z_{\odot,Fe}$. Since the photon index Γ s poorly constrained, in order to better constrain the fits, I assumed that the photon index is typical of AGNs, $\Gamma = 1.9$, in the spectral fitting. The reflection scaling factor R is allowed to vary, which indicates the relative amount of reflection compared to the directly-viewed primary power-law component.

To check the contributions of the projected halo component to the two nuclear regions, the values of Norm/Area of this component are assumed to be 8, 10, 15, and 20 times of the Norm/Area of Ring 1 (namely, the same method as used in Section 2.3.3). Even if the maximum Norm/Area is assumed, the halo thermal component is too weak to affect the integrated spectra much. It is likely due to the small areas of two nuclei circles. Therefore, the projected halo thermal plasma is not involved in the composite models for the two nuclei.

Only one VMEKAL model is used to represent the projected starburst emission and the temperature of this model is expected to be similar to those of VMEKAL models of Region 1, 2 and 3. The α-element abundances are set to the solar value while the Z_{Fe} is allowed to vary. In summary, the composite model can be written as:

$$wabs_R * [\underbrace{vmekal_R}_{thermal\ component} + \underbrace{wabs_n(pexrav + zgauss_{6.40keV})}_{cold\ reflection\ components}],$$

where $wabs_R$ is the column density correlated with the starburst emission, $wabs_n$ is the absorption of the cold reflection component, $vmekal_R$ is the thermal component, $pexrav$ is the cold reflection component, and $zgauss$ is the Gaussian line for the neutral Fe Kα emission.

This fit gave the values of χ^2_{red} (d.o.f.) $= 0.37$ (94) (see Table 2.12) and 1.01(65) (see Model A in Table 2.13) for the northern and southern nuclei, respectively. The best-fit values of the reflection scaling factor $R = 36^{+564}_{-29}$ (northern) and 469^{+406}_{-409} (southern), indicate that the two nuclei have a reflection-dominated spectrum. The fitting results of the projected thermal component, such as the temperature of the VMEKAL model and the ratio of Z_α to Z_{Fe}, are consistent with previous studies of extended starburst emission (Region 1, 2, and 3). For the northern nucleus, the results are listed in Table 2.12 and the spectra is shown in Figure 2.15. On the other hand, for the southern nucleus, this composite model is labelled as Model A in Table 2.13, while the spectrum is shown in the upper panel of Figure 2.16.

Though the thermal plasma plus cold reflection model remains feasible based on

the spectral fitting alone, weaker residuals around 6.95 keV are still visible for the southern nucleus (see the upper spectrum in Figure 2.16). Since the energy locations of the Fe XXV (6.7 keV) and Fe XXVI (6.97 keV) lines is around 6.95 keV and they are most likely to account for the weak residuals, I speculate that more components are required by the spectral data of the southern nucleus. Both of iron lines at energies higher than 6.4 keV can be expected from a "warm mirror" (scattering from highly ionized medium, see Komossa et al. 2003). This is very similar to the case of NGC 1068, which has warm scattered component and the iron K line complex. Therefore, in addition to thermal plasma and the cold reflection component, I add a power-law model[12] and two Gaussian lines to represent the warm scattered component and the He- and H-like iron lines. Spectra data of the southern nucleus is fitted by another composite model (labelled Model B in Table 2.13), which can be written as:

$$wabs_R * [\ \underbrace{vmekal_R}_{Thermal\ component} + wabs_n * (\underbrace{pexrav + zgauss_{6.40keV}}_{Cold\ reflection\ components} + \underbrace{pl + zgauss_{6.70keV} + zgauss_{6.96keV})}_{Warm\ scattered\ component}\ ],$$

For this fit (Model B), the photon indices for both the spectrum incident on the reflecting medium and the power-law component were fixed at $\Gamma = 1.9$. Given the quality of the spectral data, it is necessary to constrain other model parameters. The reflection scaling factor $R = 189^{+1823}_{-146}$ remains large. The normalizations of the pexrav and power-law models are poorly constrained in this fits and they are very sensitive to each other. Although speculative and uncertain, the spectral data of the southern nucleus is in favor of Model B, since it can provide a plausible explanation for the existence of both neutral line and ionized iron lines for the southern nucleus. This scenario can supply a coherent explanation for the emission from the "jet-like" structure, which will be discussed and developed further in Section 2.3.6.

Despite the uncertainties in measuring $N_{\rm H}$, the X-ray measured obscuration towards the two nuclei $N_{\rm H}{}^{N} = 1.1 \times 10^{22}$ cm^{-2} and $N_{\rm H}{}^{S} = 1.3 \times 10^{22}$ cm^{-2} (Model B) are greater than those estimated from IR observations, $A_V^N = 1.6$ mag and $A_V^S = 5.8$ mag (Tecza et al. 2000), corresponding to $N_{\rm H}{}^{N} = 3 \times 10^{21}$ cm^{-2} and $N_{\rm H}{}^{S} = 10^{22}$ cm^{-2}, respectively. The IR extinction may be estimated with assuming a foreground screen, whereas X-rays sources would be more deeply embedded. Thus those derived in IR are the lower limits of absorption along our line of sight toward to the two nuclei. It is plausible that the $N_{\rm H}$ values measured in X-rays are larger. This is first pointed out by Maccacaro et al. (1982). The MERLIN neutral hydrogen absorption study (Beswick et al. 2001) indicates that $N_{\rm H}{}^{N}$ and $N_{\rm H}{}^{S}$ are on the order of 10^{22} cm^{-2}, which agree respectably with those measured from X-rays.

In summary, based on the spectral analysis in this section, I confirm the conclusion

[12]This may be a simplification of the actual situation, since an intermediately ionized "warm scatter" can also contribute line emission (see e.g. Fig. 5 of Komossa et al. 1998), but the quality of the spectral data does not warrant such a complex spectral fitting.

that both of the nuclei are heavily obscured and the reflection components dominate the *Chandra* bandpass. The spectrum of the northern nucleus can be fitted by a thermal plasma model plus a cold reflection component, whose observed 0.5-10 keV, absorption-corrected X-ray luminosity is $0.93\times\ 10^{42}$ ergs s^{-1}. The southern one seems to have ionized iron lines at energies higher than 6.4 keV, indicative of an additional warm scattered component. A composite model consisting of a thermal plasma model plus both cold reflection and warm scattered components is favored by the spectral data. The observed 0.5-10 keV, absorption-corrected X-ray luminosity of the southern nucleus is $1.61\times\ 10^{42}$ ergs s^{-1} (see Table 2.15).

2.3.6 The jet-like structure

X-ray detection of a "jet-like" structure is revealed by *Chandra* observations (Komossa et al. 2003). This spatially resolved structure adjacent to the southern nucleus is the strongest feature in the 1.0-1.5 keV band, which is identified in a $2.''5 \times 1.''7$ rectangular region with the shorter side in P.A. = 51° (see the description in Section 2.2.2 and Figure 2.4). When the spectral data is fitted only with the projected thermal plasma whose temperature kT is about 1 keV, an obvious "tail" is in the hard X-rays. Firstly, I examine the possibility that such a hard X-ray "tail" is due to starburst thermal plasma. If adding an additional thermal plasma model, the temperature of this component is higher than 6 keV and badly constrained. This indicates that thermal emission is not a tenable explanation for this structure. Secondly, given the location of this structure and the plausibleness of a scattering scenario for the southern nucleus, I considered that X-ray emission from this structure is due to a highly ionized scattering medium. Following this reasoning, I fitted the spectrum with a composite model consisting of one scattered power-law component and the projected thermal component:

$$wabs_R * [\ \underbrace{vmekal_R}_{Thermal\ component} + \underbrace{pl}_{Warm\ scattered\ component}\ ].$$

The best-fit parameters are listed in Table 2.14, and the spectrum is shown in Figure 2.17. From the spectral analysis, the luminosity of the scattered component in the "jet-like" structure $L^{sc}_{(0.5-10keV)}$ is $3.0\times\ 10^{41}$ ergs s^{-1} (see Table 2.15).

Table 2.14: Spectral model fits to the "jet-like" structure of NGC 6240, with χ^2_{red} (d.o.f.) = 0.18(188).

Components	Fixed Parameters	Fitted Parameters
(1)	(2)	(3)
wabs		$N_{\rm H} = 0.76^{+1.32}_{-0.44} \times 10^{22}$ cm^{-2}
Thermal Component		
vmekal		$kT = 0.96^{+0.19}_{-0.42}$ keV
	$\mathbf{Z}_{\alpha} = 1$ Z$_{\odot}$	$\mathbf{Z}_{Fe} = 0.40^{+0.25}_{-0.18}Z_{\odot}$
		$K_{VMEKAL} = 0.63^{+1.36}_{-0.28}$E-4
Warm scattered component		
pl	$\Gamma = 1.9$	$K_{pl} = 2.55^{+0.81}_{-0.54}$E-5

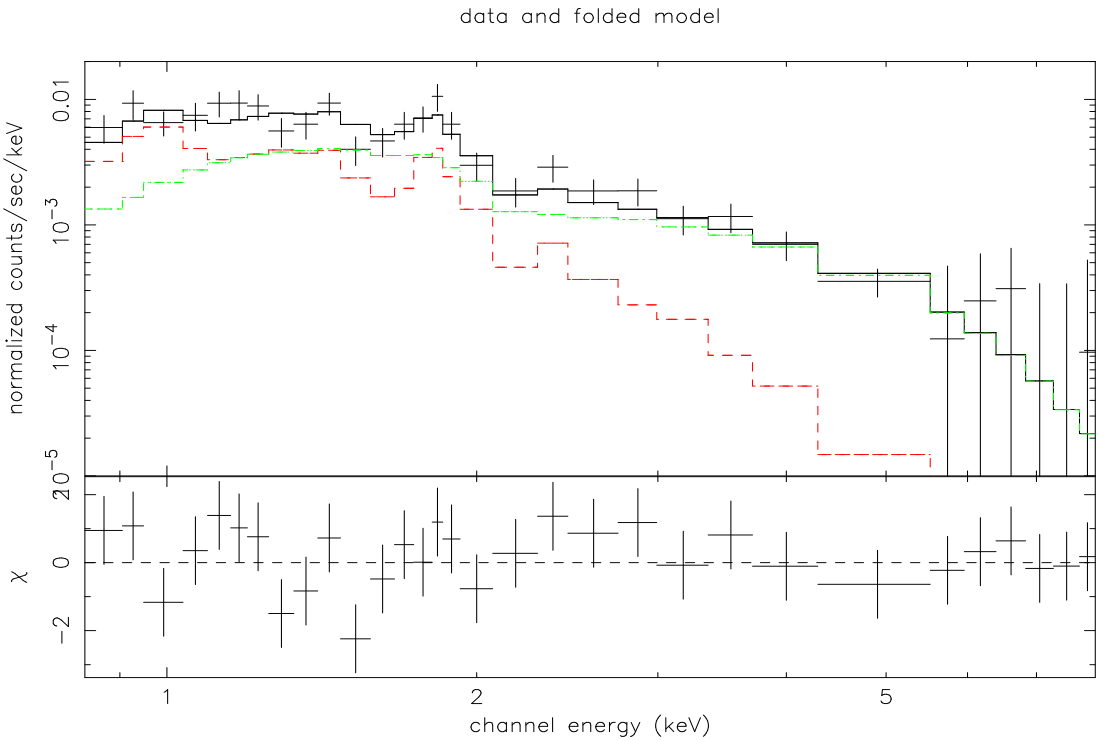

Figure 2.17: The spectra of the "jet-like" structure of NGC 6240. The red line shows the projected thermal component (VMEKAL). The green line represents the warm scattered component (power-law) component.

Table 2.15: Observed X-ray fluxes and luminosities of the two nuclei and the "jet-like" structure in NGC 6240.

Region	Model	Band keV	Flux (10^{-13} ergs cm^{-2} s^{-1})			Luminosity (10^{41} ergs s^{-1})		
			Total	Starburst	AGN	Total	Starburst	AGN
Northern	vmekal+	0.5-2	1.49	0.75	0.74	3.49	1.76	1.73
nucleus	pexrav+	2-10	3.39	0.15	3.24	7.93	0.35	7.58
	line	0.5-10	4.89	0.91	3.98	11.44	2.13	9.31
Southern	vmekal+	0.5-2	1.72	1.16	0.56	4.02	2.71	1.31
nucleus	pexrav+	2-10	6.51	0.19	6.32	15.32	0.44	14.79
	pl+lines	0.5-10	8.22	1.34	6.88	19.23	3.14	16.10
Jet-like	vmekal+	0.5-2	1.22	0.69	0.53	2.85	1.61	1.24
structure	pl	2-10	0.84	0.09	0.75	1.97	0.21	1.76
		0.5-10	2.06	0.78	1.28	4.82	1.82	3.00

2.4 Discussion

2.4.1 Large scale halo emission

A low surface brightness halo component is identified in the soft X-ray images of NGC 6240 from the *Chandra* ACIS-S observations, extending far beyond bright "butterfly-shaped" extended emission (inner 14 kpc), out to about 40 kpc from the two nuclei. *Chandra* detections of the large scale halo emission confirm previous results first hinted by *ROSAT* instruments (Komossa et al. 1998). Such a weak, large scale halo component has also been found in optical emission-line images: Hα and [N II] λ6583 emission is detected over a similar area as *Chandra* X-ray emission, and complex optical filaments are visible at least 30-40 kpc from the center (see Figure 16 of Veilleux et al. 2003).

From the spectral analysis, this halo emission is discovered to be spatially constant throughout the large scale annulus region with inner and outer radii of 14 and 42 kpc, respectively. The spectrum can be fitted with a thermal plasma with kT $\sim$ 0.6 keV and subsolar ($\mathbf{Z} \sim 0.1\ \mathbf{Z}_{\odot}$) metal abundances. It is possible that, as a ULIRG, NGC 6240 has hot halo emission. In a *Chandra* ULIRGs survey, some other ULIRGs are also found to have hot halos (outside $\sim$ 10 kpc) with a temperature of about 0.6 keV and a low metallicity (Huo et al. 2004). Based on the *Chandra* X-ray investigation from dwarf starbursts to ULIRGs, Grimes et al. (2005) further point out that even at large physical distances the halos of ULIRGs have higher temperature than those of the starburst galaxies and the ULIRGs as a class tend to preferentially occupy the high end of the temperature range (kT $\sim$ 0.25-0.75 keV).

2.4.2 Bright X-ray emission from the Extended Region

Soft diffuse emission from bright extended region (inner 14 kpc) surrounded by weak halo emission, has a spectacular "butterfly-shaped" structure, including three $\sim$ 10 kpc size loop-like regions (Region 1, 2 and 3). When comparing with *HST* images (Gerssen et al. 2004), Komossa et al. (2003, 2004) found this X-ray structure is coincident with Hα emission. The coincidences bring support to the starburst-driven superwinds scenario (Heckman et al. 1987, 1990): the soft X-ray emission from the bright extended loop-like regions are powered by a galactic superwind driven by the collective mechanical energy input from supernovae; both soft X-ray emission and optical line emission trace the interaction of the wind with denser ambient medium of the galaxy (e.g. Schulz et al. 1998; Komossa et al. 1998; Komossa et al. 2003, 2004). Schulz et al. (1998) estimated the superwind models. They adopted a supernova rate of 1 SN yr^{-1} (1 SN yr^{-1}: Colbert et al. 1994; 2 yr^{-1}: van der Werf et al. 1993) 1994) and assumed a mechanical input power of $L_{mech} \sim 3 \times 10^{43}$ ergs s^{-1}, The energy input power can drive a single shell extends to $\sim$ 10 kpc, over a period of 3×10^7 yr, within a medium of 0.1 cm^{-3} density.

The spectra of Region 1, 2 and 3, can be well described by a composite model consisting of (i) the projected halo thermal component; (ii) a thermal plasma model VMEKAL with the temperatures higher than the halo component, standing for diffuse hot gas in three loop-like regions; and (iii) a power-law model representing the populations of X-ray binaries.

The hot thermal plasma component dominates at energies lower than 2 keV. The temperatures kT of the thermal plasma VMEKAL models for three regions vary between 0.8 and 1.2 keV and lie in the typical temperature range kT = 0.2-3.0 keV for local starbursts (Ptak et al. 1999). The α-element-to-iron abundance ratio $\mathbf{Z}_\alpha/\mathbf{Z}_{Fe}$ is 3-5 times higher than the solar ratio. Similar cases of the enhanced $\mathbf{Z}_\alpha/\mathbf{Z}_{Fe}$ have been reported in other starburst galaxies (e.g. Ptak et al. 1997; Tsuru et al. 1997; Martin et al. 2002; Fabbiano et al. 2004; Strickland et al. 2004; Grimes et al. 2005). On the one hand, the enhanced $\mathbf{Z}_\alpha/\mathbf{Z}_{Fe}$ is consistent with metal-enrichment by Type II Supernovae in a young stellar population (Martin et al. 2002). On the other hand, it is also possible that the high $\mathbf{Z}_\alpha/\mathbf{Z}_{Fe}$ is due to some residual depletion of the iron on dust grains in the hot gas (Strickland et al. 2004 and references therein).

Though off-nuclear point-like sources are not detected, this does not mean no emission from X-ray binaries. because the lack of emission from X-ray binaries is incompatible with the enhanced star formation activity and the high supernovae rate in NGC 6240 (2 yr^{-1}: van der Werf et al. 1993; 1 yr^{-1}: Colbert et al.1994). Therefore, I speculate that the X-ray binaries are embedded in the diffuse emission and undetected due to the bright backgrounds. As remarked earlier, the undetected X-ray binaries represented by a power-law model might produce the bulk of the 2-10 keV flux. There are two populations of X-ray binaries: high-mass X-ray binaries (HMXB) and low-mass X-ray binaries (LMXB). From the integrated spectra, the two populations of HMXBs and LMXBs are difficult to be distinguished from one another. X-rays from HMXBs result from accretion by a neutron star of matter from the radiatively driven wind of an OB star with timescales of t$_x$ $\sim$ 10^4 yr, while LMXBs produce X-ray emission from accretion onto a neutron star or black hole via Roche lobe overflow from from a

low-mass star with timescales of $t_x \sim 10^7$ yr (Persic & Raphaeli 2002). The effective spectral photon indices of the integrated HMXB and LMXB are very similar and compatible with each other. Tecza et al.(2000) determined the starburst in NGC 6240 has a typical age of 1.5-2.5 $\times$ 10^7 yr based on the analysis of near-infrared integral field spectroscopy of NGC 6240. If the lifetime of the a single starburst is assumed to be 10^8 yr, the X-ray contributions from HMXBs is expected to dominate the hard X-ray emission, since the LMXBs have not had time to evolve from the main sequence and to come into Roche lobe contact (Persic et al. 2004; Teng et al. 2005). Moreover, the spectral results in Section 2.3.3 show that the best-fit values of photon indices of the power-law model varying between 1.0 and 1.6 are roughly consistent with those of HMXBs ($\Gamma \sim$ 1.0-1.4). Therefore, the X-ray emission above 2 keV of the three loops (Region 1, 2 and 3) indicates that the undetected and embedded HMXBs have dominant contributions to the hard X-ray spectra.

Following Persic & Rephaeli (2002), I suppose the hard (2-10 keV) emission from the bright extended region is only due to luminous ($\geq 10^{37}$ ergs s^{-1}) X-ray binaries. According to Table 2.10, the total 2-10 keV luminosity of Region 1, 2 and 3 is $8.9^{+6.7}_{-5.8}\times10^{41}$ ergs s^{-1}. This indicates NGC 6240 needs $\sim9\times10^4$ X-ray binaries for 2-10 keV emission of the extended regions. This value is 100 and 170 times the number of X-ray binaries required by the starburst galaxies M82 and NGC 253, respectively (Persic & Rephaeli 2002). If ultraluminous X-ray sources (ULXs) have contributions to the hard X-ray emission, the required number of X-ray binaries becomes smaller.

Both FIR luminosity and 2-10 keV luminosity mainly due to HMXBs, are good indicators of the current global star formation rate (SFR) (e.g. Franceschini et al.2003). The correlation between FIR luminosity and SFR is yielded by Kennicutt (1998): SFR = $L_{FIR}/2.2 \times 10^{43}$ $M_\odot$ yr^{-1}. The SFRs estimated from the FIR luminosity (6.6×10^{11} $L_\odot$) is 115 $M_\odot$ yr^{-1}. The correlation between the luminosity of HMXBs and the star formation rate (SFR) has been lately discussed in several references, e.g. Nandra et al. (2002), Grimm et al. (2003), Ranalli et al. (2003) and Persic et al. (2004). The total 2-10 keV luminosity of Region 1, 2, and 3 is 8.9 $\times$ 10^{41} ergs s^{-1}, according to Table 2.10. X-ray-derived SFRs is listed in Table 2.16. Three of them are compatible with the SFR from infrared measurement. Only the SFR using the correlation by Persic et al. (2004) is larger than that estimated from the infrared. Indeed, the calibration of Persic et al.'s relation is lower than that of Ranalli et al's relation by a factor of f = 0.2 (see Eq. (2) of Persic et al. 2004). So, the SFR derived from Persic et al.'s relation is 5 times the SFR derived from Ranalli et al's relation, as listed in Table 2.16.

2.4.3 Estimate of an upper limit for the luminosity of off-nuclear X-ray sources

Due to the lack of detection of point sources in the extent of NGC 6240, it is interesting to estimate the upper limit of the luminosity of these sources. In this section, the upper limit of luminosity of the supposed point-like sources in Region 1 will be simply estimated. Since Region 1 is located in the bright extent, the results can be viewed as a typical upper limit for the luminosity of the embedded point sources.

In order to estimate the upper limit for the luminosity, the lower limit for any

Table 2.16: Comparison of SFR of NGC 6240 derived from HMXBs luminosities.

SFR ($M_\odot$ yr^{-1})	References
160	Nandra et al. 2002
133	Grimm et al. 2003
178	Ranalli et al. 2003
890	Persic et al. 2004

detection is firstly considered in a qualitative analysis. From Table 2.1, the net counts per square arcsec is 10.2 for Region 1. Given the widening of the point spread function (PSF) at ~ 6 keV, the radius of one circular region is set at 0.6 arcsec, which ensures the encircled energy of 70%, which means the number of total counts N is 11 in this circular region. The lower limit of detection is often taken as 3 times the standard deviation of the background counts, based on that a signal at a level 3 times the standard deviation above the mean background has a 99.87% probability of not belonging to the background distribution. If the standard deviation is the square root of counts, 3 times the standard deviation is 8.8 counts per square arcsec in the circle region. This indicates one point-like source would be detected, if there are $\sim$9 excess counts existing.

I run a MARX (Model of AXAF Response to X-rays [13]) simulation for a point source with a power-law spectrum observed with ACIS to produce the simulated events file. MARX is a set of programs designed to enable the user to simulate the on-orbit performance of the Chandra satellite. The simulated events file fulfilled the requirements of the lower limit of detection. I also processed the file with CIAO and XSPEC in order to obtain the luminosity of the point-like source. In this estimation, a point source is modelled by a power-law with $\Gamma = 1.9$ and column density is set to the typical value $\sim 2 \times 10^{22}$ cm^{-2} for the extended emission in NGC 6240. Then, the flux of this simulated point source (0.5-10 keV) is 8.5×10^{-15} ergs cm^{-2} s^{-1}. Given the distance of NGC 6240, the luminosity is 2×10^{40} ergs s^{-1}, which can be taken as the upper limit of the luminosity of any embedded point-like sources.

Thanks to the superior sensitivity and spatial resolution of the *Chandra* observatory, a number of point-like sources have been discovered. For example, in NGC 4038/4039 (the Antennae), a large population of extremely luminous ($L_X \sim 10^{38}$-10^{40} ergs s^{-1}) point-like sources are detected (Fabbiano et al. 2001). The upper limit of the luminosity ($\sim 10^{40}$ ergs s^{-1}) estimated in this section is approximately the maximum luminosity of the point-like sources detected in NGC 4038/4039. The lack of the detection of point-like sources is therefore not due to the absence of X-ray bright point sources. It is possible that an amount of X-ray point-like sources with the luminosities less than 10^{40} ergs s^{-1} are existing but undetected and unresolved because of the high surface brightness of the diffuse components. Such unresolved point sources (most likely to be HMXBs) should be responsible for the hard X-ray component required by spectral

[13] http://space.mit.edu/CXC/MARX

data of the extended regions in NGC 6240.

The correlation between the luminosity of the bright point sources in a galaxy and the SFR has been noted by Gilfanov (2004). The luminosity of the brightest point source increases with the SFR, until it reaches the maximum possible value. In Figure 6 of Gilfanov (2004), once the luminosity reaches the maximum possible value of $L_X \sim 10^{40}$ ergs s^{-1}, the SFR is not sensitive to it any more and the SFR could be any value in the range between 10 M$_\odot$ yr^{-1} and a few hundred M$_\odot$ yr^{-1}. Therefore, the SFR is poorly constrained by the luminosity of the brightest X-ray point sources if L_X is 10^{40} ergs s^{-1}.

2.4.4 The nuclear emission

For the first time, *Chandra* ACIS-S observations revealed the marvellous phenomenon: both nuclei of NGC 6240 are of the AGN character (Komossa et al. 2003). The detection of the strong Fe Kα feature at 6.4 keV in both nuclei is convincing evidence of originating from fluorescence in cold material. It is also mentioned by Komossa et al. (2003) that the He-like (6.70 keV) and H-like (6.70 keV) lines appear to be present in both nuclei, but they are much weaker in the northern nucleus than in the southern one.

In Section 2.3.5, I confirm the conclusion that both of them are heavily obscured and the reflection components dominate the *Chandra* bandpass. The presence of He-like and H-like lines at 6.70 and 6.96 keV is indicative of an additional complexity, and it is possibly due to the warm scattered component. The observed luminosities in 0.5-10 keV of the northern and southern nuclei are 0.93×10^{42} erg s^{-1} and 1.61×10^{42} erg s^{-1}, respectively. The intrinsic luminosities are significantly larger, and probably provide a major fraction of the bolometric luminosity of NGC 6240, as suggested by Schulz et al. (1998).

The interpretation involving in the warm scattering medium is in agreement with the X-ray detection of the spatially extended "jet-like" structure, which is the strongest feature in soft X-ray band of 1.0-1.5 keV and adjacent to the southern nucleus. The emission from the "jet-like" structure most likely originates from the scattering of the nuclear continuum on photoionized gas. Such a scenario has been found in Compton-thick Seyfert 2 galaxies (e.g. NGC 1068: Young et al. 2001; Kinkhabwala et al. 2002; Ogle et al. 2003). If this is the case, the comparison between *HST* [O III] and soft X-ray images is expected to supply further evidence for a photonized medium surrounding the southern nucleus. The scattered luminosity L^{sc} can be determined by:

$L^{sc} = \mathbf{f} N_e \mathbf{r} \sigma L_x$

where $\mathbf{f}$ is the covering factor, N_e is the electron density fixed to 10 cm^{-3}, $\mathbf{r}$ is about 1 kpc, σ is the Thomson cross-section 6.65×10^{-25} cm^2 and L_x is the intrinsic luminosity of the southern nucleus $\sim 10^{44}$ erg s^{-1}. This scatterer is subtended in the southwest cone and much brighter than its counterpart in the northeast. Due to the asymmetry of the scattering cone, the covering factor $\mathbf{f}$ applies to the southwest cone alone. $\mathbf{f}$ is 0.0625 if assuming the cone has an opening angle of 45°. Adopting these parameters leads to the scattering luminosity $L^{sc} = 1.25\times10^{41}$ erg s^{-1}, which is very close to the observed value (3.00×10^{41} erg s^{-1}).

The hard X-ray emission (5.0-8.0 keV) is highly centralized around the two nuclei,

but marginally extended which is likely to be the spread-out/scattered nuclear emission. Most of the CO-emitting gas in NGC 6240 is concentrated in the central 3″ radius (2.1 kpc) region (Tacconi et al. 1999). The dense molecular clouds not only can play an important role for the high X-ray column density occulting the two nuclei, but also can be responsible for the reflected X-rays and for the strong iron K fluorescence line at 6.4 keV (Iwasawa & Comastri 1998). Checking a high-quality Fe Kα band (6.2-6.5 keV) image would be very helpful in order to investigate it, since the 6.4 keV Fe Kα line is a good indicator of cold gas. It requires deeper *Chandra* ACIS-S observations of NGC 6240 in the future since a longer exposure can reveals more details.

2.5 Summary

I have described the detailed analysis of the spatial and spectral properties of the X-ray emission from NGC 6240 with a 37 ks *Chandra* ACIS-S observation. With the unprecedented high resolution of *Chandra* X-ray telescope I am able to spatially isolate the different contributing components and determine the complex nature of the X-ray emission. The results are summarized below:

1. For NGC 6240, a weak, large-scale halo component extending outwards to 40 kpc is identified in the soft X-ray image and has a common spatial scale in optical emission-line images. This halo emission is spatially constant. The soft X-ray spectrum taken from the radial range of 20-60 arcsec (14-42 kpc) to the center of the galaxy can be fitted by a standard model: a one-temperature MEKAL model with kT $\sim$ 0.6 keV. The X-ray derived metal abundance is subsolar, at 0.1Z$_\odot$.

2. Surrounded by the weak halo component, the bright extent has a spectacular "butterfly-shaped" structure, including three loop-like regions. The extent is so bright that no off-nuclear point-like sources are detected in the extent. I favor a composite spectral model, consisting of (i) the projected halo component, (ii) a thermal plasma ("VMEKAL") model with a typical temperature around 1 keV, and (iii) a power-law model representing the population of X-ray binaries, for the ACIS-S spectra of the three regions. Thermal VMEKAL models require ratios of α-to-iron 3-5 times higher than the solar ratio, similar to starburst galaxies. The power-law components of three regions dominate contributions to hard X-ray (2-10 keV) band and the photon indices vary between 1.0 and 1.6. Considering the starburst history of NGC 6240 and the different characters of HMXBs and LMXBs, I speculate that the power-law component should reflect the properties of the integrated HMXBs, which are likely to be embedded in diffuse X-ray emission. The total 2-10 keV luminosity of three loop-like regions is $\sim 10^{42}$ ergs s^{-1}. The

3. The upper limit for the luminosity of any off-nuclear point-like sources is $\sim 10^{40.3}$ ergs s^{-1}, estimated from a MARX simulation. This value is approximately the maximum luminosity of extremely luminous point sources detected in NGC 4038/4039.

4. I confirm the two nuclei are heavily obscured and the reflection components dominate the *Chandra* bandpass. The southern nucleus seems to show ionized iron line emission at energies higher than 6.4 keV. The 0.5-10 keV luminosities are 0.93$\times$ 10^{42} ergs s^{-1} and 1.61$\times$ 10^{42} ergs s^{-1} for the northern and southern nuclei, respectively. The spatial and spectral results indicate that the hard X-ray emission is marginally

extended. It is due to either the spread-out of the PSF or scattered nuclear emission. Deeper *Chandra* observations are helpful to resolve this puzzle. The southern nucleus shows both the neutral Fe Kα and the ionized iron emission, indicative of the existence of an additional warm scatterer. One "jet-like" structure, southwest of the southern nucleus, is likely to be scattered emission.

CHAPTER 3
NGC 2782

3.1 Introduction

X-ray observations can offer significant evidence for both AGN and starburst activities. Moreover, there is some evidence that a fraction of AGNs do not show the typical Seyfert characteristics in their optical spectra, but they show features of a hidden AGN from X-ray observations (e.g. NGC 6240). The 2-10 keV spectra of heavily obscured AGNs show a reflection component and a prominent Fe Kα line, whereas the intrinsic transmitted component is observed in the 10-100 keV range (Done, Madejski & Smith 1996; Guainazzi et al. 2000).

NGC 2782 is a nearby galaxy (D=51 Mpc, assuming H_o = 50 km s^{-1} Mpc^{-1}). The nature of its nuclear emission is still unclear. It was originally classified as a Seyfert galaxy (Seyfert 1943), while Boer, Schulz & Keel (1992) argued that the optical nuclear spectrum is typical of a nuclear starburst. New optical spectroscopy puts the source in the transition region of the Veilleux & Osterbrock (1987) diagnostic diagrams, based on its optical emission-line ratios (Boer et al. 1992, Ho et al. 1997, Usui et al. 2001; see Figure 3.1). Soft X-ray data from *ROSAT* shows X-ray emission characteristic of superwinds related to starburst activity, but can not exclude a hidden low-luminosity AGN (Schulz et al. 1998). Therefore we can not rule out the possibility of the coexistence of starburst and AGN activity in NGC 2782. If a dense obscuring column of gas is located along our line of sight, it can be strongly attenuate the direct X-ray emission from an AGN. If this is the case, hard X-rays (above 2 keV) offer an important tool to investigate the presence of a hidden AGN, since hard X-rays can penetrate through the obscuring material. The scattering medium located along the polar axis of a disk-like gaseous structure has a direct view of the nucleus. Observing directly a large equivalent width fluorescent Fe Kα line provides the clearest evidence for the presence of a hidden AGN.

Gaseous outflows are easily detectable through the following emission processes: optical line emission (e.g. Hα, [O III]), radio synchrotron continuum emission and diffuse soft X-ray emission. Strong evidence for a spatially resolved, starburst-driven outflow in NGC 2782 has been found in both optical and radio observations. The most important piece of evidence is an additional high-excitation component 5″ south of the central bright emission. This component was first identified by Boer et al. (1992), and compelling evidence for this spatially resolved shell-like structure comes from Hα, [O III] and 5 GHz radio continuum (hereafter RC)images. Due to the low resolution of *ROSAT*, we were unable to see the X-ray outflow morphology in NGC 2782 in previous *ROSAT* images. The detailed filamentary (and/or low surface brightness) emission which has been shown in the optical and radio wave bands is expected to be seen when data with high angular resolution are available.

In this chapter, we make use of *Chandra* high-resolution imaging spectroscopy of NGC 2782, which permits a detailed study of the physical properties of the starburst-driven superwind in the X-ray band, and can also provide important hints with regard to the nature of the central region, allowing us to determine whether the AGN or

the starburst dominates the core emission. More detailed information of the energy-dependent structure is expected to be distinguished clearly in the *Chandra* X-ray images.

This chapter is organized as follows: in Section 3.2, the observations and data reduction are described; the imaging and spectral analyses are reported in Section 3.3 and 3.4, respectively; the discussion is presented in Section 3.5, including the interpretation of the nature of the core emission and the more extended X-ray emission outside the core region; we conclude in Section 3.6.

3.2 Observations and data reduction

NGC 2782 was observed by the *Chandra* Imaging Spectrometer ACIS-S on May 15 2002 (ObsID 3014), for 29.96 ks on the S3 chip. The standard Level 2 event files obtained by the Standard Data Processing (SDP) were filtered on good time intervals, resulting in an effective exposure time of 29.80 ks. The *Chandra* data were downloaded from the *Chandra* data archive. These data were reduced and analyzed with the CIAO version 3.0.2 and XSPEC version 11.3.2 software packages. I examined the light curves extracted from an area of 2.2 arcmin^2 within the energy range of 0.3-10.0 keV and found no significant flares. It is unnecessary to further clean the data to remove periods of high background levels, and the full dataset within the standard good time intervals of 29.80 ks were used in the following analyses. For a more detailed description of many of the imaging and spectral analysis techniques used, I refer the reader to Chapter 2, unless otherwise stated.

3.3 Imaging analysis

Figure 3.2 shows the broadband (0.5-8.0 keV) *Chandra* ACIS-S3 raw image of NGC 2782, with a resolution of 0.49 arcsec per pixel. This detailed image, for the first time shows the X-ray morphology of NGC 2782. The X-ray emission can be divided into three main components: a bright core source, bipolar soft X-ray extended emission surrounding the core source, e.g. enhanced off-nuclear emission to the south at 5″-8″ and finally very weak diffuse emission. In the smoothed soft X-ray image (see Figure 3.3), the X-ray emission has a bipolar structure, extending northwardly and southwardly from the nucleus. The northern emission can be traced out to a distance of at least 30″ (3 σ above the background), and is more elongated than the southern emission, which can be traced to 15″. The largest difference between the north and the south emission is the striking shell-like structure with enhanced emission 5-8″ south of the bright core emission.

In *Chandra* images, the particular structures of NGC 2782 vary greatly depending on the energy range. Figure 3.4 shows the central 10″ X-ray emission of NGC 2782 in six X-ray bands. The energy ranges used are 0.5-1.0 keV, 1.0-1.5 keV, 1.5-2.0 keV, and 2.0-2.5 keV, 5.0-8.0 keV, and 6.0-6.5 keV. These images clearly show a change of morphology with X-ray energy. NGC 2782 shows extended X-ray emission up to 2

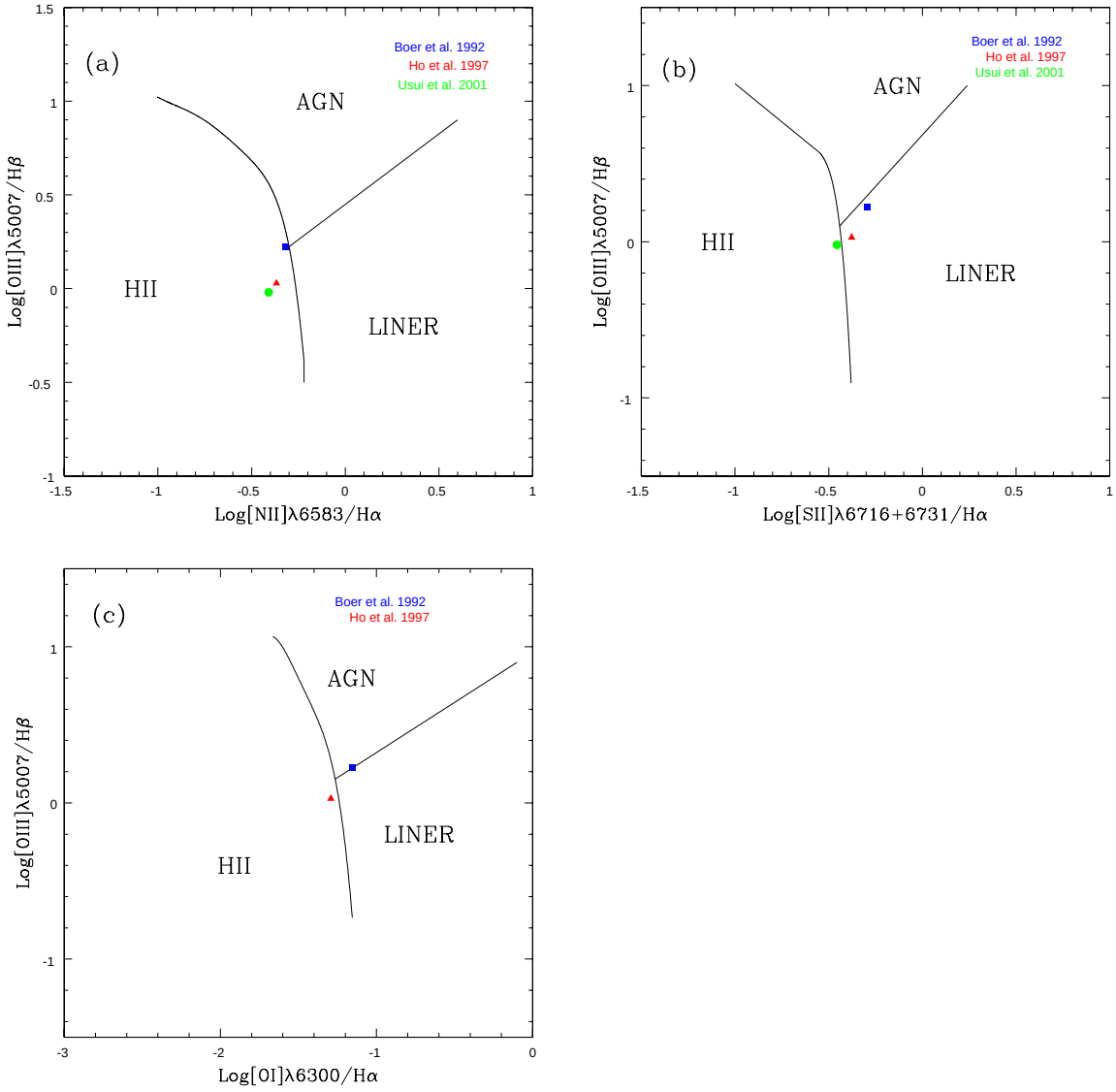

Figure 3.1: The position of NGC 2782 in the diagnostic diagrams of Veilleux & Osterbrock (1987), based on optical emission line ratios: (a) [O III]/Hβ *vs.* [N II]/Hα diagnostic diagram; (b) [O III]/Hβ *vs.* [S II]/Hα diagnostic diagram; (c) [O III]/Hβ *vs.* [O I]/Hα. Observed values of the optical emission line ratios in the references are shown by symbols indicated at top right corners. The solid lines are empirical boundaries used to delineate the three regions (AGN, LINER or H II) indicated on each plot.

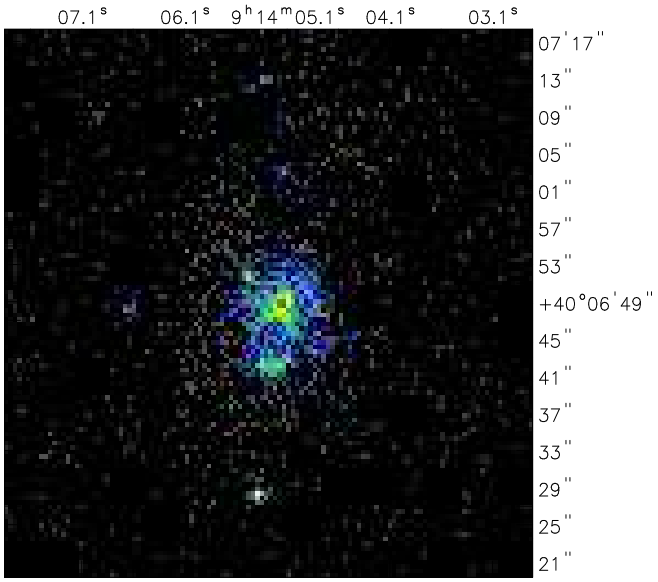

Figure 3.2: The broad-band (0.5-8.0 keV) *Chandra* ACIS-S3 raw image of NGC 2782. North is to the top, and east is to the left. The field of view is 58″.8 × 58″.8.

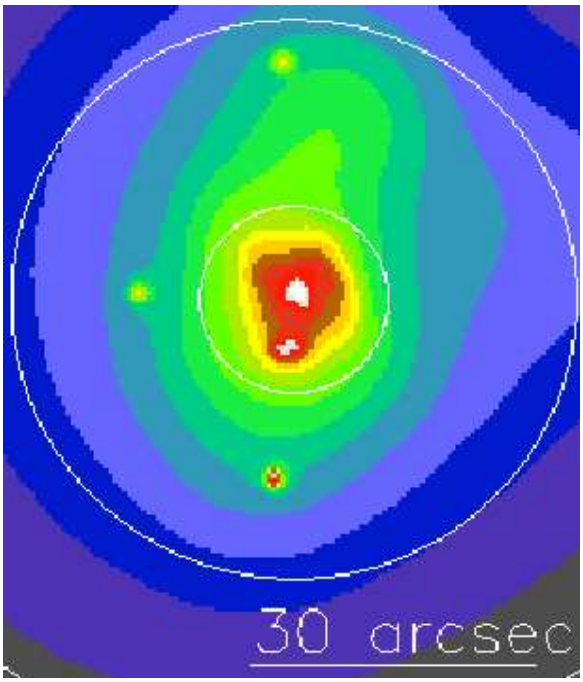

Figure 3.3: Adaptively Smoothed soft X-ray (0.5-1.5 keV) image of NGC 2782, in which the large scale north-south extended emission can be seen. The white bar represents 30″; North and east as in Figure 3.2.

keV, and above 2 keV the core emission dominates. The compact X-ray core source is surrounded by brighter extended soft X-ray emission. Within a radius of 10″, the most significant feature is the enhanced emission 5-8″ south of the core source, with a shell-like structure. With increasing X-ray energy, the enhanced emission becomes fainter, fading at X-ray energies higher than 2 keV. The core source is likely to be prominent in the hard X-ray (2-8 keV) band. After examining the intensity images up to 8 keV, we find that the position of the core source is systemically consistent in the energy range of 2-8 keV within the uncertainty of 0.5″. Running a standard source detection routine, the core is detected as a source in the energy interval 5-8 keV with signal-to-noise ratio of 5.4. The hard X-ray emission is dominated by this core point source. The radial profile of the core source in the 4.0-8.0 keV energy band is plotted in Figure 3.5. The red solid curve represents the best-fit Gaussian model convolved with the 6.4 keV PSF.The measured FWHM of 0.61±0.12 arcsecond, which is consistent with the expected width of the Chandra PSF, confirms the point-source nature of the core source. Therefore, NGC 2782 can be viewed as a point source above 4.0 keV.

Five off-nuclear point sources are detected in total in NGC 2782 within a radius of about 30″. Most of them are too faint to allow us to obtain spectral fits. The brightest one has about 60 counts. If a power-law spectral shape is assumed to estimate its luminosity, it has a luminosity of 10^{40} erg s^{-1}. Future deeper observations are needed to study these sources further.

In conclusion, the *Chandra* high resolution data allow us to deconvolve the X-ray emission of NGC 2782, for the first time, into three different components: firstly, the compact core source dominating in the hard X-ray regime; secondly, the bright extended emission surrounded the core source within a radius of about 10″, including the enhanced shell-like emission correlated with the Hα bubble; and thirdly, the weak, large-scale diffuse emission, which extends northward and southward.

3.4 Spectral analysis

In this section, we present a detailed spectral analysis of NGC 2782 using the *Chandra* ACIS data.

3.4.1 The extended emission

The spectrum of the large-scale extended diffuse emission is extracted from an annulus with radii of 10″ and 30″, centered on the core source, as shown in Figure 3.3, after excluding all the point-like sources. Given the weakness of the extended diffuse emission, the spectrum is fitted only in the 0.5-2.5 energy range keV. Extending the energy range does not affect the results. The spectrum can be fitted with a thermal MEKAL plasma with a temperature of 0.58 keV, and absorption fixed to the Galactic column density, $N_{\rm H,Gal}$=1.8 $\times 10^{20}$cm^{-2}. Figure 3.6 shows the spectrum and the corresponding best fitting model, and Table 3.1 details the results from the fitting of the model. The absorption-corrected soft-Xray luminosity is $L_x \approx 1.7 \times 10^{40}$ erg s^{-1}.

As mentioned in Section 3.3, inside the weak, bipolar extended emission, a bright diffuse emission component exists, surrounding the compact core source. The spectral

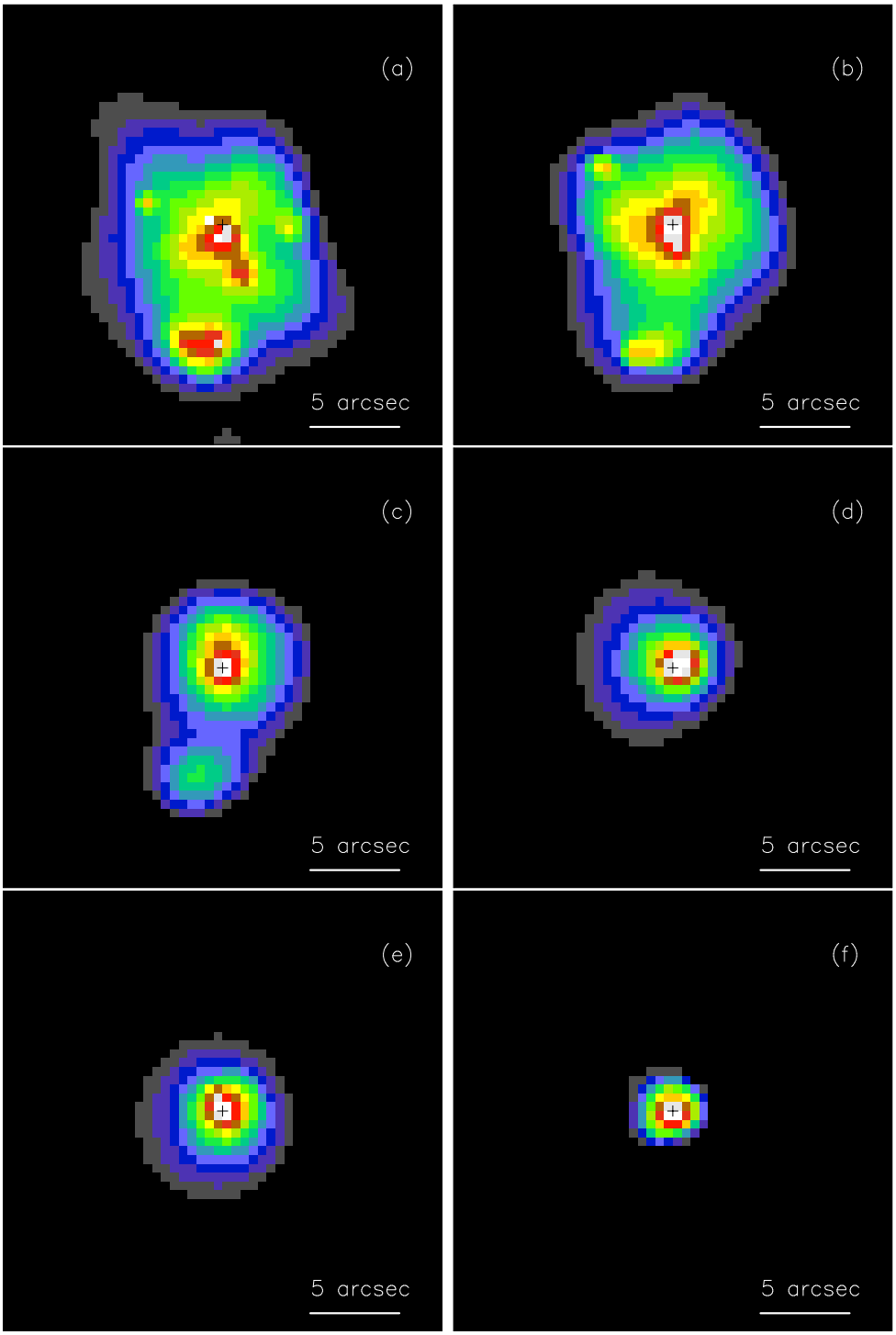

Figure 3.4: The *Chandra* X-ray intensity images of NGC 2782 in the selected energy intervals. Panels (a)-(f) display the central 10″ X-ray images of NGC 2782 with the core source marked by a cross in each image: (a) 0.5-1.0 keV; (b) 1.0-1.5 keV; (c) 1.5-2.0 keV; (d) 2.0-2.5 keV; (e) 5.0-8.0 keV; (f) 6.0-6.5 keV. The white bars represent 5″.

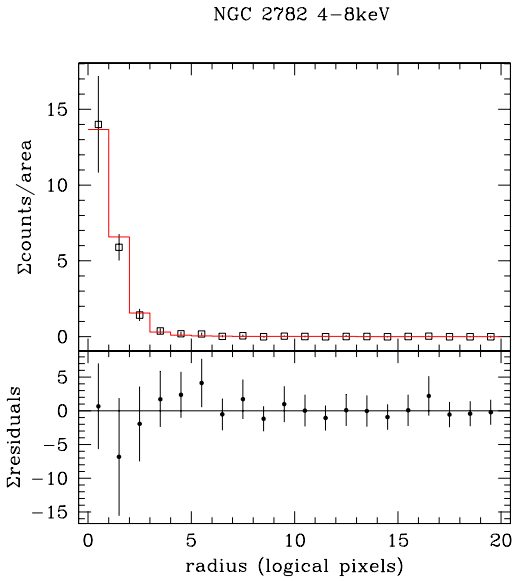

Figure 3.5: Radial profile of the core source of NGC 2782 in the 4-8 keV energy band. The observed profile is given by the squares with errorbars, the model-with the red solid line in the upper panel. The lower panel displays the fit residuals.

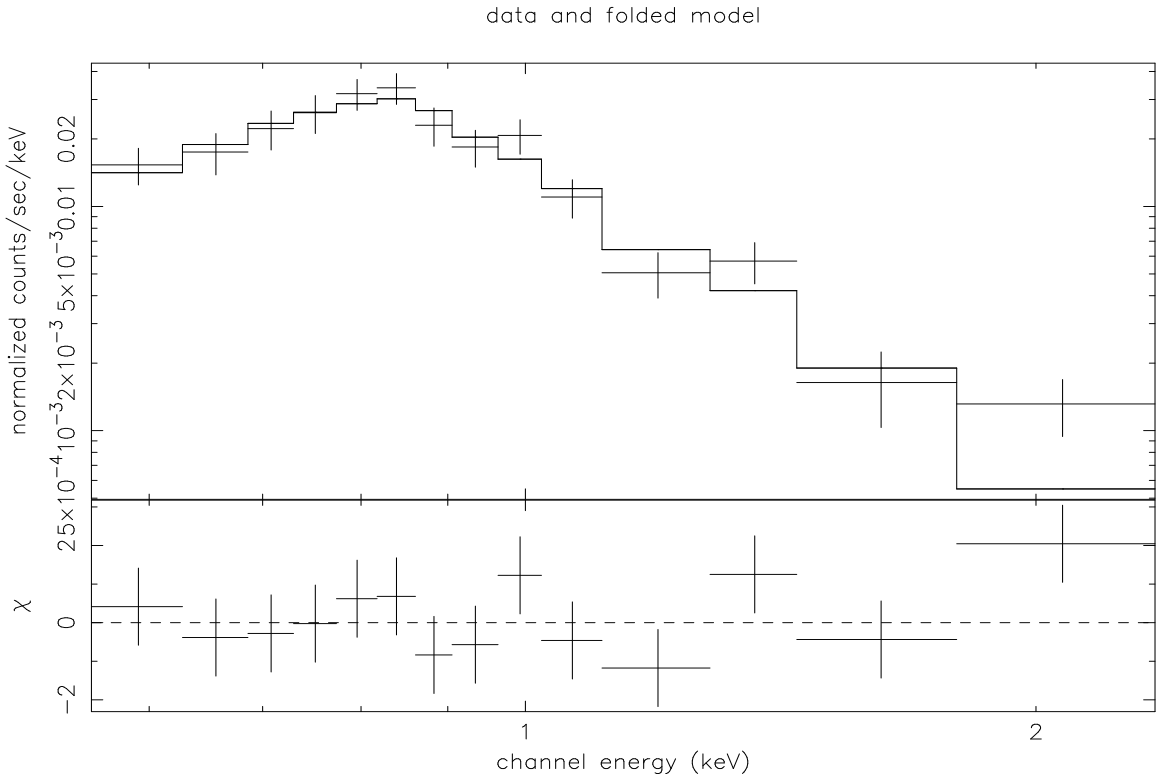

Figure 3.6: *Chandra* ACIS X-ray spectrum of the large-scaled extended X-ray emission of NGC 2782. The panel shows the observed spectrum with crosses. The solid line represents the best-fit one temperature thermal MEKAL model. The residuals are shown in the lower panel.

Table 3.1: Spectral fits to the X-ray spectrum of the weak large-scale extended emission of NGC 2782. $*$ denotes the fixed parameter: the Galactic column density $N_{\rm H,Gal}$.

$N_{\rm H}$	$k\mathbf{T}$	$\mathbf{Z}$	$L_{0.5-2.5keV}$	χ^2_{red}
10^{20} cm^{-2}	[keV]	[Z$_\odot$]	[10^{40}erg s^{-1}]	(d.o.f.)
1.8^*	$0.58^{+0.06}_{-0.07}$	$0.08^{+0.07}_{-0.04}$	1.7	1.03 (11)

Table 3.2: Spectral fits to X-ray spectra of the inner 10″ extended region *excluding* the compact core source.

$N_{\rm H}$	$k\mathbf{T}$	$\mathbf{Z}$	$L_{0.5-2.5keV}$	χ^2_{red}
10^{22} cm^{-2}	[keV]	[Z$_\odot$]	[10^{40}erg s^{-1}]	(d.o.f.)
$0.10^{+0.10}_{-0.02}$	$0.69^{+0.13}_{-0.05}$	$0.10^{+0.02}_{-0.03}$	5.2	1.02(24)

fitting for this bright extended emission has been carried out from an annular region with an inner and outer radii of 2″ and 10″, respectively. (see Figure 3.7 and Table 3.2). The absorption-corrected luminosity is L$_x \approx 5.2\times10^{40}$ erg s^{-1}.

The spectrum of the shell-like emission south of the core source is extracted from an elliptical region centered at R.A.= $09^h14^m05.2^s$, decl.=40°06′43″, (ellipse radii: 3.″4 and 2.″0). We find that a thermal MEKAL model with a temperature of 0.45 keV and a metal abundance of $\sim$0.04Z$_\odot$ yields an acceptable fit. Since the column density can not be well constrained but likely to be close to the value for the inner bright extended emission, it is fixed to 10^{21} cm^{-2}. The model-dependent X-ray luminosity is 4.5 $\times$ 10^{39} erg s^{-1}. If we assume there is a "hidden" counterpart of this southern shell-like emission, it could be present at 5-8″ north of the core source. The upper limit of the luminosity of the "hidden" counterpart determined by using the MEKAL model with the same parameters is 0.7 $\times$ 10^{39} erg s^{-1}.

3.4.2 The compact core source

More than 90% of the hard X-ray photons originate from the inner 2″ region; outside this region the soft X-ray emission becomes dominant. This is consistent with the results from spatial analysis which suggest that the hard X-ray emission is dominated by the core point source emission. The core source emission is extracted from a circular region centered at R.A.= $09^h14^m05.1^s$, decl.=40°06′49.2″, with a radius of 2″. Since the extended soft X-ray component is projected onto the area of the core source, we expect the soft and hard X-ray emission to overlap spatially in the core area.

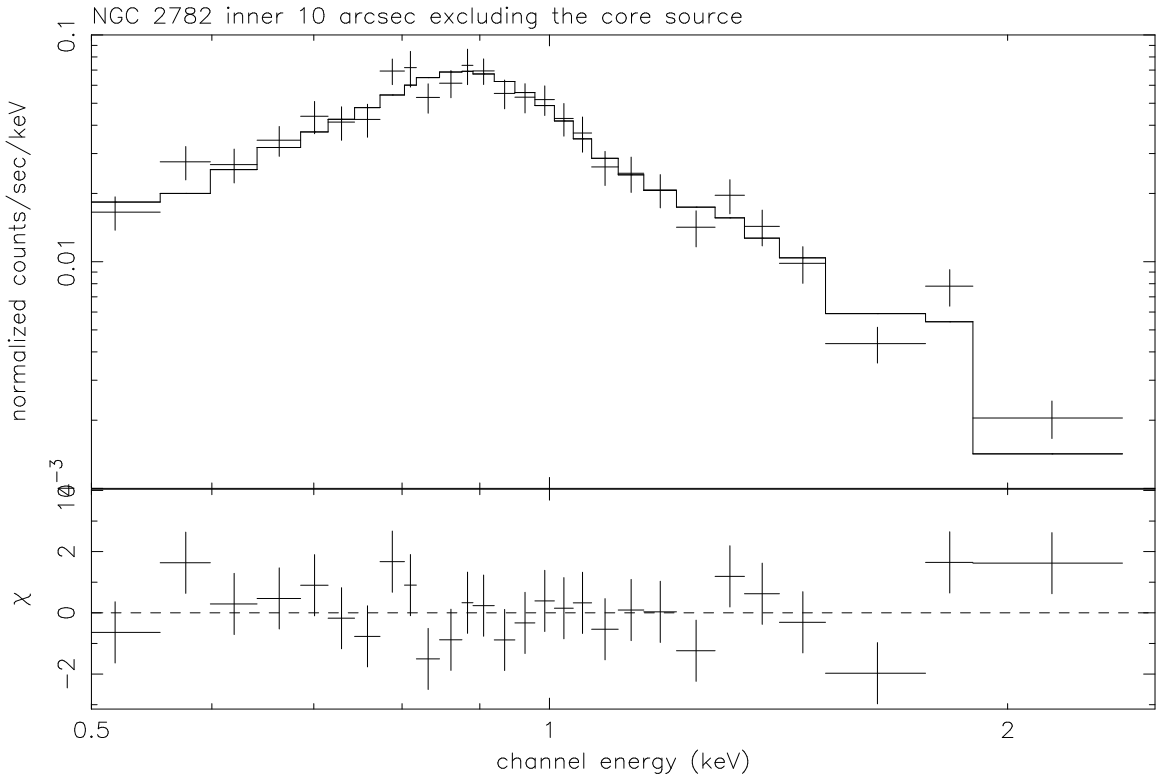

Figure 3.7: *Chandra* ACIS X-ray spectrum of the inner 10″ extended X-ray emission of NGC 2782, *excluding* the compact core source. Panels and residuals as in Figure 3.6.

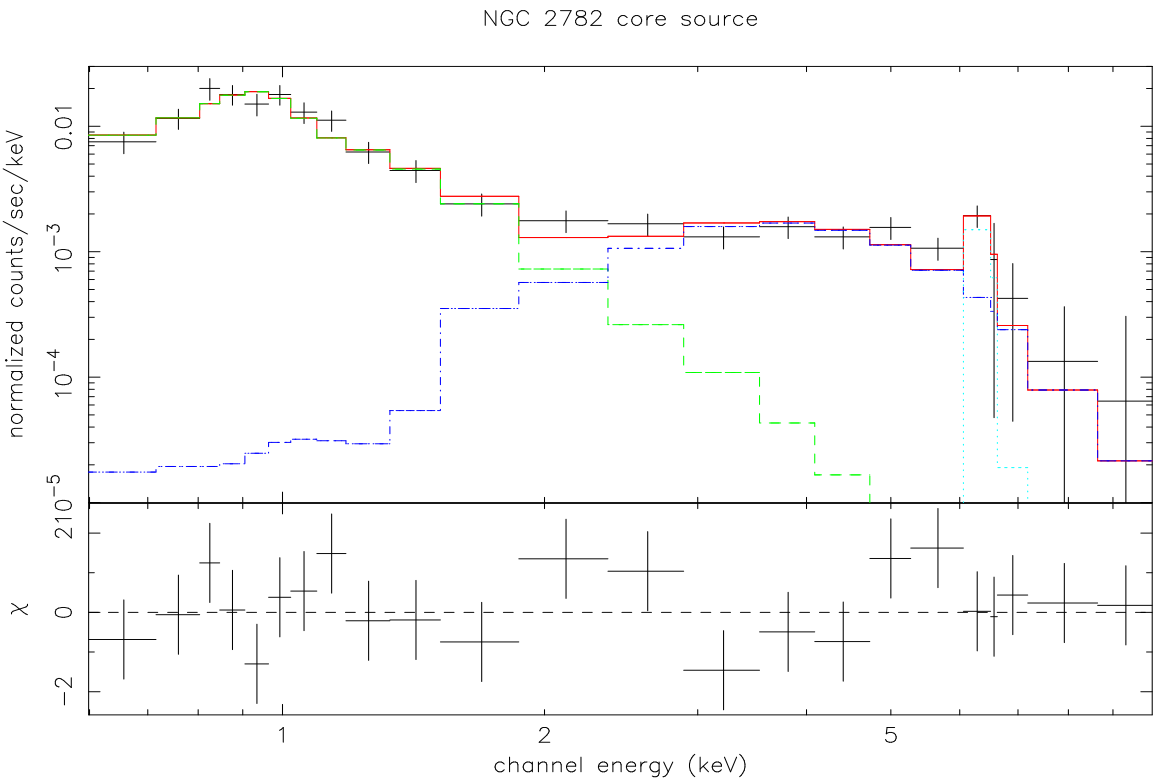

Figure 3.8: The *Chandra* ACIS X-ray spectrum of the compact core source in NGC 2782. The model consists of a thermal MEKAL and a power-law continuum. The red line denotes the full model fit, with the MEKAL and power-law components given by the green and blue curves, respectively.

The soft X-ray emission is ascribed to the previously determined MEKAL component. Though the hard X-ray spectrum can be fitted either as a power-law continuum or a thermal bremsstrahlung continuum, the latter is ruled out here, because the derived temperature from the spectral fitting is unrealistically high. Thus, the spectral model of the core source consists of a MEKAL model plus a power-law component.

If the hard X-ray emission is attributed to a single power-law model, a significant excess of counts is obvious in the 6-7 keV range, whether the photon index is set as a free parameter or fixed to 1.9 (see Figure 3.9). This indicates the presence of strong iron K shell emission line from the core source. Fitting the data with a narrow (σ = 0.1 keV) Gaussian line yields a better fit ($\triangle\chi^2$ = 8.6, for two more parameters.) Therefore, the addition of a Gaussian line is justified. In summary, the model F for the core source can be written as: $F = Wa*[MEKAL+Wa*(Powerlaw+Zgauss)]$. Table 3.3 shows the details of the spectral fitting for the core source, the spectrum itself is shown in Figure 3.8. The best-fit gives E = $6.37^{+0.14}_{-0.28}$ keV for the Gaussian line energy, and the contour plot in the energy and normalization plane is shown in Figure 3.10. The emission line is more likely to be the neutral fluorescence iron line, further weakening the case for a thermal plasma accounting for the hard X-ray components. The observed intensity of the neutral line corresponds to an equivalent width of $\sim$ 900 eV. The explanation for the nature of the core source will be discussed in Section 3.5.2.

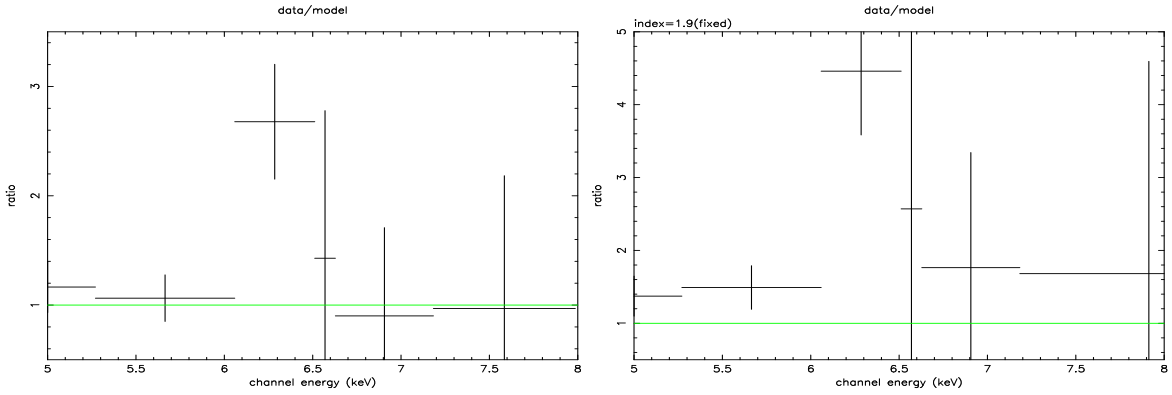

Figure 3.9: Data/model ratio in the 5-8 keV range. Left: Data/model ratio in the 5-8 keV range with the photon index of the power-law component free to vary. Right: same for the photon index fixed to 1.9.

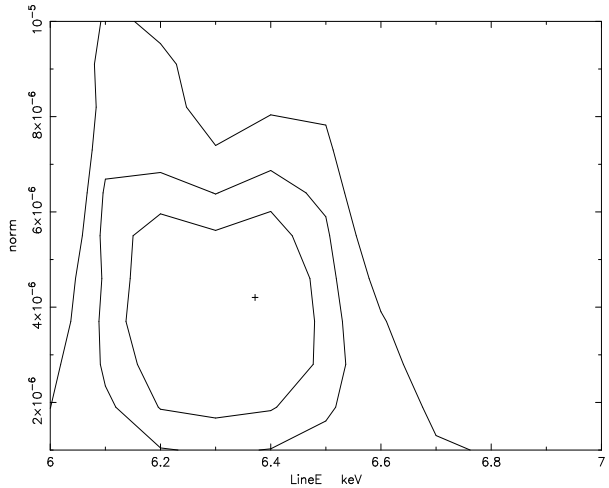

Figure 3.10: χ^2 contour plots in the Normalization-Energy space with solid line contours indicating the 68%, 90%, and 99% confidence contours for the best-fit model of the core source.

Table 3.3: Spectral fits to the compact core source of NGC 2782. ($*$:10^{-6} photons cm^{-2} s^{-1} keV^{-1} at 1 keV.)

MEKAL			PL+line					
$N_{\rm H}$	k**T**	**Z**	$N_{\rm H}$	Γ	$E_{\rm line}$	**Norm**	$L_{0.5-10.0keV}$	
(10^{20} cm^{-2})	(keV)	(Z$_\odot$)	(10^{22} cm^{-2})		(keV)	($*$)	(10^{41}erg s^{-1})	χ^2_{red} (d.o.f.)
0.1(fixed)	$0.80^{+0.10}_{-0.08}$	$0.15^{+0.07}_{-0.06}$	1^{+3}_{-1}	$-0.08^{+0.16}_{-0.20}$	$6.37^{+0.14}_{-0.28}$	$4.2^{+2.2}_{-2.6}$	1.3	0.24 (113)

3.5 Discussion

3.5.1 The X-ray Starburst-driven Superwinds

The soft X-ray morphology of NGC 2782 can be studied in detail using the high-resolution *Chandra* images, in which the bipolar soft X-ray emission extends north-to-south. The most significant feature in the southern extended region is the shell-like structure 5-8″ south of the central emission. Though the northern part has no obvious shell-like emission, the weak soft X-ray emission due to diffuse hot gas can be traced out to a distance of 30″ (5 kpc), two times further the southern extended emission. The large-scale N-S extent of the X-ray extended emission of NGC 2782 can be interpreted as starburst-driven superwind, preferentially oriented along the minor axis of the galaxy. Thermalized kinetic energy from the massive stars in the starburst creates a hot(10^8 K) bubble in the ISM. This bubble expands, sweeping up ambient material into a dense shell. The shell becomes broken into fragments, and is carried along by the wind. The wind itself or ambient clouds overrun by the wind are the source of of optical emission line filaments, and possibly the soft X-ray emission (e.g. Heckman et al. 1993b, Strickland et al. 1997).

The correlations between the X-ray emission and the optical/RC emission provide important evidence for the starburst-driven superwinds in NGC 2782. To study the correlation between the X-ray emission and the optical line emission, we used *HST* (WFPC-2) archival data. Figure 3.11 shows the X-ray contours overlaid on the Hα image. The Hα shell 5-8″ south of the core coincides spatially with the southern enhanced X-ray emission, indicating that they are related. The main difference between the Hα emission and X-ray emission lies in a clumpy arclike feature about 3″ north of the central peak emission present in the Hα image (Jogee et al. 1998) but absent in the X-ray contours. We also overlaid the X-ray image with the contours (black) of the RC emission (Saikia et al. 1994). The RC emission has a compact central source with two east-west secondary peaks and the north-south extended bubbles (Jogee et al. 1998). The overlay image (see Figure 3.12) indicates that the X-ray core emission is correlated with the RC peak and the southern RC shell-like structure spatially coincides with the X-ray southern enhanced emission. Like the Hα emission, the X-ray emission has no obvious structure corresponding to the RC north bubble structure.

Though no northern shell-like structure exists in the Hα emission image, the north bubble is clearly seen in the RC image. The RC emission is produced when relativistic electrons undergo synchrotron losses or inverse Compton scattering. The *Chandra* soft X-ray images do show a weak extended emission north of the core source. What is the reason for the disappearance of the shell-like structure in the northern extended emission in both the X-ray and optical images? One plausible explanation is that the shock heating is not sufficient to produce either the observed soft X-ray or the optical emission in the northern extended region. The density of the ISM/ambient clouds might be too low to form a dense shell overrun by the wind. If fewer ISM/ambient clouds interact with the hotter matter in north region, the X-ray emission observed in the north region would be fainter, and no clear shell feature would be observed.

Another possibility comes from the consideration of the geometry of NGC 2782 proposed by Boer et al. (1992): north of the center, the contribution of the backside

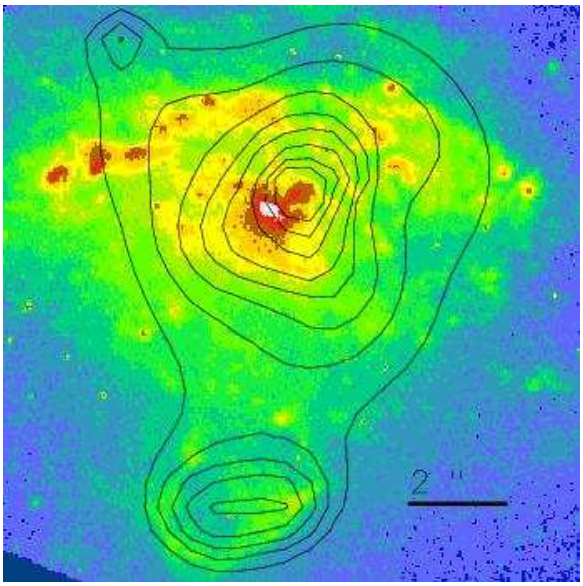

Figure 3.11: X-ray contours (black) overlaid on the Hα (*HST* WFPC-2) image of NGC 2782. The contour levels are 1, 1.5 ,2 ,2.5 ,3 ,4 ,5 ,6σ above the background. The Hα shell-like structure 5-8$''$ south of the core source coincides with the southern enhanced X-ray emission. The clumpy, arclike feature about 3$''$ north of the nucleus seen in the Hα image is not visible in the X-ray contour image.

shell is hidden by dust in the side of the disk nearest to us. As shown in the *HST* V band (F555w)image, a set of striking dust lanes exists about 4$''$ north of the center, running approximately east-west (Jogee et al. 1998, 1999). Due to stronger absorption in the northern region, many more X-ray photons are absorbed in this region than in south, and therefore no shell feature can be seen north of the center. The absence of the northern shell-like structure is therefore consistent with the view that the northern part of the outflow is viewed through the disk because soft X-rays are more easily absorbed.

It is worth emphasizing that the coincidence of X-ray and optical structure is expected exist only in those areas where the X-ray and optical emitting gases are well intermixed. Thus, the correlation is not expected to hold everywhere; for example, the fact that the clumpy arclike feature about 3$''$ north of the central peak emission in the Hα image (Jogee et al. 1998) has no X-ray counterpart, is perhaps not surprising.

3.5.2 The nature of the compact core source

A LLAGN or an obscured AGN?

An important question is what is the nature of the core source. The X-ray luminosity (0.5-10 keV band) of the core source is 1.3 10^{41} erg s^{-1}, fainter than $L_x \sim 10^{42}$ erg s^{-1} which is usually taken as indicative for the presence of a 'normal' AGN.

As mentioned above, the core source is detected in the hard X-ray energy band with S/N of 5.4 and a point source morphology. A neutral iron line is also observed at

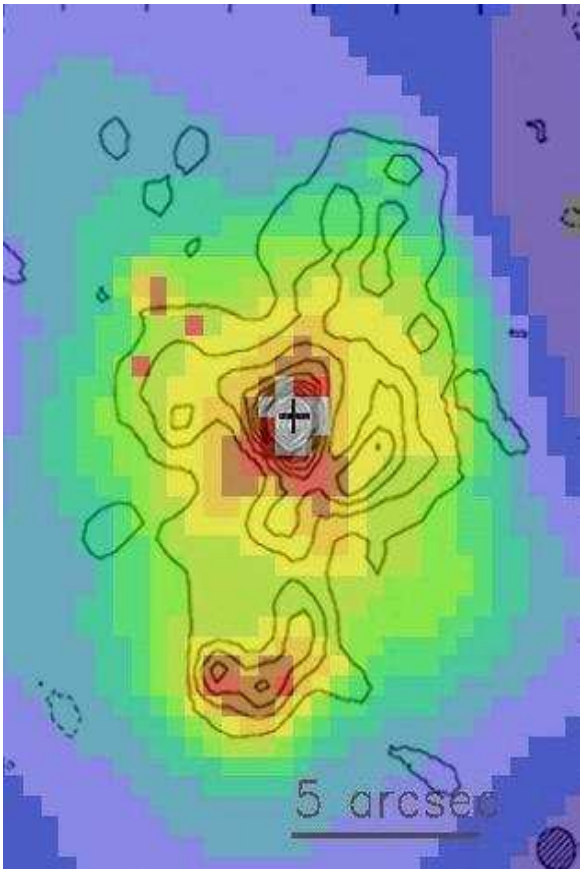

Figure 3.12: 5 GHz radio continuum contours (black) superposed on the X-ray intensity image. The contour levels (Saikia et al. 1994) are 5%, 10%, 30%, 50%, 70%, 90% and 100% of the peak flux (3.97 mJy per beam). The X-ray core source is marked by a cross. The black bar represents 5 arcsec.

Table 3.4: The predicted soft X-ray luminosities derived from the correlation with Hα luminosities (Halderson et al. 2001). Luminosities are given in units of erg s^{-1}.

$L_{H\alpha}$ (extinction-corrected)	L_x (0.1-2.4 keV, predicted)
8.4×10^{41} (Boer et al. 1992)	5.9×10^{42}
7.2×10^{41} (Ho et al. 1997)	5.0×10^{42}
10.9×10^{41} (Usui et al. 2001)	7.6×10^{42}

6.4 keV, which could indicate either a LLAGN or an obscured AGN.

The X-ray to optical flux ratios can be used as a discriminator of the underlying emission process within the core source region. Halderson et al.(2001) found a correlation between the soft X-ray and Hα luminosities of LLAGNs in their sample. The mean $L_x/L_{H\alpha}$ ratio for LLAGN is 7. L_x is the soft X-ray (0.1-2.4 kev) luminosity in units of erg s^{-1}. $L_{H\alpha}$ is the luminosity of the extinction-corrected Hα emission line. Table 3.4 shows the details of the predicted soft X-ray luminosities derived from the $L_{H\alpha}$ of NGC 2782 estimated by three different authors. The observed X-ray (0.1-2.4 keV, absorption-corrected) luminosity is 2.1×10^{40} erg s^{-1}, lower by more than 2 orders of magnitude, compared with those inferred from de-reddened Hα luminosity, which may suggest either that the core source cannot be attributed to a LLAGN, or that the line of sight to the AGN is heavily obscured in X-rays, probably Compton-thick.

If a heavily obscured AGN is present, we only see the X-ray emission scattered by a warm and/or cold reflector. If the scattering fraction is a few percent, an upper limit of the intrinsic X-ray luminosity is calculated approximately to be $\approx 10^{43}$ erg s^{-1}. The iron fluorescence emission line at 6.4 keV originates from a cold material irradiated by the primary X-ray source (e.g. Lightman & White 1988, George & Fabian 1991). The large equivalent width of the line is expected when the X-ray source is obscured by a high column density typically larger than 10^{23} cm^{-2} (Makishima 1986). Thus the strong observed iron emission line at 6.4 keV with an equivalent width of $\approx$ 900 eV in NGC 2782 suggests the presence of an obscured X-ray source. The equivalent width of the Fe Kα line can be a good indicator of the absorbing column density (e.g. Ghisellini et al. 1994). Ghisellini et al. (1994) calculate equivalent widths of the fluorescence iron line produced by the torus as a function of $N_{\rm H}$. For a geometrical structure with the half-opening angle $\sim 45°$, the plot of equivalent widths of the 6.4 keV line dependent to the column density is shown in Figure 3 of Ghisellini et al. (1994). The equivalent width in NGC 2782 is 900 eV, which corresponds to column density $N_{\rm H} \sim$ 2-3 $\times 10^{24}$ atoms cm^{-2}, indicating a Compton-thick source.

I also consider the correlation known to exist between hard X-ray(2-10 keV) and [O III] luminosities (Mulchaey et al. 1994). For Seyfert 1 and 2 galaxies, the ratio log $L_{[OIII]}/L_{HX}$ is typically -1.89 and -1.76, respectively. Table 3.5 gives the predicted hard X-ray luminosities for NGC 2782. The observed X-ray (2-10 keV, absorption-corrected) luminosity is 1.1×10^{41} erg s^{-1}, with an upper limit of 1.4×10^{41} erg s^{-1}

Table 3.5: The predicted hard X-ray luminosities derived from the correlation with [O III] luminosities (Mulchaey et al. 1994). Luminosities are given in units of erg s^{-1}.

$L_{[OIII]}$ (extinction-corrected)	L_x (2-10 keV, predicted)
4.6×10^{41} (Boer et al. 1992)	3.6×10^{43}
2.5×10^{41} (Ho et al. 1997)	1.9×10^{43}
5.6×10^{41} (Usui et al. 2001)	4.3×10^{43}

calculated by varying the index of the power-law model, etc. Again, the observed X-ray luminosity, even the upper limit, is substantially less than those predicted by the observed [O III] luminosity, which might be an indication that X-ray emission is being observed indirectly, with only a fraction of the total luminosity reaching our line of sight.

The diagnostic diagram of the $F_x/F_{[OIII]}$ versus $F_{[OIII]}/F_{IR}$ ratio [1] is shown in Figure 3.13. The ratios are used to distinguish between the contribution of the AGNs and starburst components (Panessa & Bassani 2002), because the [O III] λ5007 emission is related to the AGN activity while the infrared emission is related to the star forming activity. As pointed out by Panessa & Bassani (2002), the column density could be inferred from the flux ratio of the X-ray fluxes versus the isotropic [O III] λ5007 flux. The diagram shows that NGC 2782 can be classified as Compton-thick AGN. This indicates large absorption in agreement with the results from spectral fitting; i.e., the existence of the neutral iron line emission with large equivalent width.

Starburst component?

After discussing the possibility of the existence of a LLAGN or an obscured AGN in NGC 2782, we examine the possibility that all of the hard X-ray emission is related to a nuclear starburst here. As discussed in Section 2.4.2, X-ray binaries can contribute significantly to the hard X-ray emission, and there is a correlation between the X-ray luminosity in 2-10 keV energy band $L_{2-10keV}$ and the SFR presented by Nandra et al.(2002), Grimm et al. (2003), Ranalli et al. (2003), and Persic et al. (2004).

Assuming that the infrared luminosity also originates in a starburst, we can use the correlation between the infrared luminosity L_{FIR} and the SFR (Kennicutt 1998) to estimate the upper limit of the SFR. The derived SFR for NGC 2782 is 6 $M_\odot$ yr^{-1}.

From the $L_{2-10keV} \sim$ SFR and the $L_{FIR} \sim$ SFR correlations, a newly derived correlation between the infrared luminosity L_{FIR} and the X-ray 2-10 keV luminosity $L_{2-10keV}$ can be obtained. Figure 3.14 shows the correlation between the two luminosities. Even when the lower limit of the X-ray 2-10 keV luminosity of 8.1×10^{40} erg s^{-1}

[1] The IR flux is defined (Helou et al. 1985) as a combination of *IRAS* 60 μm and 100 μm fluxes, $f_{IR} = 1.26 \times 10^{-11}$ (2.58 $f_{60} + f_{100}$) erg s^{-1} cm^{-2}, where $f_{60} = 9.17$ Jy and $f_{100} = 13.76$ Jy (Sanders et al. 2003).

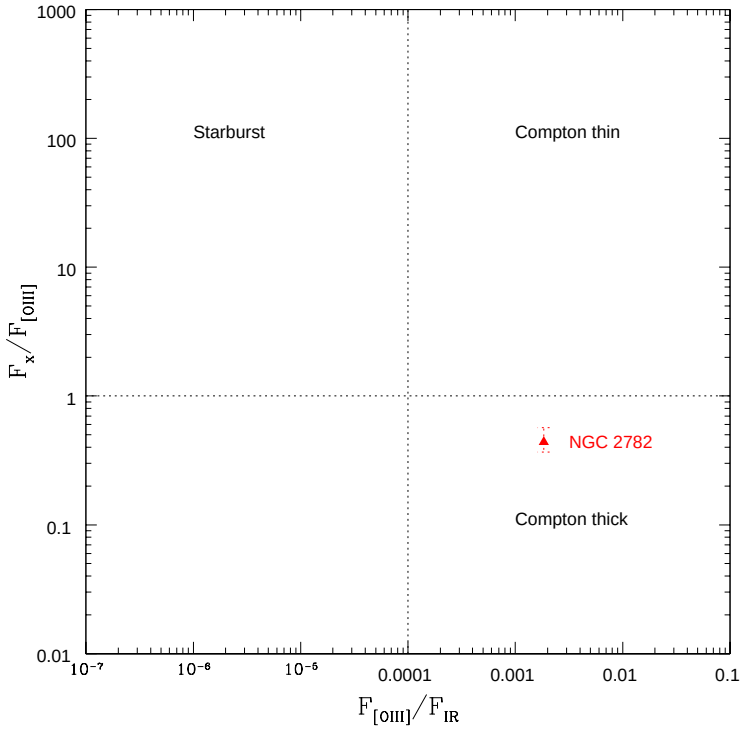

Figure 3.13: $F_x/F_{[OIII]}$ versus $F_{[OIII]}/F_{IR}$. Compton-thin, Compoton thick, and starburst regions (as derived from Panessa & Bassani 2002) are delineated by dotted lines.

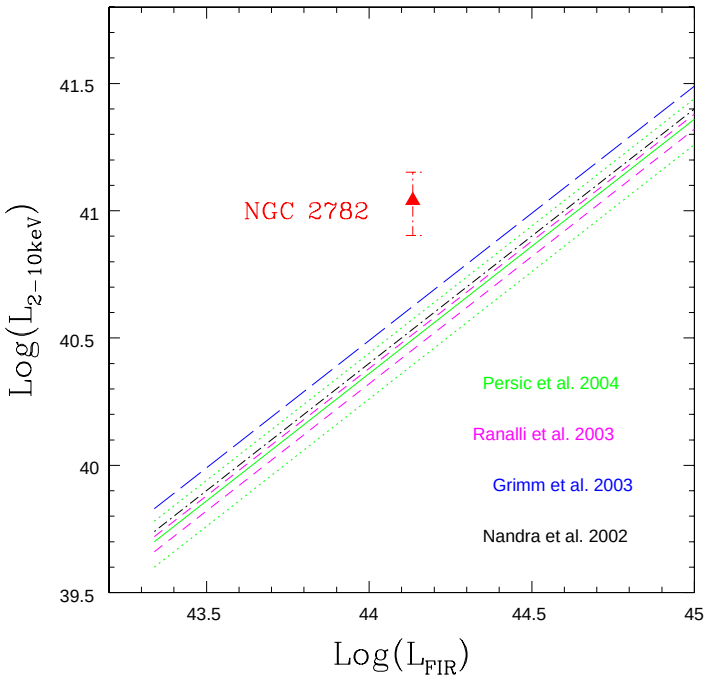

Figure 3.14: The X-ray 2-10 keV luminosity versus the infrared luminosity for NGC 2782. Lines represent the X-ray luminosities from the star formation rate by different authors as noted in the text.

is considered (obtained by varying the index of the power-law model and assuming the lowest possible column density) the observed hard X-ray luminosity is higher than the expected value produced by the starburst component by at least a factor of 2. Although the discrepancy is not very large, it likely indicates that the starburst component is not sufficient to produce the observed 2-10 keV X-ray luminosity in NGC 2782.

It is also worth noting that the energy of the iron line emission is about 6.4 keV from the spectral fitting, which is hard to explain by the starburst component.

ULX?

An alternative explanation for the origin of the hard power-law component and the iron emission line is the presence of an Ultra-luminous X-ray source (ULX) in the center. Non-nuclear point-like sources with X-ray luminosities on the order of 10^{37-40} erg s^{-1} have been detected in many nearby galaxies. The typical spectrum of a *Chandra* ULX can be described by a simple power-law with photon index $1.8 \leq \Gamma \leq 2.9$, steeper than the value obtained in our spectral analysis (Strickland et al. 2001; Roberts et al. 2002). If we arbitrarily set the index to 1.9, the lower limit of the luminosity (0.5-10.0 keV) is 5.6×10^{40} erg s^{-1}. According to the correlation between the maximum luminosity of the ULX in a galaxy and the star formation rate by Gilfanov (2004), the expected, maximum luminosity of the ULX in NGC 2782 is in the range of (0.5-1.4) $\times$ 10^{40} erg

s^{-1}. Hence, the lower limit of the luminosity is slightly larger than that expected from the maximum luminosity of the ULX. Moreover, The lower limit of the luminosity somewhat exceeds the typical maximum luminosities of the known ULXs (a few 10^{40} erg s^{-1}). Therefore, we can not firmly rule out the possibility that the core source of NGC 2782 is an ULX.

3.6 Summary

I presentd a detailed investigation of the X-ray emission of NGC 2782 using *Chandra* high-resolution imaging spectroscopy. This work shows the following:

- The starburst-driven outflow morphology of NGC 2782 is observed in the soft X-ray band, clearly seen in the narrow range images. The bipolar emission extends North-to-South. The northern extended emission is more elongated than the southern. In the central region, the compact core source is prominent in the hard X-ray (2-8 keV) band.

- A shell-like structure 5-8″ south of the core source is detected in all X-ray, Hα and radio images. The absence of a northern bubble can be interpreted either as insufficient shock heating to produce the bubble structure, or heavy absorption due to dust in the galactic disk.

- The emission from the starburst bubble is thermal. The temperature ranges between 0.6 and 0.7 keV.

- The emission from the compact core source may be the reflected/scattered component of an AGN. The direct component is so heavily absorbed that only a fraction of the total luminosity is observed. However, the possibility of an ULX in the center of NGC 2782 can not be ruled out, even though we consider it unlikely.

- Five off-nuclear point sources are detected in NGC 2782. The brightest one has a luminosity of $\sim 10^{40}$ erg s^{-1}.

APPENDIX

In order to predict the soft- and hard-band X-ray luminosities of NGC 2782, the fluxes of both Hα and [O III] emission are needed. The extinction correction for the fluxes of NGC 2782 are reported in this appendix.

If we suppose an AGN behind a dust screen which is the simplest source/dust geometry, the intrinsic flux $f_{int}(\lambda)$ is derived from the observed flux $f_{obs}(\lambda)$ via

$$f_{int}(\lambda) = f_{obs}(\lambda)10^{0.4E(B-V)k(\lambda)}$$

where $k(\lambda)$ is the total-to-selective extinction only dependent on the wavelength, and $E(B-V)$ is the color excess (see Calzetti 2001 for a review). The ratio of the observed-to-intrinsic Balmer line ratio can be expressed:

$$\frac{[L(H\alpha)/L(H\beta)]_{obs}}{[L(H\alpha)/L(H\beta)]_{int}} = 10^{0.4E(B-V)[k(H\beta)-k(H\alpha)]}$$

For a foreground, homogeneous, nonscattering dust screen and a Milky Way extinction curve for diffuse ISM, $k(V) = 3.1$, $k(H\alpha) = 2.5$, and $k(H\alpha) - k(H\alpha) = 1.1$ (Cardelli et al. 1989). The [O III] fluxes can be corrected for optical reddening by using the relation

$$f_{cor}([OIII]) = f_{obs}([OIII]) \left[\frac{[L(H\alpha)/L(H\beta)]_{obs}}{[L(H\alpha)/L(H\beta)]_{int}}\right]^{3.0}$$

where $[L(H\alpha)/L(H\beta)]_{obs}$ is the observed luminosity ratio, and $[L(H\alpha)/L(H\beta)]_{int}$ the intrinsic luminosity ratio. $[L(H\alpha)/L(H\beta)]_{int}$ is essentially insensitive to the physical conditions of the gas, being 3.03 for temperature T = 5,000 K, 2.86 for T = 10,000 K, and 2.74 for T = 20,000 K (Osterbrock 1989). Since variations in this ratio only amount to about 5-10 % due to the variations in the temperature, we fixed $[L(H\alpha)/L(H\beta)]_{int}$ to 3.

The emission-line fluxes were obtained from the literature by different authors. Only high signal-to-noise data ratios are used in this thesis.

Boer et al. (1992) measured the intrinsic $H\beta$ luminosity to be 2.8 $\times$ 10^{41} erg s^{-1} and $[L(H\alpha)/L(H\beta)]_{obs} = 7$ for the center (including the narrow line region). If the measured line ratio $[L([OIII])/L(H\beta)]_{obs} = 1.68$ is used with the position angle PA $\sim$ 0° (see Table 2 in Boer et al. 1992), the observed [O III] luminosity $L([OIII])_{obs}$ is 3.2 $\times$ 10^{40} erg s^{-1}. Then, we have the intrinsic Hα luminosity $L(H\alpha)_{int} \sim 8.4 \times 10^{41}$ erg s^{-1}, and the intrinsic [O III] luminosity $L([OIII])_{int} \sim 4.6 \times 10^{41}$ erg s^{-1}.

The optical spectroscopy observation of the nuclear region (r $\sim$ 200 pc) of NGC 2782 is presented by Ho et al. (1997) as part of a survey of nearby galaxies. The apertures are large enough that most of the [O III] emission coming from the narrow line region is included, if assuming an AGN exists in the nuclear region of NGC 2782. The contribution to the [O III] flux outside this aperture is negligible, since it is believed to originate in the circumnuclear star-forming regions. In this observation, the observed Hα flux is 3.7 $\times$ 10^{-13} erg s^{-1} cm^{-2}, the line intensity ratio of [O III] emission relative to Hα is 0.16, and $[L(H\alpha)/L(H\beta)]_{obs} = 6.5$ (see Table 2 and 4 in Ho et al. 1997). We

estimate the intrinsic Hα luminosity $L(H\alpha)_{int} \sim 7.2 \times 10^{41}$ erg s^{-1}, and the intrinsic [O III] luminosity $L([OIII])_{int} \sim 2.5 \times 10^{41}$ erg s^{-1}.

According to the observations of Usui et al. (2001), the intrinsic Hα luminosity is 10.8×10^{41} erg s^{-1}, and the intrinsic [O III] luminosity is 5.6×10^{41} erg s^{-1} .

CHAPTER 4
NGC 1386

4.1 Introduction

NGC 1386 is a nearby Seyfert 2 galaxy (z=0.002895, D∼11Mpc for H_0= 71 km s^{-1} Mpc^{-1}; $1'' = 52$ pc) viewed at high inclination ($i \simeq 71°$), and located near the center of the Fornax cluster (Philips & Frogel 1980; Phillips, Charles and Baldwin 1983). NGC 1386 is the subject of various studies by a series of authors. It was detected in the soft X-ray band with the *Einstein Observatory*, with $L_{0.2-3.5keV} \sim 1.4 \times 10^{40}$ erg s^{-1} for a distance of 11 Mpc (Fabbiano et al. 1992). The X-ray spectrum of NGC 1386 obtained from *ASCA* by Iyomoto et al. (1997) consists of an absorbed power-law and a strong 6.4 keV Fe Kα emission feature with an equivalent width of 1.6 keV, characterized by a large absorbing column (3×10^{23} cm^{-2}). NGC 1386 is part of a sample of 11 Compton-thick AGNs studied by Guainzazzi et al. (2005). They present the result of an *XMM-Newton* observation of NGC 1386 and classify it as a reflection-dominated object. The presence of the strong Fe Kα line is also confirmed by the *Chandra* ACIS-S observations (Bianchi et al. 2006).

For NGC 1386, two physical interpretations of the soft X-ray emission have been discussed: (i) thermal emission from optically thin, collisionally ionized plasma (Guainzazzi et al. 2005), and (ii) reflection of the nuclear continuum from gas photoionized by the central AGN, which was tested with the CLOUDY code (Bianchi et al. 2006). In the latter scenario, the scattering medium located at ionized cones, along the axis of the torus (as in NGC 1068, Antonucci & Miller 1985; Marshall et al. 1993) has a direct view of the nucleus, while we have an unobscured view towards the scattering gas. Then the X-ray emission consists of scattered nuclear photons, and/or is produced within the scattering region itself. The soft X-ray spectrum is dominated by line emission from photoionization and photoexcitation by the central AGN (e.g. NGC 1068: Kinkhabwala et al. 2002; Brinkman et al. 2002; Ogle et al. 2003). Bianchi et al. (2006) also point out that the soft X-rays are spatially correlated with the [O III] emission, which indicates a connection between the soft X-rays and narrow-line-region (NLR). The size and properties of the NLR in NGC 1386 are well studied with optical long-slit spectroscopy by Bennert et al. (2006). They determined the radius of the NLR in NGC 1386 to be $6''$ ($\sim$ 300pc).

However, it should be kept in mind that Bianchi et al. (2006) did not include the flux of Fe-L emission around 1 keV when they stated that the soft X-ray spectra are dominated by emission lines produced in photoionized gas. The previous parameterizations are too simple to yield adequate fits for the spectra of NGC 1386.

In this chapter, we take advantage of *Chandra* ACIS-S data which are obtained with high spatial resolution ($\leq 1''$) imaging spectroscopy. The excellent resolution makes it possible to investigate the nuclear and extended emission separately. Here, we undertake a more detailed study of the existing data, with the goal of understanding better both the nuclear and the extended X-ray emission. This detailed study, combined with the morphological correlations between the X-ray emitting gas and the optical line structures, may allow us to determine the true nature of the X-ray emission in NGC 1386. The present chapter is organized as follows. The observations and data reduction

are described in Section 4.2; the detailed imaging analysis and spectral analysis are presented in Sections 4.3 and 4.4, respectively. the discussions of the X-ray properties of NGC 1386 is given in Section 4.5. the summary and conclusions are presented in Section 4.6.

4.2 Observations and data reduction

NGC 1386 was observed with the *Chandra* ACIS detectors on November 19, 2003, with a total exposure time of 19.89 ks. The nucleus of the galaxy was positioned on the ACIS-S detector. The standard Level 2 event files downloaded from the *Chandra* data archive, were filtered on good time intervals, resulting in an effective exposure time of 19.80 ks. The data were reduced and analyzed with the CIAO version 3.0.2 and XSPEC version 11.3.2 software packages. I checked the light curves extracted from an area of 0.35 arcmin^2 within the energy range of 0.1-10.0 keV and found no significant flares. No further cleaning the data to remove periods of high background levels was necessary, and the data within the standard good time intervals of 19.80 ks were used in the following analysis.

The Galactic column density toward NGC 1386, $N_{\rm H,Gal}$= 1.4 $\times$ 10^{20}cm^{-2}, is calculated based on the source position by using the data from Dickey & Lockman (1990).

4.2.1 Statistics

The data were binned to at least 15 or 20 counts bin^{-1}. The spectra were modelled using χ^2 statistics with XSPEC. We also modelled the unbinned data using Cash statistics (Cash 1979). The χ^2 statistics requires a Gaussian distribution of the counts in a bin, therefore, it can not describe well a finely binned or unbinned spectrum. The Cash statistics is the maximum likelihood statistics for the Poisson distribution, which can be applied to the Poisson distribution of counts per bin for a finely binned or unbinned spectrum and allow us to better constrain the fitting parameters. Unlike χ^2, the Cash statistics does not have an objective measure of the goodness of fit. To determine the goodness of fit, I used the "goodness" command in XSPEC which make use of Monte Carlo simulations. The "goodness of fit" should be around 50% if the observed data was produced by the fitted model.

4.3 Imaging analysis

The *Chandra* data reveal the complexity of X-ray emission of NGC 1386, as shown in the X-ray intensity images of Figure 4.1 (with a real-valued binning factor of 0.25 pixel). The X-ray emission of NGC 1386 consists of resolved extended regions and a compact nuclear source.

The extended emission dominates in the soft X-ray band (below 2 keV), as a function of energy. In the soft X-ray band, I consider six energy intervals separately: 0.1-0.5, 0.5-1.0, 1.0-1.5, 1.5-2.0, 2.0-8.0, and 6.0-6.5 keV (see Image (a), (b), (c), (d), (e) and (f) of Figure 4.1). The position of the soft X-ray maximum intensity (hereafter the soft X-ray nucleus) is marked by an asterisk in each image of Figure 4.1. The X-ray

emission in 0.1-1.0 keV band has the greatest spatial extent, which shows clear N-S elongated extended emission. Both the north and south parts of extended emission extend as far as 4″ from the nucleus along P.A. $\sim 5°$. Of special interest is the "blob" about 3″ north of the soft X-ray nucleus, hereafter "the northern blob". As X-ray energy becomes higher, the extended emission shrinks abruptly, fading for X-ray energies higher than 2 keV.

The hard X-ray emission (2-8 keV) is dominated by a compact source, hereafter "the hard X-ray nucleus". In Image (e) and (f) of Figure 4.1, the hard X-ray nucleus is marked by a cross. Note that the soft (denoted by an asterisk) and the hard (denoted by a cross) X-ray nuclei are separated by $\sim 0.4''$. The radial profile of the compact source in the 2-8 keV energy band is consistent with the PSF size (see Figure 4.2), indicating that there is no intrinsically extended hard emission.

Soft X-ray and optical-line/radio images

Correlations between the soft x-ray emission and the optical-line emission, if present, give important hints for the origin of the X-ray emitting gas. The narrow-band images of [O III] λ 5007 and [N II]$\lambda\lambda$6548,6583 + Hα emission lines were obtained with the *HST* (WFPC-2; observations prgID 6419). Before the *Chandra* and *HST* images are overlaid, any systematic shift of simultaneously detected sources should be identified and corrected. Unfortunately, no overlapping point sources are present in the fields of view of the *Chandra* and *HST* instruments. Therefore, the absolute pointing accuracy can not be improved.

In order to compare the soft X-ray emission with optical-line emission, I choose the location which has the optical maximum intensity as the optical nucleus in the *HST* images, and then assume that the soft X-ray and the optical nuclei coincide in Figures 4.3 and 4.4. Figure 4.3 shows the *Chandra* X-ray contours in the 0.1-0.5 keV energy band overlaid on the archival *HST* WFPC-2 [O III] and [N II]$\lambda\lambda$6548,6583 + Hα images of NGC 1386. Figure 4.4 illustrates the *Chandra* X-ray contours in the 0.5-1.0 keV energy band overlaid on the *HST* optical Hα and [O III] images. The figures suggest that the correlations exist between soft X-ray and optical emission. Both the soft X-ray and the optical images show bright nuclear emission and fainter bipolar extended emission. The extended emission in both the soft X-ray images and the optical images is preferentially elongated along PA $\sim 5°$. Note that the soft X-ray northern blob coincides with the bright northern [O III] blob. This coincidence suggestes that the enhanced soft X-ray emission from the northern blob is a separate feature, unlike the rest of the extended elongated emission, since the location of this blob is spatially correlated with a special region in which several signs for shocks are founded by Bennert et al. (2006). Further analysis and discussion of this issue are given in Sections 4.4.1 and 4.5.3.

In Figure 4.5, I overlaid the [O III] contours by Henrique Schmitt (Figure 1 of Bennert et al. 2006) on the soft X-ray images. Figure 4.5 shows again the overlap between the soft X-ray and the [O III] emission. Apart from the optical nucleus, the hidden optical nucleus is also marked in this *HST* [O III] image, $\sim 1''$ north of the optically bright nucleus. The distance between the optically bright nucleus and the hidden nucleus is larger than the separation between the soft and hard nuclei (1″ vs.

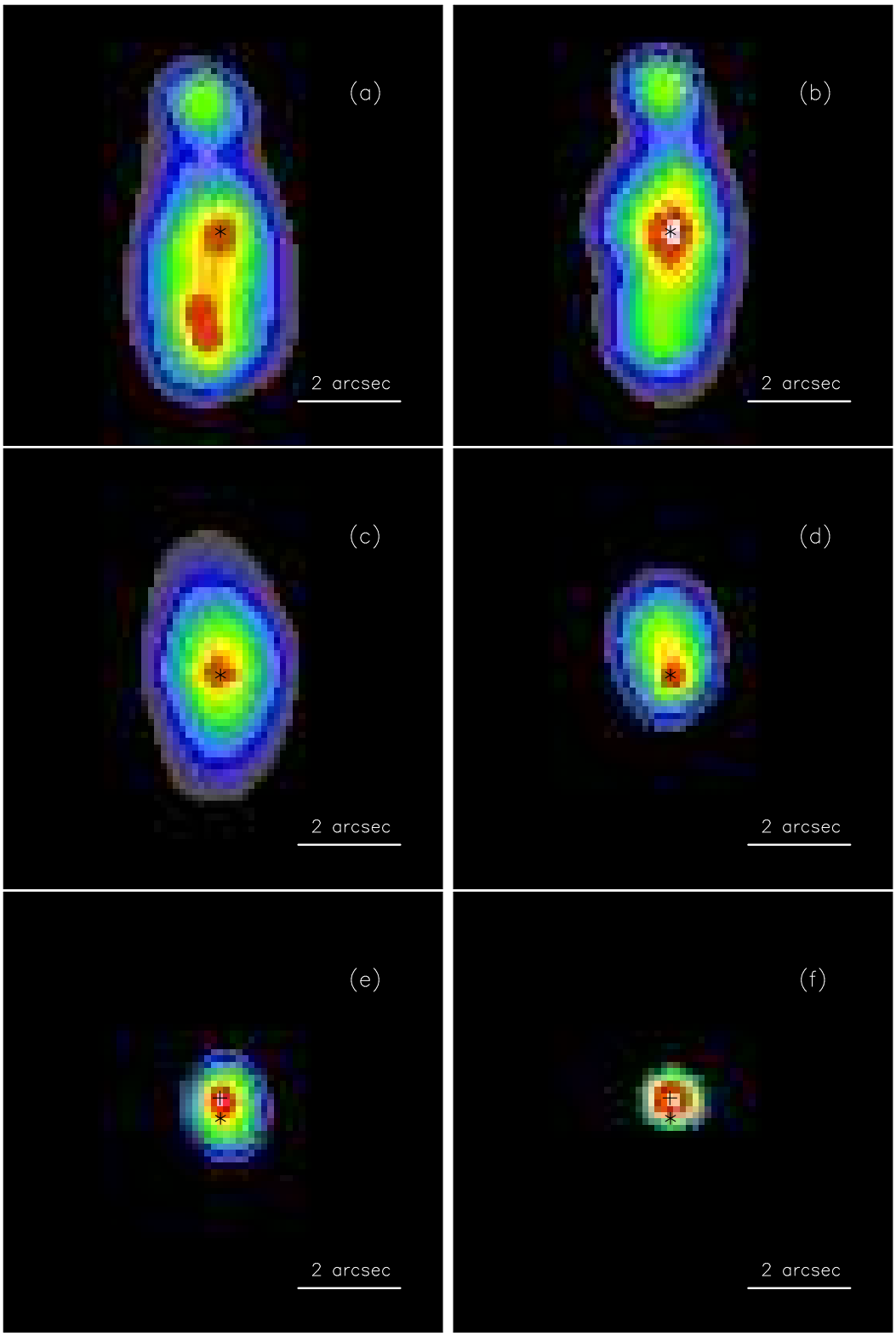

Figure 4.1: *Chandra* X-ray intensity images of NGC 1386 in the selected energy intervals. Panels (a)-(f) display the central 6″ of NGC 1386 with the soft X-ray nucleus of the galaxy marked by an asterisk in each image: (a) 0.1-0.5 keV; (b) 0.5-1.0 keV; (c) 1.0-1.5 keV; (d) 1.5-2.0 keV; (e) 2.0-8.0 keV; and (f) 6.0-6.5 keV. In (e) and (f), the crosses mark the positions of the hard X-ray nuclei. North is up and East is to the left.

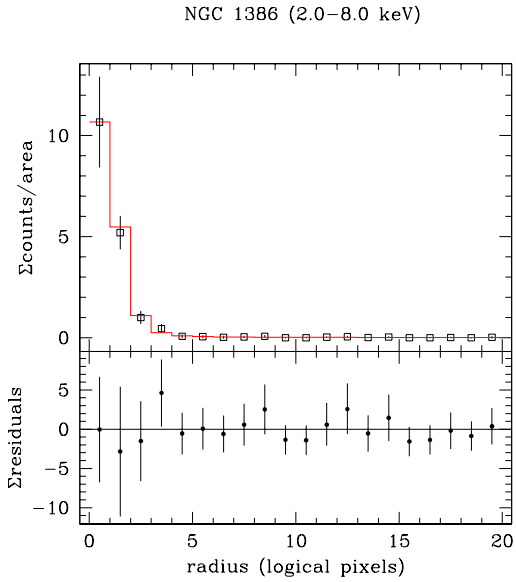

Figure 4.2: Radial profile of the hard X-ray nucleus of NGC 1386 in the 2-8 keV energy band. The observed profile is given by the squares with errorbars, the model-with the red solid line in the upper panel. The lower panel displays the fit residuals.

0.4″).

Of further interest is the alignment between the soft X-ray and the radio structures. We were unable to obtain meaningful results by comparison of the radio images (Figure 6 of Nagar et al. 1999) with the soft X-ray images, because of the lower resolution of the 20 cm radio image, and lack of the information of low surface brightness features in 3.6 cm radio image.

4.4 Spectral anaylsis

Considering the results obtained from the imaging analyses, I extracted X-ray spectra from three interesting regions, which are marked in Figure 4.6. (1) The core: a circular region with radius of 0.9″ centered at α= $03^h36^m46.^s176$, δ= -35°59′57.″43 (the blue circle in Figure 4.6). (2) the northern blob: a circular region with a radius of 1.2″, centered at α= $03^h36^m46.^s177$, δ= -35°59′54.″70 (the yellow circle in Figure 4.6). (3) The extended emission: an elliptical region (ellipse radii:3″ and 6″, angle = 5°), centered at the core source (the green ellipse in Figure 4.6.) but excluding the core (the blue circle) and the northern blob (the yellow circle).

All spectra were analyzed with XSPEC 11.3 and CIAO 3.0 software . Using the FTOOL “grppha” the data were grouped into bins with at least 15 or 20 counts for χ^2 fitting. The data were fitted with the X-ray spectral analysis tool XSPEC. Errors correspond to the 90% confidence level for the one interesting parameter ($\Delta\chi^2$=2.71), keeping the other model parameters fixed. A large annular source-free region centered on the core source is used for the background. Only the data within the energy range between 0.35 and 2.0 keV are used in the the spectral fitting for the northern blob and

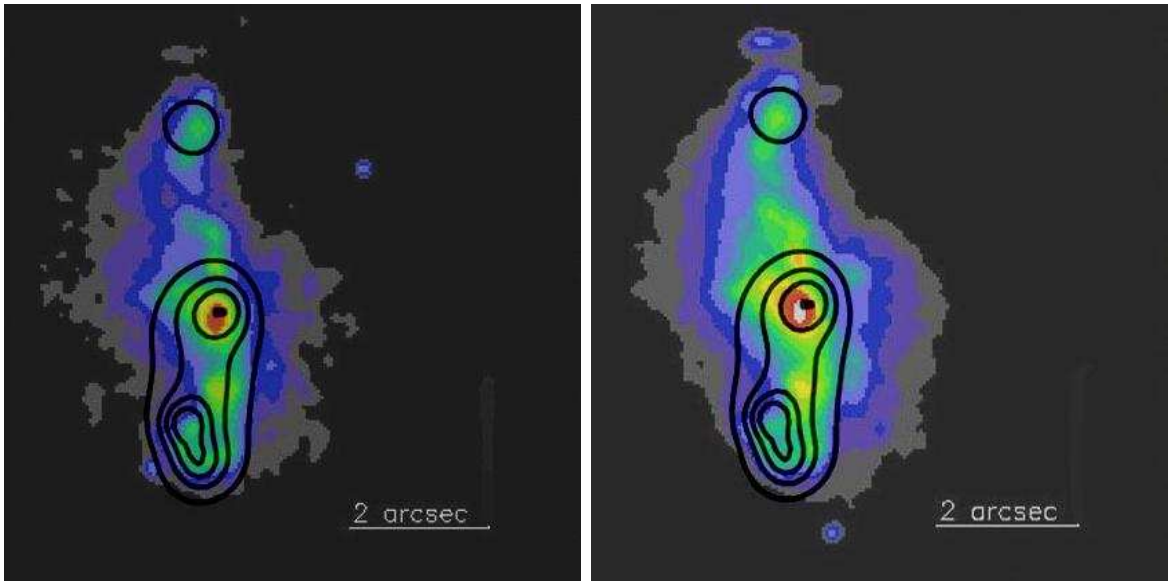

Figure 4.3: The *Chandra* X-ray (0.1-0.5 keV) contours overlaid on the *HST* (WFPC-2) images of NGC 1386. *Left*: X-ray contours overlaid on the [O III] image. *Right*: X-ray contours overlaid on the [N II]$\lambda\lambda$6548,6583 + Hα image. Contour levels are drawn at 0.03, 0.065, 0.104, 0.15 10^{-3} counts s^{-1} $arcsec^{-2}$.

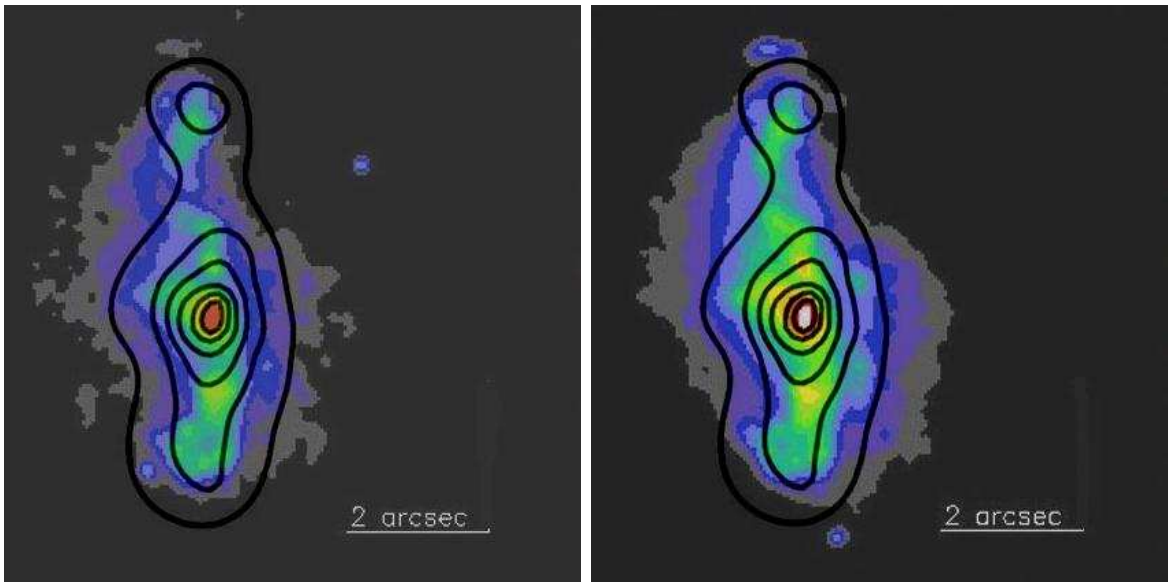

Figure 4.4: The *Chandra* X-ray (0.5-1.0 keV) contours overlaid on the *HST* (WFPC-2) images of NGC 1386. *Left*: X-ray contours overlaid on the [O III] image. *Right*: X-ray contours overlaid on the [N II]$\lambda\lambda$6548,6583 + Hα image. Contour levels are drawn at 0.03, 0.121, 0.272, 0.484, 0.756, 1.088 10^{-3} counts s^{-1} $arcsec^{-2}$.

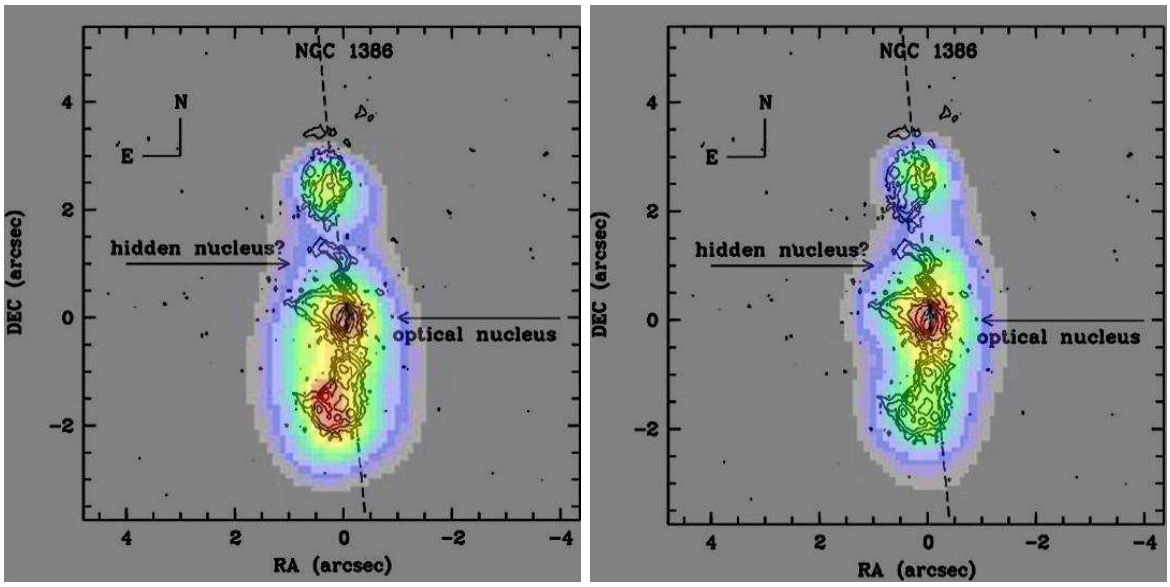

Figure 4.5: The *HST* [O III] contours (provided by Henrique Schmitt) overlaid on the *Chandra* soft X-ray images of NGC 1386. The contours start at the 3σ level above the background (2.1×10^{-14} erg cm^{-2} s^{-1} arcsec^{-2}) and increase in powers of 2 times $3\sigma(3\sigma \times 2^n)$. A hidden nucleus is located $\sim 1''$ north of the optical nucleus (Bennert et al. 2006). *Left*: X-ray (0.1-0.5 keV) contours overlaid on the [O III] image. *Right*: X-ray (0.5-1.0 keV) contours overlaid on the [O III] image.

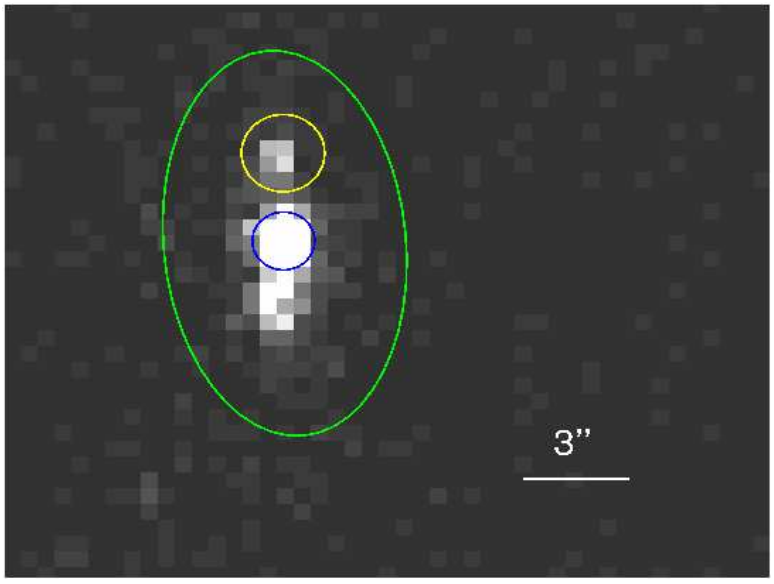

Figure 4.6: Individual regions of NGC 1386 marked on the *Chandra* raw image (see text). The white bar represents $3''$.

the extended region. The main reasons are as follows: (1) The lower bound of 0.35 keV was chosen to avoid a strong feature in the instrumental background; (2) Given that the 2.0-8.0 keV ACIS-S3 count rates for these two regions are basically zero, excluding the spectral data above 2.0 keV is appropriate in order to maintain an adequate S/N for the spectral fitting.

4.4.1 The northern blob

Since the location of the soft X-ray northern blob is coincident with the position of the [O III] northern blob where some signs for shocks are founded by Bennert et al. (2006), it is plausible that the soft X-ray emission from this blob is also produced by shocks.

To check the shock scenario, I fit the 0.35-2.0 keV spectrum of the northern blob with collisionally ionized plasma model (the MEKAL model in XSPEC). In the model fitting, the column density is fixed to the Galactic Density $N_{\rm H,Gal}$= 1.4 $\times$ 10^{20} cm^{-2}. Variation of the metal abundances does not improve the fit, while providing poor constraints on metal abundances. Consequently, we fix the metal abundances to the solar values in the spectral analysis. The best-fit temperature is kT = $0.26^{+0.07}_{-0.04}$ keV (χ^2_{red} = 0.26, see the upper panel of Figure 4.7).

Alernatively, the spectrum can be fitted with the plane-parallel shock plasma model, the NPSHOCK model in XSPEC (Borkowski et al. 2001). The model parameters are the post shock temperature (T$_s$), the postshock electron temperature (T$_e$), the lower and upper limits on the ionization timescale (τ_l and τ_u); and the metal abundance Z is fixed to the solar value. Perhaps because the quality of the data is not high enough, the temperatures can not be well constrained (T$_s$=1^{+4}_{-1} keV, T$_e$=1^{+32}_{-1} keV, with χ^2_{red} = 0.16; see the lower panel of Figure 4.7).

4.4.2 The extended emission

Bennert et al. (2006) determined the radius of Narrow Line Region (NLR) in NGC 1386 to be 6″, excluding the [O III] contamination from circumnuclear starbursts. The imaging analysis of the *Chandra* ACIS images of NGC 1386 in Section 4.3 has shown that there is a spatial coincidence between the soft X-ray emission and the optical-line emission within a radius of 4″. Thus, the soft X-ray extended emission is correlated with the optical NLR in NGC 1386. In this section, I mainly consider a few models for the spectrum of the extended emission *excluding* the northern blob.

Power-law model

We start with a simple power-law model, corrected for photoelectric absorption, with the absorbing column assumed to be equal to the Galactic line-of-sight column density, $N_{\rm H,Gal}$= 1.4 $\times$ 10^{20} cm^{-2} or the average column 2 $\times$ 10^{21} cm^{-2} derived from optical data (Bennert et al. 06). If the photon index is fixed to 1.9, it is obvious that this model does not give an acceptable fit with either the Galactic column density (χ^2_{red}=2.8) or the average column density (χ^2_{red}=1.6). Next, I attempted to fit the data with a model including a free photon index and the absorbing column fixed to the Galactic value, i.e. intending to determine the degree of curvature in the spectrum. The best-fit parameter

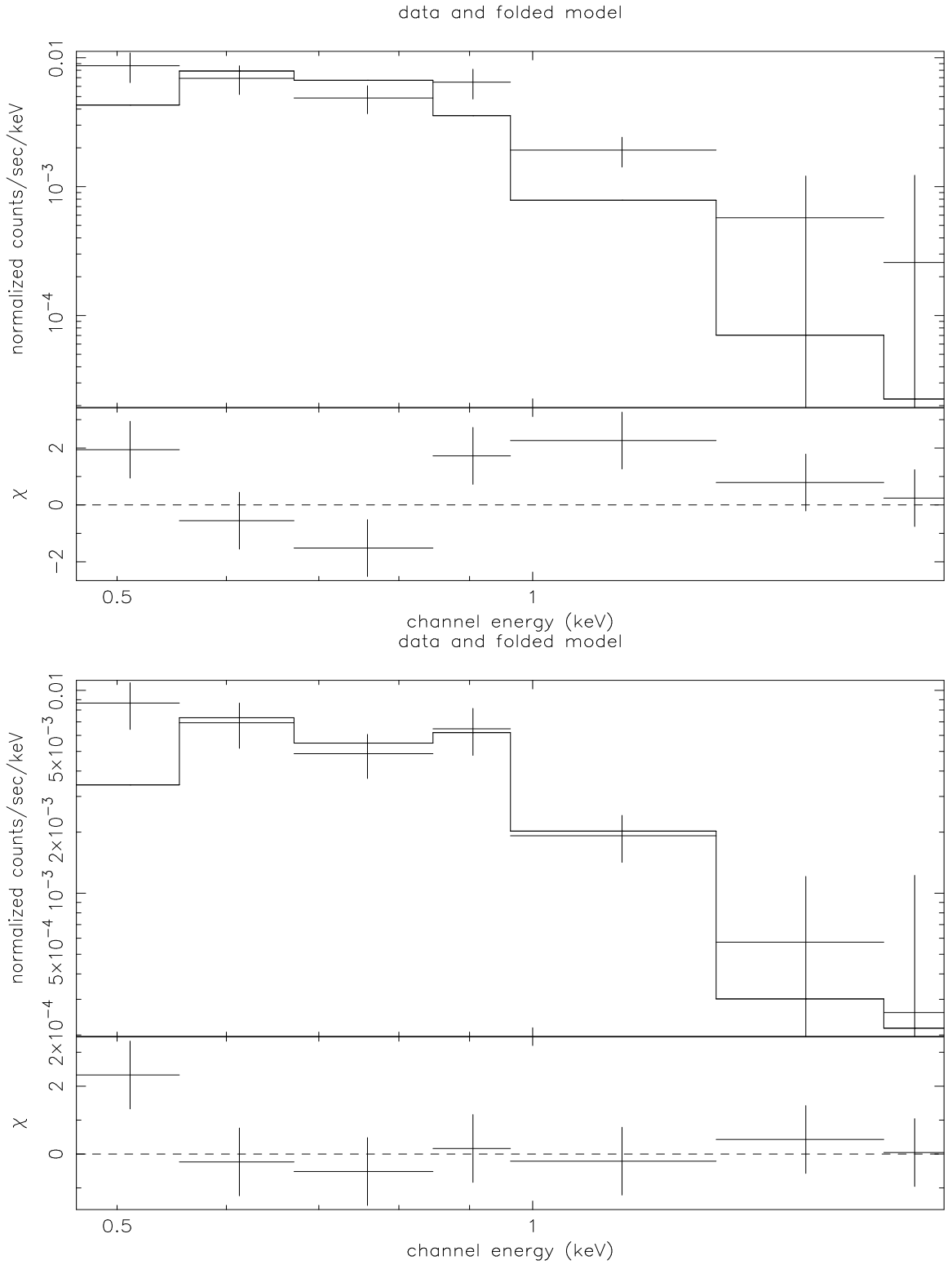

Figure 4.7: *Chandra* ACIS X-ray spectra of the northern blob in NGC 1386. The fitted model is a thermal MEKAL model (the upper panel) or a NPSHOCK (the lower panel).

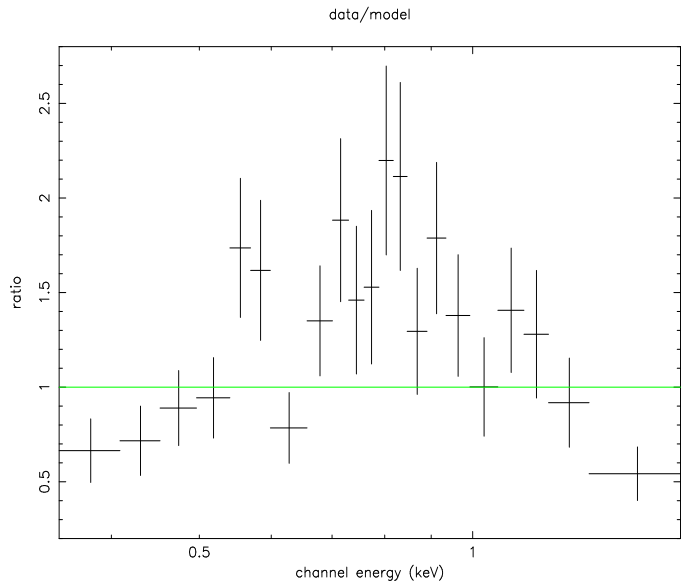

Figure 4.8: The data of the extended emission divided by a power-law model with a free photon index and the Galactic column. This figure illustrates the positive residuals in the 0.5-1.5 keV band can be seen in the spectrum even for a steep power-law continuum.

is $\Gamma \sim 3.1 \pm 0.1$ in this case, giving $\chi^2_{red} = 2.8$ for 15 degrees of freedom. However, I found there are still some positive residuals around 1 keV for such a steep power-law model (see Figure 4.8). Considering the low S/N of the data and the small number of total counts in the spectrum, as well as the fact that the residuals peak at $\sim$ keV might be judicative of a more complex emission as seen in other galaxies, I explore more additional models below.

XSTAR photoionization model

Given the existence of positive residuals in a single continuum, I consider the possibility that the soft X-ray spectrum contains emission lines clusters which are heavily blended together, and very difficult to resolve at the low resolution of the CCD. When the spectra are "smoothed" by the finite resolution, these blended lines mimic a pseudo-continuum, leading to the poor constraints of the spectrum shape due to the low S/N. To check if the soft emission is rich in emission lines, I used the unbinned data fitted by a power-law model with a free index. Some of emission lines (either present or absent in the spectrum) in the energy range of 0.5-1.5 keV(8-24 $\mathring{A}$) are marked in unbinned spectrum in Figure 4.9. The strong emission line features might include Mg XI 1.34 keV(9.32$\mathring{A}$), Fe XXIV 1.18 keV(10.5$\mathring{A}$), Fe XXIII 1.08 keV(11.5$\mathring{A}$), Ne IX 0.915 keV (13.5$\mathring{A}$), Fe XIX 0.83 keV(15 $\mathring{A}$), Fe XVIII 0.77keV(16.1$\mathring{A}$), O VII 0.738keV(16.8$\mathring{A}$), O VII (17.4-17.8$\mathring{A}$), and O VII 0.56keV(22.1$\mathring{A}$).

In AGN unification models, the emission lines can arise from a photoionized medium, which may contribute to the extended emission. We used XSTAR model produced by the XSTAR photoionization code (Kallman & Krolik 1993, here version 2.1kn3) in this section to test this hypothesis. The XSTAR computer code is a program to calcu-

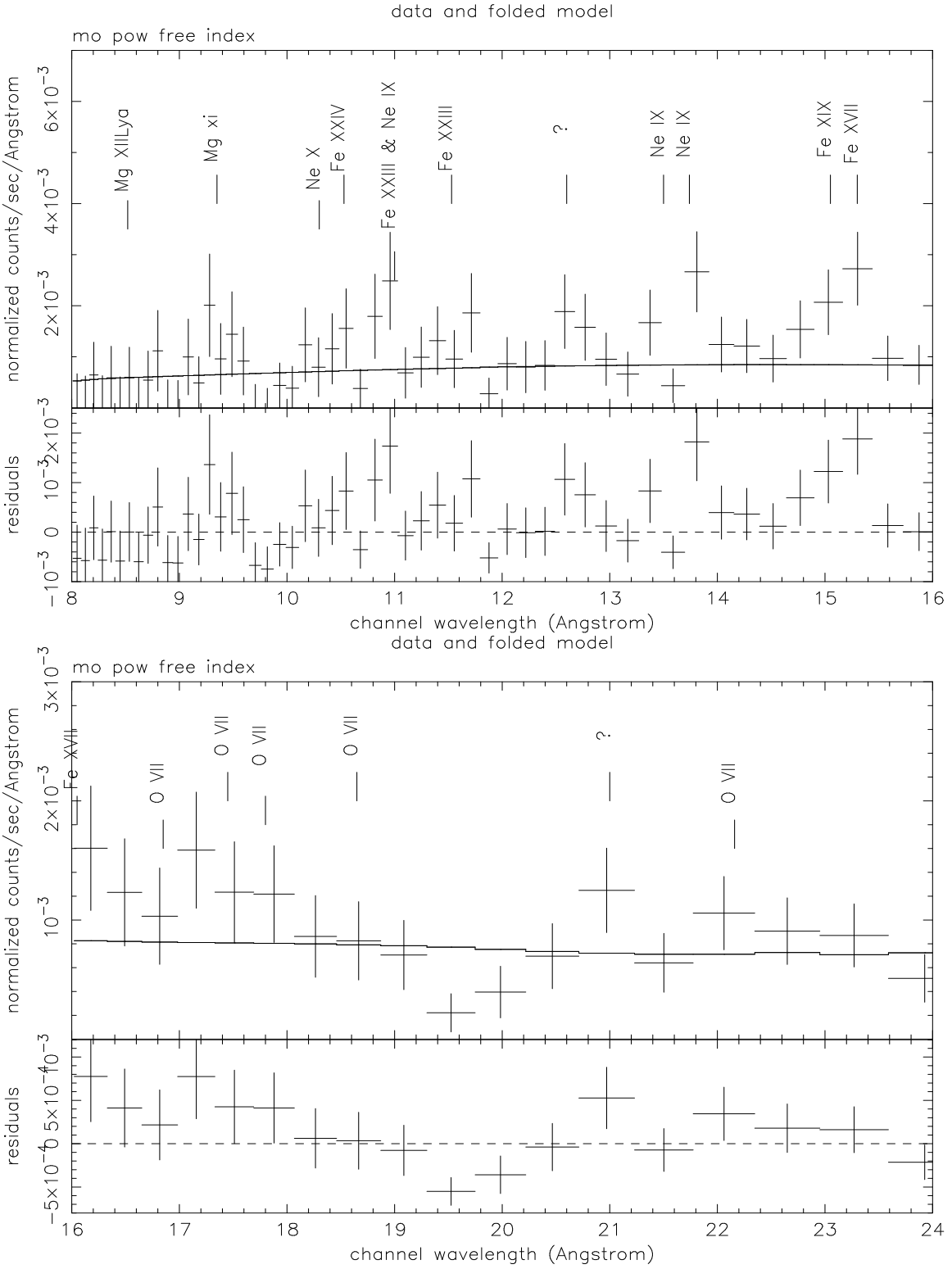

Figure 4.9: The unbinned spectrum of the extended emission modelled by a power-law with a free index. Locations of known emission lines (either present or absent in the spectrum) are marked.

late the physical conditions and emission spectra of spherically extended photoionized gases with a point source of continuum radiation at the center. The presence of the spherically extended gases affects the observed spectrum, which absorbs some of the radiation and reradiate it in other portions of the spectrum. XSTAR calculates the effects on the gas of absorbing this energy and the spectrum of reradiated emission. XSTAR includes a useful command XSTAR2XSPEC, which allow us to use XSTAR with the actual data. XSTAR2XSPEC calls XSTAR multiple times and produces table models from the results of the calculations and then which can be used in XSPEC fitting procedures to obtain a best-fit model.

The input parameters of the code are the central continuum, the density and the column density, the X-ray ionization parameter, the temperature and the eletment abundances. The ionization parameter is defined as $\xi = L/(nR^2)$ erg cm s^{-1}, where L is the luminosity in the 0.0136-13.6 keV band[1], fixed to 10^{43} erg s^{-1}; n is the density and R is the distance from the ionizing source. The density is assumed to be 1000 cm $^{-3}$, and the temperature is taken to be 10^5 K. If I assume the central continuum is a power-law with the photon index $\Gamma = 2$ ($F \propto E^{-\Gamma}$ in XSPEC), then the energy slope α is set to be -1, since the luminosity L in XSTAR is related with the energy E as $L \propto E^{\alpha}$ and $\Gamma = -(\alpha - 1)$ by definition.

The two most important parameters in the XSTAR calculations, the ionization parameter and the column density, determine the level of ionization and affect the line intensities and line ratios. I assume that log ξ ranges from 0 to 4 and the column density varies from 10^{20} to 10^{23} cm $^{-2}$. Theoretical calculations of a photoionized medium with the XSTAR code demonstrate that soft X-ray emission lines can be produced in photoionized gas. To illustrate it, we show a XSTAR model in Figure 4.10 with a covering factor of 1, temperature set to 10^5 K, density n=1000 cm $^{-3}$, a column density of 10^{21} cm $^{-2}$, and logξ=2.5.

However, the XSTAR photoionization model does not provide a good description of the spectrum. If the column density is fixed to $N_{\rm H,Gal}$, χ^2_{red} is 5.7. Allowing the column density to vary does not substantially improve the fit. The curvature predicted by the model does not match the observed spectral shape: positive residuals can clearly be seen in Figure 4.11. There are three "humps": the first "hump" is below 0.5 keV, the second one between 0.7 and 0.9 keV, and the third one between 1.0 and 1.2 keV. In the energy ranges where the latter two "humps" exist, there are mostly the blends of Fe L and Ne K lines. It is possible that the discrepancies are due to some strong emission lines which stand out against the continuum in the observed spectrum. I searched for ways to eliminate the discrepancies by adjusting the parameters of the XSTAR photoionization models. I found the strength of Fe L lines (e.g. Fe XXIII 1.08 keV and Fe XXIV 1.18 keV) can be increased with varying the ionization parameter and the column density at solar abundance, but, unfortunately, it can also affect the strength of the emission lines of other elements. More specifically, at high ionization parameters, the lines of other elements, such as Ne and Mg, are shown to dominate iron over the 0.7-1.5 keV range, that is, the iron L lines around 1.1 keV are always weaker than those of other element lines e.g. around 0.9-1.0 keV band. I also considered the possibility of

[1]I extrapolate $L_{0.0136-13.6keV}$ from the estimated $L_{2-10keV}$, by using a power-law model with $\Gamma = 2$. An estimate of $L_{2-10keV}$ was derived in Section 4.5.2.

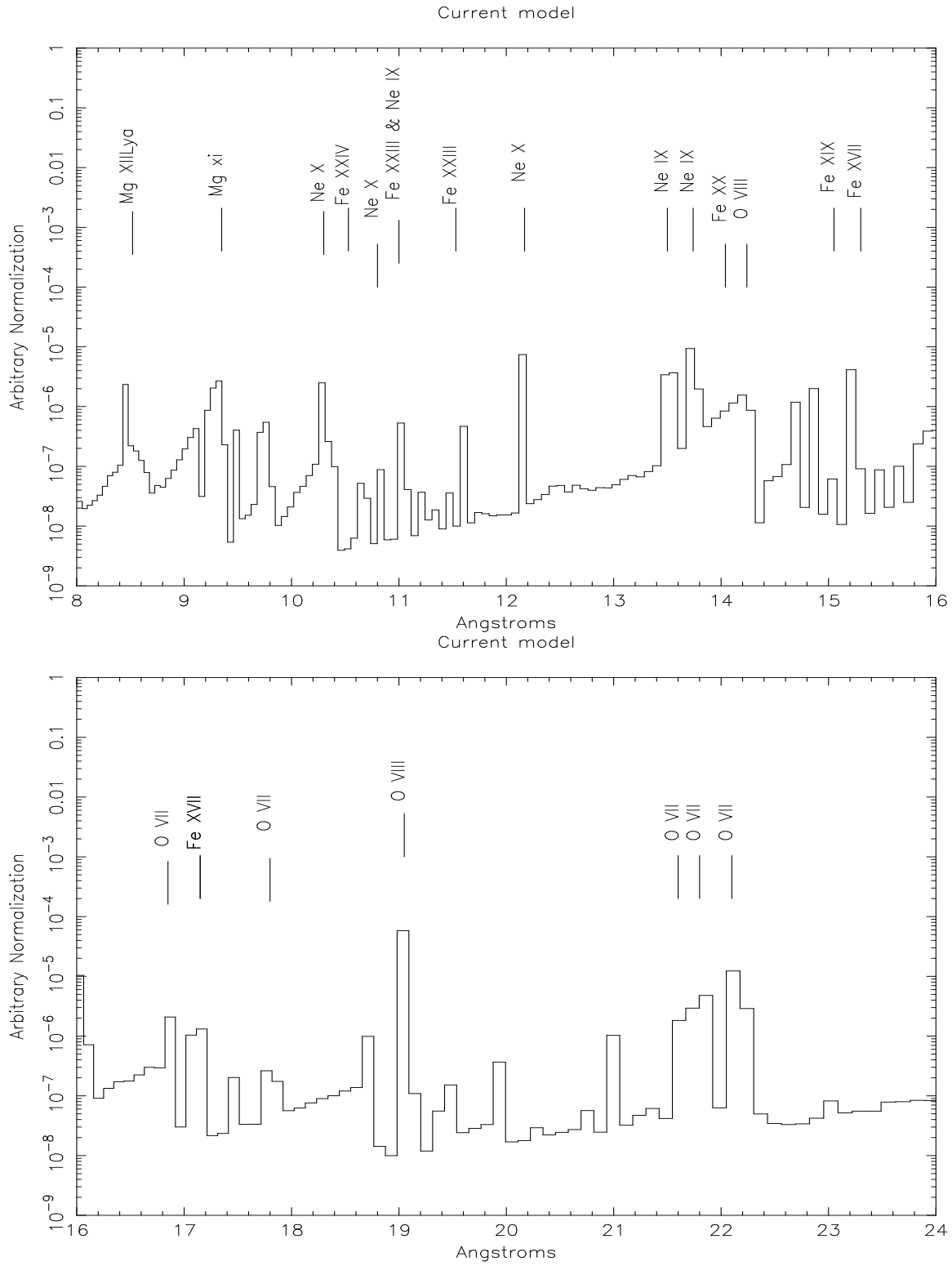

Figure 4.10: An example of an emission spectrum of in the forward (transmitted) direction produced by XSTAR. Representative emission lines are marked in the spectrum.

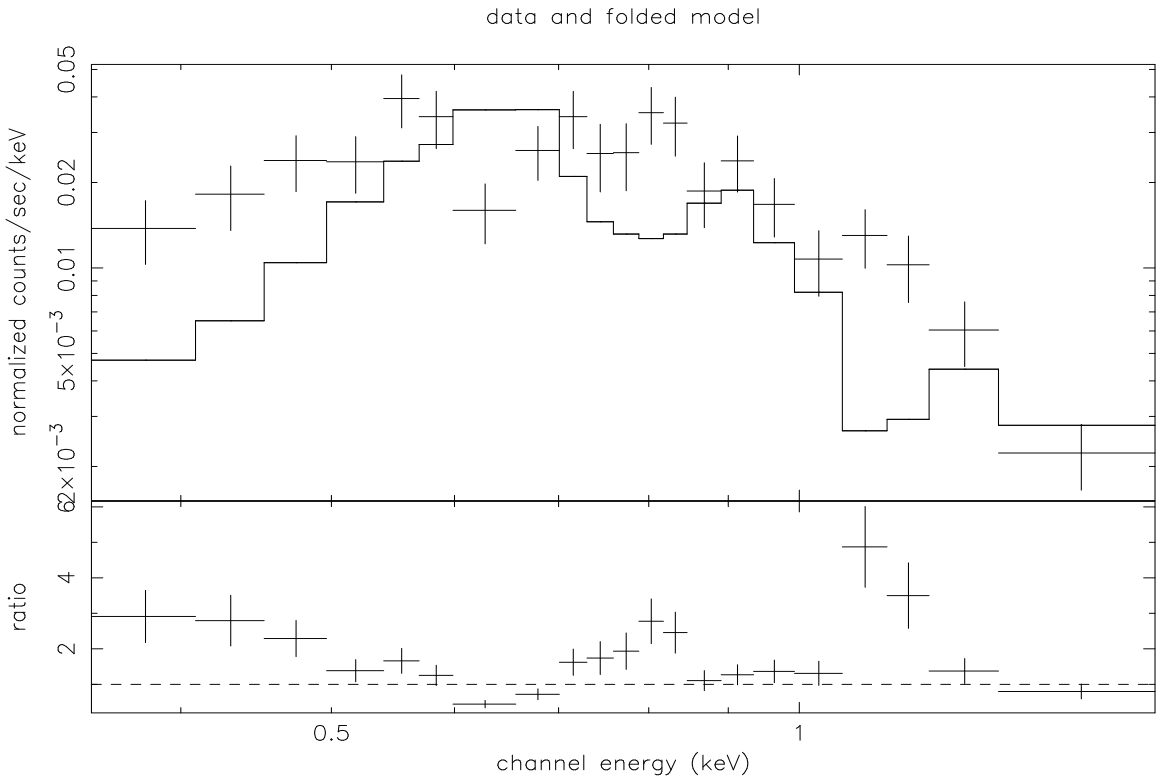

Figure 4.11: The *Chandra* ACIS X-ray spectrum of the extended emission *excluding* the northern blob of NGC 1386 fitted by the XSTAR photoionization model. The column density is fixed to $N_{\rm H,Gal}$= 1.4×10^{20} cm^{-2}. Positive residuals are clearly seen in the lower panel, indicating that the XSTAR models is not a good representation of the spectral data.

the abnormally high of Fe/H ratio, but experimenting with iron abundance that is four times solar results in changes that are still not high enough to make the iron L emission dominant. It seems that the apparent discrepancies can not be resolved by adjusting the parameters of the models. Though XSTAR photoionization model predicts many emission lines in the soft X-ray band, it can not represent the observed spectrum of the extended emission. This is discussed further in Section 4.5.

Black-body model

By inspecting of the observed spectral shape, I found the soft X-ray spectrum rises steeply (compared to an extrapolation of the power-law fits to lower energies) and the spectrum, grouped to a minimum of 15 counts bin^{-1}, appears to be continuous with a significant curvature. Therefore, I attempted to fit the data with a curved black-body model. The column density is fixed at either the Galactic absorption or the average absorbtion. According to the optical measurement of A_V (Bennert et al. 2006), and the relation between $N_{\rm H}$ and A_V (Bohlin et al. 1978), the average column density can be roughly estimated at $N_{\rm H} = 2 \times 10^{21}$ cm^{-2} which is adopted in the spectral analysis. The black-body component is consistent with the shape of the soft X-ray spectrum and can be considered a crude parameterization of the spectrum. The possibility of

Table 4.1: Spectral fits to X-ray spectra of the extended region of NGC 1386. The models are shown: (1) the black-body model and (2) the bremsstrahlung model. [a] $N_{\rm H,Gal}$= 1.4 × 10^{20} cm^{-2}. [b] the average absorption 2.0 × 10^{21} cm^{-2} (according to Bennert et al.2006).

Model	$N_{\rm H}$	$k\mathbf{T}$	$L_{0.35-2.0keV}$	χ^2_{red}
	10^{20} cm^{-2}	keV	erg s^{-1}	(d.o.f)
(1)	1.4[a]	$0.16^{+0.02}_{-0.01}$	1.28×10^{39}	1.0(19)
	20.0[b]	$0.13^{+0.01}_{-0.02}$	3.51×10^{39}	1.8(19)
(2)	1.4[a]	$0.45^{+0.07}_{-0.05}$	1.38×10^{39}	1.6(19)
	20.0[b]	$0.24^{+0.01}_{-0.01}$	5.02×10^{39}	1.0(14)

the heavy line blending at the spectral resolution of the CCD has to be ignored in this model. The best-fit black-body temperature is around 110-160 eV(see Table 4.1 and Figure 4.12). The addition of a second black-body component with a different temperature does not give a significant improvement of the fit.

Bremsstrahlung model

An alternative model in terms of thermal bremsstrahlung for the soft X-ray continuum is also considered. From spectral fitting I found that the thermal bremsstrahlung model is also an acceptable description for the extended emission (see Figure 4.13). The best-fit bremsstrahlung temperatures are shown in Table 4.1. I will discuss the possible implication of this model in Section 4.5.

4.4.3 The nuclear emission

Fe Kα emission

One of the striking features from the nuclear emission of NGC 1386 is the Fe Kα emission line in the hard X-rays band. An excess of the counts is evident in the 6.3-6.5 keV band (see Figure 4.14). This indicates the presence of the strong iron K-shell emission line in the object. When the data were grouped to a minimum of 20 counts bin^{-1} in the core region, the spectral resolution above 1 keV was significantly reduced by the grouping. Due to the small number of the counts, I use the "local fits" (see Guainazzi et al. 2005) in the 5.25 - 7.25keV energy range with the unbinned spectra. Since χ^2 fitting is not meaningful with the unbinned spectrum the C-statistic (Cash 1979) was used to determine the best fits and errors for the Fe Kα emission from the nuclear region, and the "Goodness" command in XSPEC was run to determine the

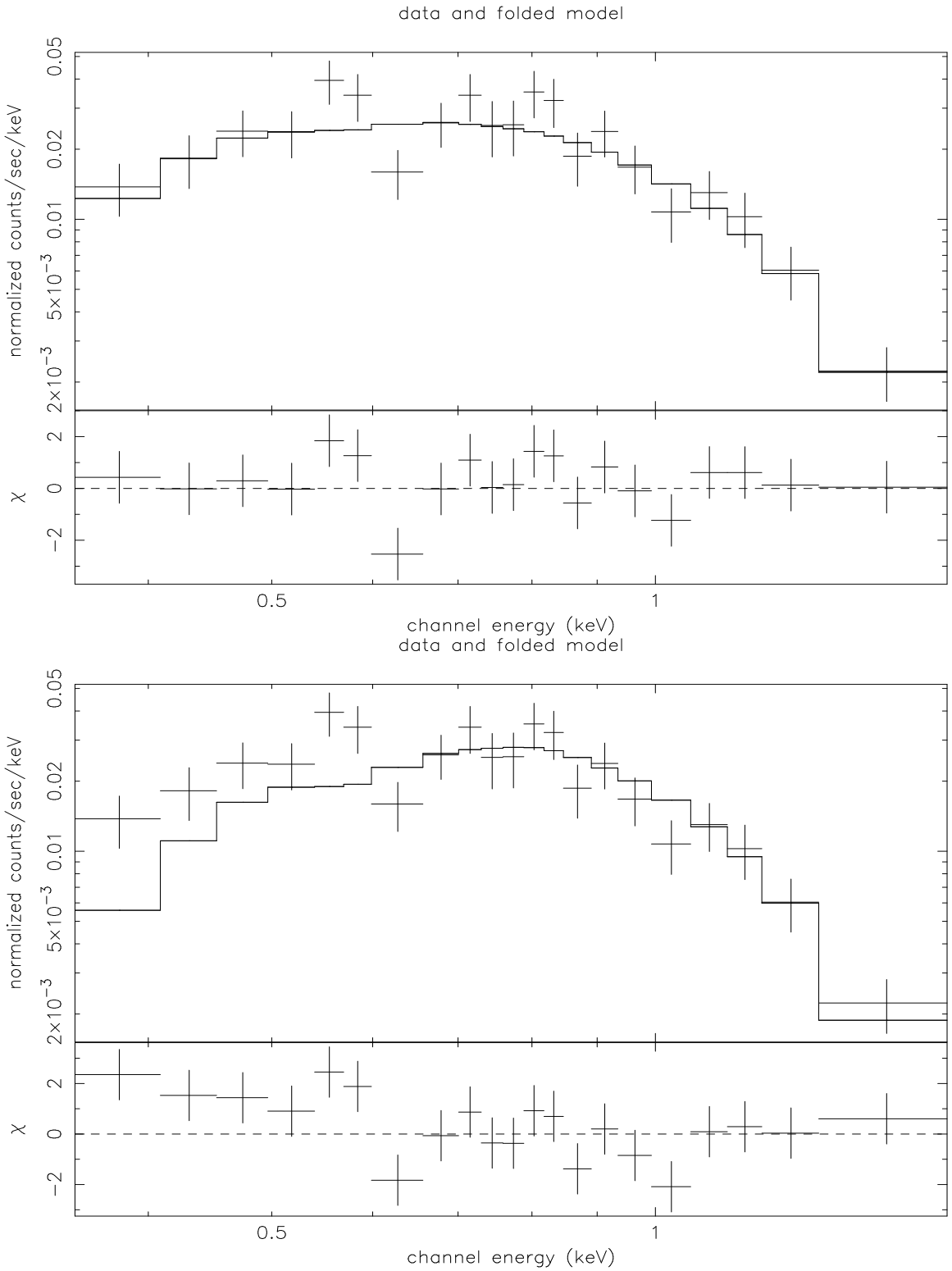

Figure 4.12: The spectrum of the extended emission fitted by a blackbody model with Galactic absorption (upper panel) and the average absorption derived rom the the optical data by Bennert et al. (lower panel).

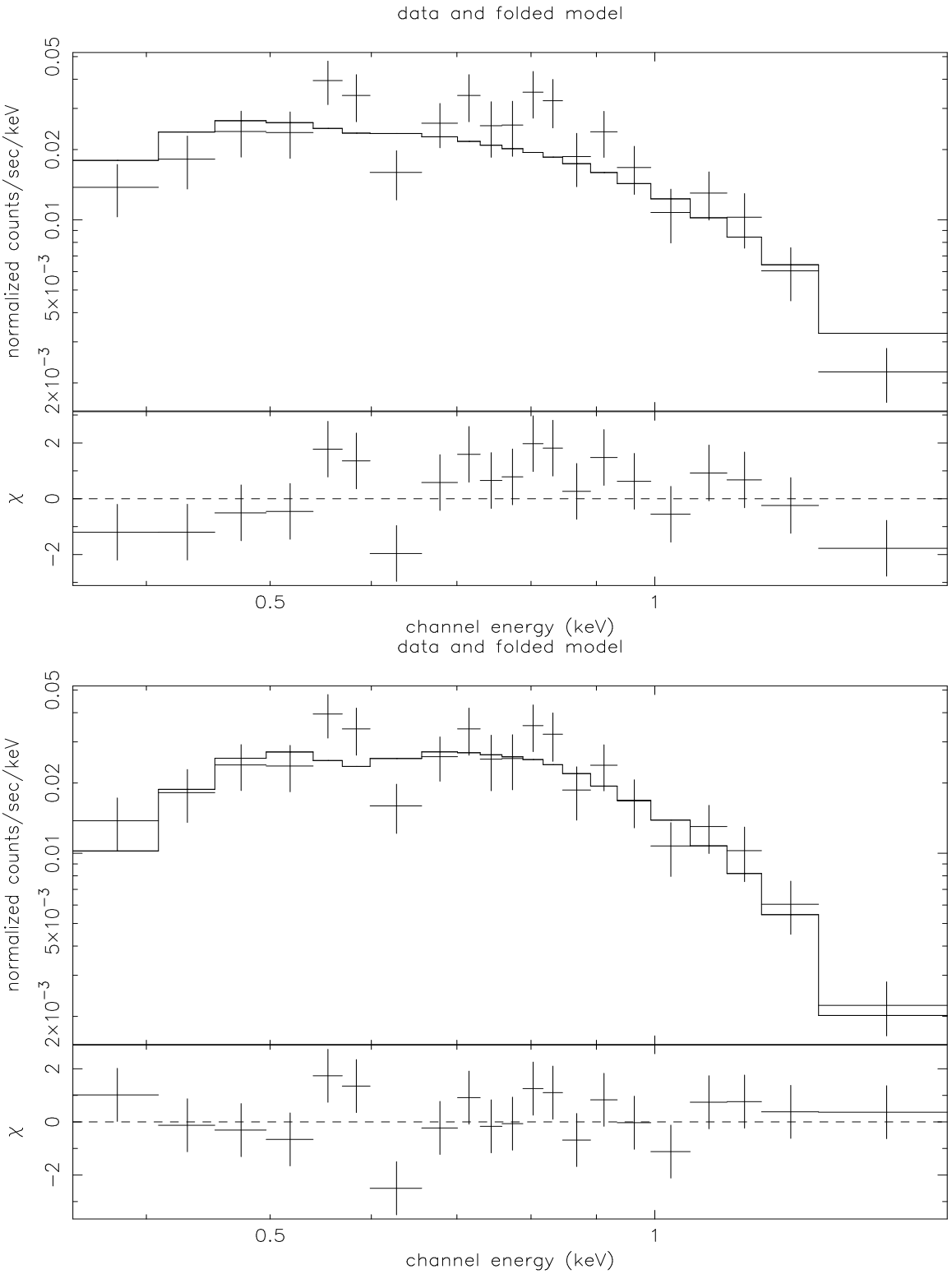

Figure 4.13: The spectrum of the extended emission fitted by a thermal bremsstrahlung model with Galactic absorption (upper panel) and an average absorption derived from the optical data by Bennert et al. (lower panel).

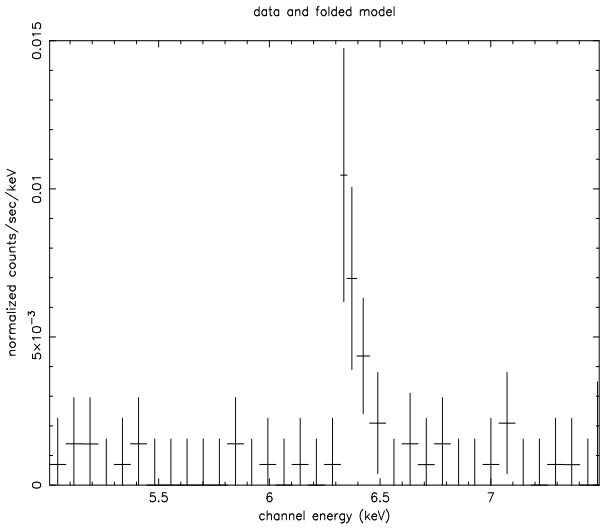

Figure 4.14: The "local" fit for the iron line of NGC 1386.

goodness of the fit. I found if the line width is set to be 0.01 keV, the measured energy of the emission line is $6.39^{+0.05}_{-0.07}$ keV, which is consistent with the energy of Fe Kα at the systematic velocity of the galaxy. The equivalent width for the narrow line is $1.39^{+1.13}_{-0.54}$ keV, with 39% of Monte-Carlo probability. The contours plotted in Figure 4.15 are for the 68.3%, 90%, and 99% confidence limits on the values of the energy of Fe Kα line emission and the normalization.

The overall spectrum

In this section, I discuss the 0.35-8.0 keV data from the nuclear emission region. Channels below 0.35 keV and above 8 keV were ignored in the spectral fitting, and the data were grouped into a minimum of 15 counts bin^{-1}. The spectrum was initially fitted with a model consisting of an Fe Kα emission line and a power-law continuum (Γ = 1.9) suffering a photoelectrical absorption by the Galactic column density $N_{\rm H,Gal}$= 1.4 $\times$ 10^{20} cm^{-2}. This gives an unacceptable fit, with the significant positive residuals below 2 keV. This is an indication that the soft excess below 2 keV arises from the the nuclear emission in NGC 1386. The spectral shape of this soft X-ray excess is shown in Figure 4.16. In the following analysis, I consider an additional component to represent the soft X-ray emission from the nucleus.

Double power-law model

In a first attempt, I fit the data with a model composed of two power-law components and a Gaussian line at 6.4 keV. One power-law model has a fixed photon index Γ_1 = 1.9, and the other has an unconstrained photon index Γ_2. Both of power-law have been modified by the Galactic column density $N_{\rm H,Gal}$or the average value derived from optical observations (Bennert et al. 2006). The spectral results are listed in Table 4.2. Even though the addition of a second power-law significantly improves the single

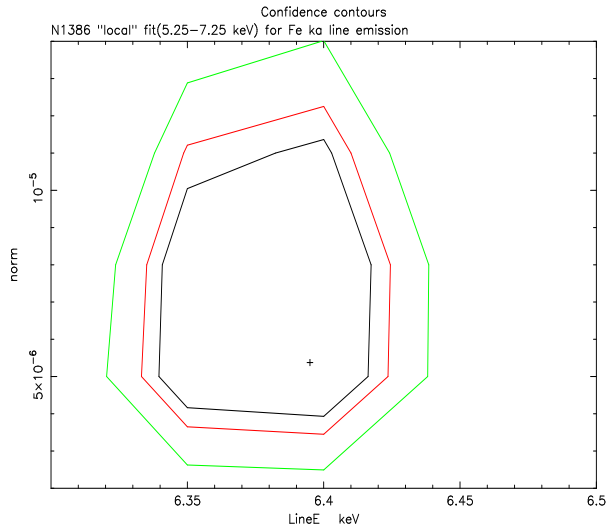

Figure 4.15: C-statistic contour plots in the Normalization-Energy space for Fe Kα emission line in NGC 1386. The solid lines indicate the 68%, 90%, and 99% confidence contours for the best-fit model of the local fits.

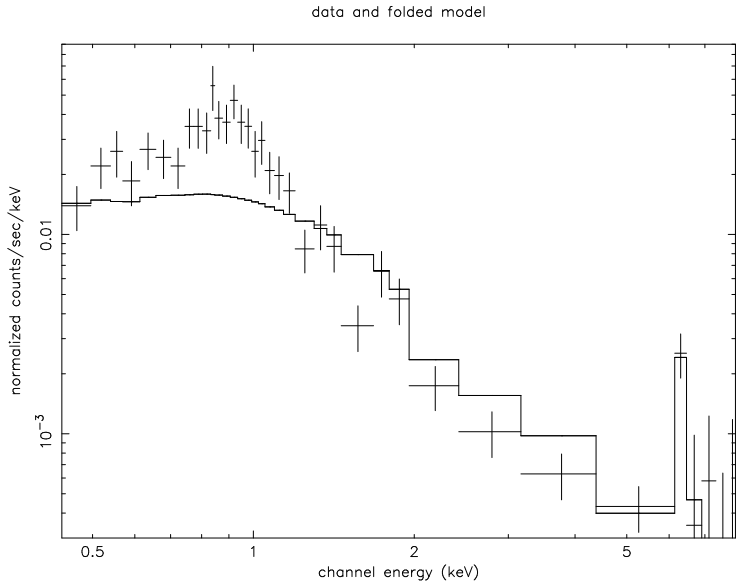

Figure 4.16: Illustration of the soft X-ray excess from the nuclear emission of NGC 1386. The solid line represents the model consisting of an Fe Kα emission line and a power-law continuum ($\Gamma = 1.9$) with $N_{\rm H,Gal}$= 1.4 $\times$ 10^{20} cm^{-2}.

Table 4.2: X-ray continuum models for the nuclear emission in NGC 1386. Three continuum models are shown: (1) two power laws, (2) a black-body plus a power law, and (3) a bremsstrahlung plus a power law. The column density is fixed to either the Galactic column density $N_{\rm H,Gal}$, or the average value from optical observations. In Model (1), two photon indices (Γ_1 and Γ_2) are shown separately. [a] Galactic column density $N_{\rm H,Gal}$= 1.4 × 10^{20} cm^{-2}. [b] the estimated, average column density 2.0 × 10^{21} cm^{-2}, according to Bennert et al. (2006).

Continuum Model	$N_{\rm H}$ 10^{20} cm^{-2}	$k\mathbf{T}$ (eV)	Γ_1	Γ_2	$L_{0.35-8.0keV}$ erg s^{-1}	χ^2_{red} (d.o.f.)
(1)	1.4[a]	–	1.9	$2.84^{+0.25}_{-0.63}$	3.28×10^{39}	0.8 (132)
	20.0[b]	–	1.9	$4.01^{+0.23}_{-0.20}$	6.70×10^{39}	0.6 (132)
(2)	1.4[a]	$0.19^{+0.02}_{-0.02}$	1.9	–	3.14×10^{39}	0.5 (132)
	20.0[b]	$0.14^{+0.01}_{-0.02}$	1.9	–	5.85×10^{39}	0.4 (132)
(3)	1.4[a]	$0.56^{+0.16}_{-0.12}$	1.9	–	3.21×10^{39}	0.7 (132)
	20.0[b]	$0.29^{+0.04}_{-0.03}$	1.9	–	6.72×10^{39}	0.5 (132)

power-law, strong residuals can be seen in the low-energy band. The residuals in the 0.8-1.2 keV range exhibit a "hump" clearly seen in Figure 4.17.

Power-law plus black-body model

An alternative model for the soft excess is a black-body component, which is thermal in nature. If the soft excess is from an accretion disk about the central black hole, it can be approximated by a black-body model. Then the overall emission from the core can be fitted by the combined model (a power-law plus a black-body Model with a Gaussian feature; see Figure 4.18). Since the column density can not be well constrained, it is again fixed to either the Galactic column density $N_{\rm H,Gal}$, or the average column density estimated from the optical observations (see Table 4.2). A by-eye inspection of the spectrum does indicate that the power-law plus black-body model is a better attempt to minimize the residuals in the soft X-ray band. Statistically, however, both models provide acceptable fits.

Power-law plus bremsstrahlung model

We also attempted a model fit, replacing the black-body model with the bremsstrahlung model. The combined model for the core emission consists of a power-law plus a bremsstrahlung model with a Gaussian line at 6.4 keV. The results are listed in Table 4.2 and the spectrum is shown in Figure 4.19.

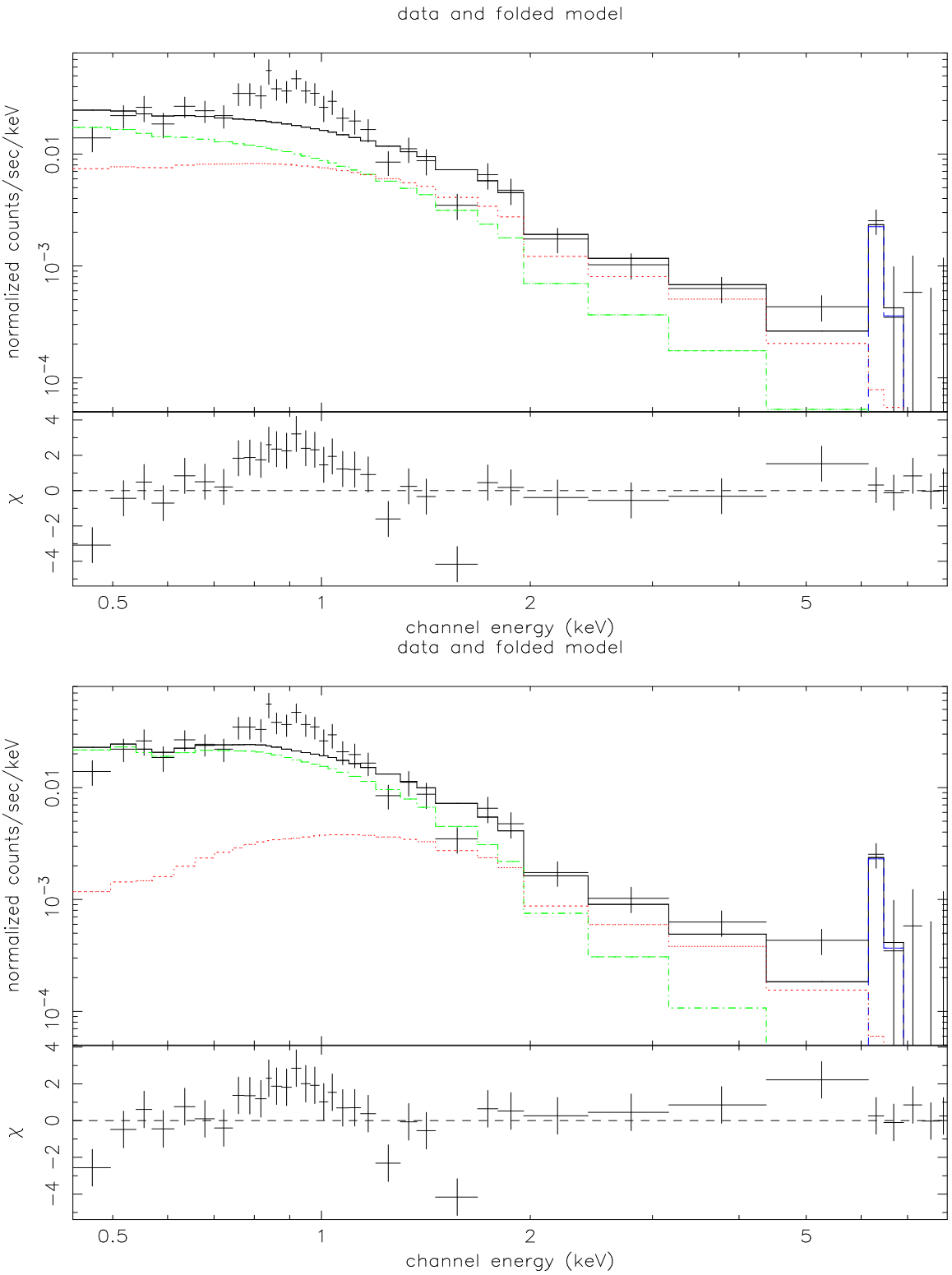

Figure 4.17: The double power-law models (red and green) with a Gaussian line (blue) fit to the overall *Chandra* ACIS X-ray spectrum (0.35-8.0keV) of the nucleus of NGC 1386. The column density is fixed to the Galactic absorption $N_{\mathrm{H,Gal}}$(upper panel) and the average column density estimated from the optical observations (lower panel). A "hump" is clearly seen in the residuals at low energy.

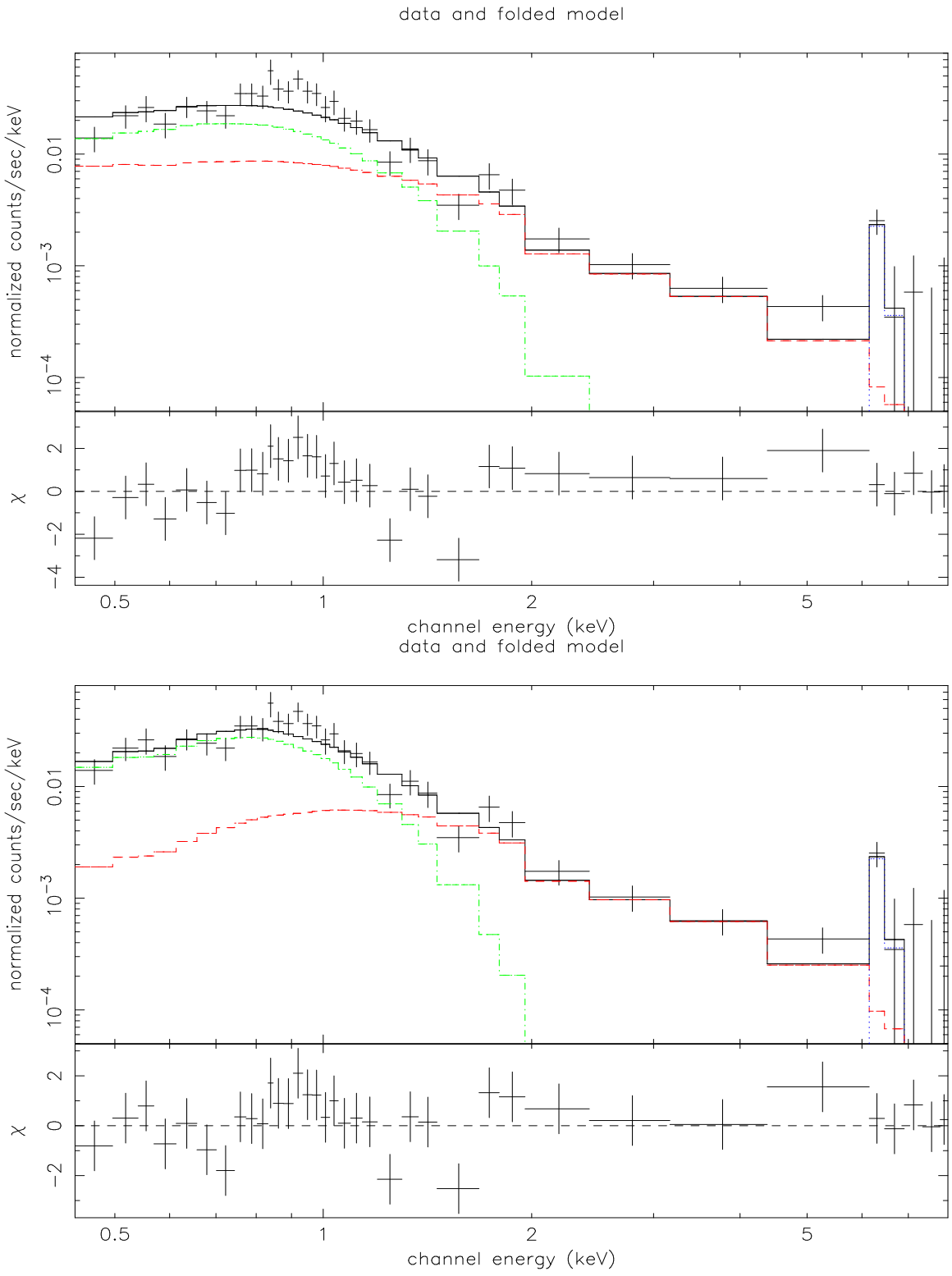

Figure 4.18: The power-law (red) plus black-body (green) model with a Gaussian line (blue) fit for the overall *Chandra* ACIS X-ray spectrum (0.35-8.0keV) from the nucleus of NGC 1386. The column density is fixed to the Galactic absorption $N_{\rm H,Gal}$(upper panel) and the average column density estimated from the optical observations (lower panel).

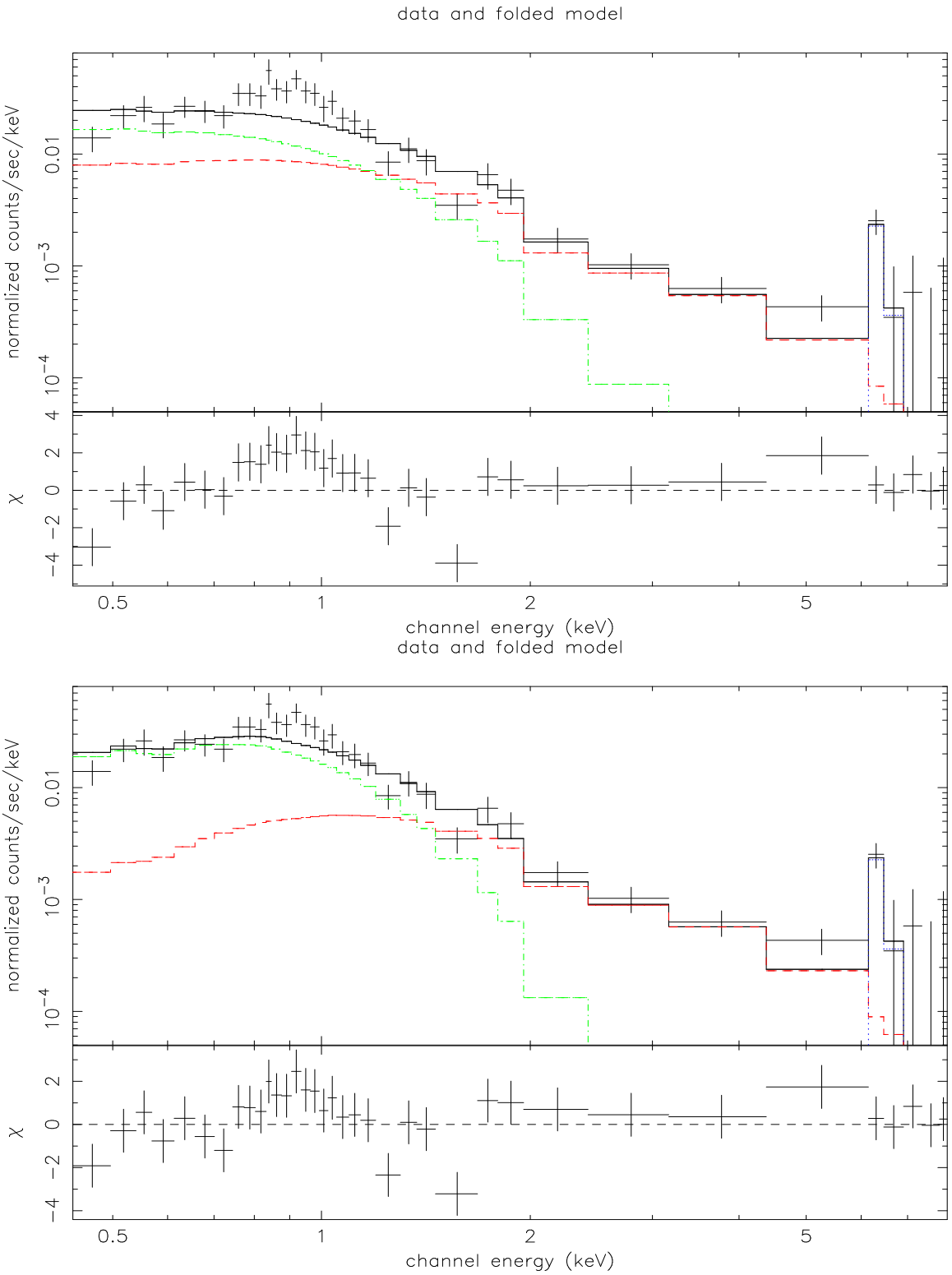

Figure 4.19: The power-law (red) plus bremsstrahlung (green) model with a Gaussian line (blue) fit for the overall *Chandra* ACIS X-ray spectrum (0.35-8.0keV) from the nucleus of NGC 1386. The column density is fixed to the Galactic absorption value of $N_{\rm H,Gal}$(upper panel) or the average column density estimated from the optical observations (lower panel).

4.5 Discussion

4.5.1 The Implications of the observed Fe Kα emission

The existence of "cold" fluorescent Fe Kα emission from the obscuring torus is predicted by the AGN unification models. The line equivalent width can be a good indicator of the absorbing column density (e.g. Ghisellini et al. 1994). Ghisellini et al. (1994) calculate the equivalent widths of fluorescence iron line produced by the torus as a function of $N_{\rm H}$. They assume a power-law continuum emission with a photon index =1.9 which is intercepted by a torus close to the nucleus. At large inclination angles and large torus column densities, the torus produces a considerable amount of Fe Kα emission (i.e. large equivalent widths). For a geometrical structure with the half-opening angle $\sim 45°$, the plot of equivalent width of the 6.4 keV line dependent to the column density is shown in Figure 3 of Ghisellini et al. (1994). The equivalent width estimate for NGC 1386 is 1.4 keV, which corresponds to column density $N_{\rm H} \geq$ a few $\times\ 10^{24}$ atoms cm^{-2}. If this estimate is accurate, NGC 1386 is likely to be a Compton-thick Seyfert galaxy with the transmitted continuum suppressed below 10 keV, and the reflection component playing a dominant role. This scenario is also consistent with the ratio of [O III] λ5007 and X-ray luminosities considered in Section 4.5.2.

4.5.2 The hard X-ray and the [O III] luminosities

The [O III] λ5007 line is a good estimator of the AGN luminosity in both Type 1 and Type 2 AGNs. The integrated [O III] flux of NGC 1386 from *HST* is 5.0 $\times$ 10^{-13} erg s^{-1} cm^{-2} (Ferruit et al. 2000). Assuming an average reddening of E(B-V) $\sim$ 0.4 (see Bennert et al. 2006) for the inner 4$''$ region, the extinction-corrected [O III] luminosity is 2.6 $\times$ 10^{40} erg s^{-1}.

Mulchaey et al. (1994) present the dependence of the 2-10 keV X-ray luminosity and the [O III] luminosity for Type 2 AGN as log $L_{[OIII]}/L_{HX}$ = -1.76. The predicted 2-10 keV X-ray luminosity for NGC 1386 from this correlation is 1.5 $\times$ 10^{42} erg s^{-1}. The observed 2-10 keV X-ray luminosity is 2.7 $\times$ 10^{39} erg s^{-1}, considerably lower than that predicted by the [O III] luminosity. This further suggests that the AGN is heavily absorbed in the X-ray band and the unabsorbed luminosity is significantly larger than the observed value. This is in agreement with the existence of the neutral iron line at 6.4 keV with a large equivalent width discussed in the previous section.

4.5.3 The physical interpretation of the northern blob emission

Using the long-slit spectroscopy obtained with FORS1[2] at the VLT[3], Bennert et al. (2006) find a secondary peak of the electron-density and the ionisation-parameter distribution north of the nucleus. The peak of the ionisation parameter 4$''$ north of the nucleus is close to the northern tip of the [O III] emission with a blue continuum indicating low extinction (Ferruit et al. 2000). Bennert et al. (2006) point out that the

[2]FOcal Reducer/low dispersion Spectrograph.
[3]Very Large Telescope, Cerro Paranal, Chile (ESO).

increased density and the ionisation-parameter originate from shocks by which a radio jet interacting with the line-emitting gas.

The X-ray spatial and spectral information together indicate that the northern blob is a separate feature consistent with this shock scenario. The X-ray blob, about 3″ north of the soft X-ray nucleus, is prominent only below 1 keV. The soft X-ray northern blob appears to overlap with the *HST* optical northern blob, where evidence for shocks exists. The X-ray spectrum of the northern blob can be fitted by a thermal MEKAL model with kT = 0.26 keV. The spectrum can also be approximated by a shock plasma (NPSHOCK) model, though the low quality of the data prevents us from constraining the parameters.

4.5.4 Soft X-ray extended emission

The unique *Chandra* ACIS-S imaging spectroscopy allows us to understand the character of the extended emission in NGC 1386 by combining spatial and spectral information. In the imaging analysis (see Section 4.3), I noted that the X-ray emission is correlated with both the [O III] and the Hα emission, on both small and large scales. In starburst galaxies, the morphological relationship between X-ray and Hα image is usually attributed to collisionally ionized plasma, as a result of starburst-driven superwinds (see for example, NGC 6240 and NGC 2782 in this dissertation). However, in case of NGC 1386, Bianchi et al. (2006) suggested that the spatial correlation between the soft X-ray and [O III] emission indicates that both are related by the photoionized plasma located in the narrow line region. In such a scheme, the photoionized medium extending outside the torus is ionized by the central continuum, reprocessing the incident continuum in the form of emission lines. Our results of the spectral analysis indicate that the soft X-ray extended emission (*excluding* the northern blob) can not be well represented by the XSTAR photoionization model. An approximate description is a bremsstrahlung model or a black-body model. To illustrate the difficulties in explaining the soft X-ray extent as a photoionization medium, I note below the discrepancies found between the data and the XSTAR photoionization model, followd by a discussion of the physical implication of the bremsstrahlung model.

Problems with the XSTAR photonionization models

As shown in the spectral analysis, XSTAR photoionization models can not account for the data: for example, the calculated models are much below the observed data in two narrow energy bands: 0.7-0.9 and 1.0-1.2 keV. This obvious discrepancy makes photoionization models unsuitable as an explanation of the soft X-ray extended emission of NGC 1386. If this problem is due to the inaccurate calculation of Fe-L emission lines between 0.7 and 1.2 keV band in the models, the flux of the "missing" lines should be consistent with that of two or a few Fe-L lines. To check this possibility, two Gaussian lines are introduced to represent the "missing" emission lines, whose energies are 0.8 and 1.1 keV (hereafter G1 and G2), respectively. The ratios of the luminosities of the additional Gaussian lines relative to the luminosity of the XSTAR model in the 0.7-1.2 keV band are measured with the observed spectrum fitted by an XSTAR model plus two Gaussian lines (with XSTAR parameters: log$\xi \sim 2$, $N_{\rm H}$ =3.0×10^{21}cm^{-2}).

The measured ratios are 0.436 and 0.527 for G1 and G2, respectively. On the other hand, the luminosity ratio of the entire Fe-L complex relative to the whole XSTAR component in the 0.7-1.2 keV is always around 0.1 or even smaller (see Table 4.3). Obviously, the luminosities of the two additional Gaussian lines are too large to explain as the luminosities of the "missing" Fe-L emission lines. Moreover, Table 4.3 gives the relative strengths of the emission lines from other elements. The emission lines of other elements appear to dominate all the iron lines over a relative wide range of parameter space. Consequently, the contribution from a single Fe-L line to the whole luminosity in XSTAR model should be relatively small. This also indicates two or even a few "missing" Fe-L lines in the 0.7-1.2 keV range is not likely to explain the large discrepancy observed (see Figure 4.11). Therefore, it is reasonable to rule out the possibility that the discrepancy is due to uncertainty in the Fe-L emission computation. Because of the large residuals (see Figure 4.11), it is difficult to model the spectrum of soft X-ray extended emission (*excluding* the northern blob) by the XSTAR photonionization model. More complex models or scenarios might give a better interpretation, but this requires better data quality. Based on the current, low quality data, there is an unavoidable problem in explaining the soft extended emission as emission from a photoionized scattering medium. We conclude that high-resolution X-ray spectral data are absolutely necessary in order to determine the nature of X-ray extension in NGC 1386.

Implications of the bremsstrahlung model

The soft X-ray extended emission can be modelled by a bremsstrahlung model with photoelectric absorption, implying that hot gas (a few $\times$ 10^6 K) emission contributes to the observed X-ray extended emission. The density of the hot gas can be inferred from the thermal bremsstrahlung description. For the bremsstrahlung model,

$$NORM_{Brem} = 3.02 \times 10^{-15} \int n_e n_I dV/(4\pi D^2)$$

where $NORM_{Brem}$ is the normalization of the bremsstrahlung model, n_e is the electron density, n_I is the ion density, and D is the distance to the source (all in cgs units). We assume that the hot gas in the observed extended region uniformly fills two cylinders (representing the northern and southern parts), each of them with a radius of 50 pc and a height of 300 pc (estimated from X-ray images). Assuming $n_e n_I \approx n_h^2$, the hot gas density n_h can be calculated,

$$n_h = \begin{cases} 3 \quad cm^{-3}, \quad if \quad NORM_{Brem} = 1.53 \times 10^{-4} & (1) \\ 10 \quad cm^{-3}, \quad if \quad NORM_{Brem} = 1.52 \times 10^{-3} & (2) \end{cases}$$

where (1) stands for a model with $k\mathbf{T}$=0.45 keV or 5.2 $\times$ 10^6K and (2) for $k\mathbf{T}$=0.24 keV or 2.7 $\times$ 10^6K (see Table 4.1). The spatial correlation between the extended soft X-rays and the extended forbidden-line gas in NGC 1386 suggests that the hot X-ray gas share the same spatial scale with optical narrow-line-emitting clouds. This implies that at least two phases are located in the plasma, one being hot (a few $\times$ 10^6 K) and the other warm ($\geq$ 10^4 K, Bennert et al. 2006). Krolik & Vrtilek (1986) offer a

Table 4.3: The luminosity ratios of the emission lines from Fe-L and other elements relative to the luminosity of the total 0.7-1.2 keV of the photoionized gas. The total 0.7-1.2 keV luminosity includes: 1) the luminosities of the emission lines from iron and other elements, and 2) recombination continuum luminosities.

Case	Log(ξ)	Other Elements	Iron
$N_{\rm H} = 1.0 \times 10^{20}$ cm^{-2}			
1	1.5	0.477	0.125
2	2.0	0.569	0.078
3	2.5	0.627	0.037
4	3.0	0.640	0.035
5	3.5	0.633	0.033
$N_{\rm H} = 1.0 \times 10^{21}$ cm^{-2}			
6	1.5	0.470	0.125
7	2.0	0.556	0.087
8	2.5	0.617	0.044
9	3.0	0.641	0.028
10	3.5	0.608	0.033
$N_{\rm H} = 3.0 \times 10^{21}$ cm^{-2}			
11	1.5	0.454	0.123
12	2.0	0.530	0.103
13	2.5	0.513	0.081
14	3.0	0.530	0.055
15	3.5	0.552	0.040
$N_{\rm H} = 5.0 \times 10^{21}$ cm^{-2}			
16	1.5	0.446	0.104
17	2.0	0.428	0.132
18	2.5	0.453	0.110
19	3.0	0.487	0.079
20	3.5	0.521	0.054
$N_{\rm H} = 1.0 \times 10^{22}$ cm^{-2}			
1	1.5	0.400	0.072
22	2.0	0.398	0.083
23	2.5	0.404	0.129
24	3.0	0.443	0.107
25	3.5	0.442	0.106

scenario in which the warm optical narrow-line-emitting clouds are entrained by a hot nuclear wind outflowing the center of the galaxy. Bennert et al. (2006) estimate a high and low densities of 1540 and 50 cm^{-3}, respectively, and a temperature of $T_e \simeq$15650 K. Assuming the average density is 800 cm^{-2}, the pressure $n_e T_e = 1.25 \times 10^7$ cm^{-3} K. If the warm and hot clouds are in rough pressure equilibrium, such that $n_e T_e = n_h T_h$, the required density of the hot phase gas with a thermal bremsstrahlung temperature of T_h=5.2 keV or 2.7 $\times$ 10^6 K, should be 2 or 5 cm^{-3}. This is close to the hot gas density calculated from the thermal bremsstrahlung fits to the *Chandra* data.

Better signal-to-noise observations are necessary to search for weak spectral features in the soft X-ray band. A longer *Chandra* exposure would allow us to detect features associated with any photoioninzed gas and/or collisionally ionized plasma, as well as a thorough testing of complex models for the soft X-ray emission.

4.6 Summary

I analyzed the high-resolution X-ray imaging spectroscopy of NGC 1386 with *Chandra* X-ray observatory. The high-resolution image shows a hard X-ray nucleus located at the center of NGC 1386 and soft X-ray extended emission below 2 keV. The soft X-ray emission is spatially resolved and extends out to ∼300 pc northwardly and southwardly from the center, along P.A.∼ 5°. A northern blob is also resolved, about 3″ north of the center. I overlaid the X-ray image and optical emission-line images. The close spatial correlation between the extended soft X-rays and optical line emission (e.g. [O III] λ5007) can be clearly seen on hundreds of parsecs scale. Moreover, the enhanced soft X-ray emission from the blob is consistent with the shock scenario and can be treated as a separate feature based on the coincidence of the soft X-ray northern blob and the [O III] northern blob.

Our spectral analysis suggests that the photoionized plasma models can not explain the spectrum of the extended emission. A black-body or a bremsstrahlung model on the other hand do provide a crude parameterization of the spectrum.

The hard X-ray spectrum of the nucleus is fitted by a power-law plus Fe Kα emission line at 6.4 keV, while the soft excess of the nuclear spectra can be approximated by a black-body or a bremsstrahlung model (assuming the soft excess is from an accretion disk about the central black hole). The large equivalent width (∼ 1.4 keV) of the Fe Kα line indicates that the intrinsic column density, $N_{\rm H}$, is greater than 10^{24} cm^{-2}. The predicted hard X-ray luminosity from the Mulchaey et al. (1994) correlation of log $L_{[OIII]}/L_{HX}$ = -1.76, is considerably higher than the observed value, consistent with the heavily absorbed AGN scenario.

CHAPTER 5
CONCLUDING REMARKS AND PROSPECTIVE VIEWS

The X-ray properties of three galaxies, NGC 6240, NGC 2782, and NGC 1386, are analyzed in this dissertation. All the X-ray data are obtained from *Chandra* ACIS-S observations. In this chapter, I will summarize the general conclusions, discuss their implications, and provide some prospective views of follow-up investigations and future observations with the current and new X-ray missions.

5.1 Concluding remarks

5.1.1 The nature of the soft X-ray emission

An important result of this thesis is the realization that the soft X-ray emission in these three sources originates in different emission processes. Although the soft X-ray emission is spatially resolved in all three galaxies, the spectral decompositions indicate that the soft X-ray emission is due to different emission mechanisms.

One possibility to interpret the soft X-ray emission is thermal emission due to collisionally ionized plasma which is present in both NGC 6240 and NGC 2782. This thermal plasma model is associated with the presence of a starburst. The relations between the diffuse X-ray and the Hα emission observed indicate morphological correlations between the two gas phases in both the ULIRG (NGC 6240) and the starburst galaxy (NGC 2782). The correlation between the soft X-ray and the optical line emission is suggestive of a scenario in which the interaction between the hot outflow and the ambient medium in the disk and halo of ULIRGs and/or starbursts galaxies produces the observed emission.

Another possibility is that the soft X-rays emission originates in a photoionized gas, as seen in the Seyfert 2 galaxy NGC 1068. For NGC 1386, various observations point toward a relation between the soft X-ray emission and the narrow line region. Thus, a photoionizaion model is expected to fit the observed soft X-ray emission. However, we found that a photoionizaion model (produced by a XSTAR code) can not well represent the spectra of the soft X-ray extended emission; consequently, the question of the nature of soft X-ray extended emission in NGC 1386 remains open.

5.1.2 X-ray emission associated with Starburst activity

A noteworthy result of this study is the characterization of the X-ray emission related to the starburst activity in NGC 6240 and NGC 2782. I summarize the main properties of both galaxies in Table 5.1. In this section, I will compare the results and comment on the diffuse components and point-like sources.

Thermal diffuse components

As a ULIRG, NGC 6240 has a weak, large-scale halo component extending up to 40 kpc and spectacular bright "butterfly"-shaped feature in the inner $\sim$ 10 kpc. The soft X-ray emission from the halo component is well modelled by a single-temperature thermal

plasma model with kT $\sim$ 0.6 keV. In addition to the 0.6 keV thermal component, a second thermal component with kT $\sim$ 1.0 keV is required to describe the soft emission of "butterfly-shaped" structure.

For NGC 2782, the inner part (within $\sim$ 2.5 kpc) of the extended emission is much brighter than the outer part (at radii $\geq$ 2.5 kpc, extending to 7.5 kpc). For easily comparison with NGC 6240, I define the outer part of NGC 2782 as the halo region. X-ray spectral data of either the inner bright extent or the halo region can be fitted by a single-temperature thermal model. The temperature of the inner part (kT$\sim$0.7 keV) is a little bit higher than that of the halo component (kT$\sim$0.6 keV), but the small difference is insignificant.

We should keep in mind that the best-fit plasma temperature(s) at a given starburst region should be viewed as only an emission-measured simplification and not as representing the true physical state of the X-ray emitting gas, since the actual thermal plasma is most likely to be a phase continuum of states (Strickland & Stevens 2000). The main properties of NGC 6240 and NGC 2782 can be summarized as follows (see also Table 5.1):

1. NGC 6240 is one of the nearest ULIRGs and a key representative of its class. NGC 2782 is an edge-on starburst galaxy.

2. The soft X-ray emission of both galaxies shows evidence for starburst-driven superwinds. The superwinds in two galaxies differ in dynamical timescales and observed physical sizes. The X-ray emission associated with superwinds of NGC 6240 is correlated with Hα emission. For NGC 2782, only the shell-like structure at 5-8$''$ south of the core source is observed in all X-ray, Hα and radio images.

3. The diffuse X-ray plasma of NGC 6240 has the emission-measured temperatures of 0.6 and 1.0 keV. For NGC 2782, the temperature of the thermal diffuse component is 0.6-0.7 keV.

4. The physical sizes of the diffuse X-ray plasma in NGC 6240 (bright extent: inner $\sim$ 10 kpc; halo: $\sim$ 10-40 kpc) are larger than those of NGC 2782 (bright extent: inner $\sim$ 2 kpc; halo: $\sim$ 2-8 kpc).

5. In comparison to NGC 2782, NGC 6240 has a higher SFR and larger X-ray luminosities of both the halo region and bright component.

The similarities and differences between two galaxies pose quite a few interesting questions which we discuss Section 5.2.

X-ray point sources

With *Chandra* subarcsecond angular resolution, the emission from individual point-like sources can be isolated from the diffuse emission of hot gases, both spatially and spectroscopically (see Fabbiano 2006 for a recent review). There are five off-nuclear point sources detected in NGC 2782. The brightest source has about 60 counts in the *Chandra* ACIS-S exposure. If a power-law spectral shape is assumed with a photon index of $\Gamma \sim 1.9$, the luminosity of this brightest source is estimated to be $\sim 10^{40}$ erg s^{-1}. Based on its high X-ray luminosity, this source is likely to be a Ultraluminous X-ray source (ULX).

Although no off-nuclear point sources are detected in NGC 6240, it does not provide the absence of such sources. The NGC 6240 point sources (e.g. X-ray binaries) might

Table 5.1: Comparison of the properties of NGC 6240 and NGC 2782 (see the text for more details).

Properties	NGC 6240	NGC 2782
Distance[a]	144 Mpc	51 Mpc
Type	ULIRG	edge-on Starburst[b]
	Starburst+ a binary AGN	+ a hidden AGN?
L^{c}_{FIR}	6.6×10^{11} $L_{\odot}$	3.6×10^{10} $L_{\odot}$
SFR[d]	115 $M_{\odot}$ yr^{-1}	6.2 $M_{\odot}$ yr^{-1}
Superwinds[e]:		
Dynamical timescale	$\sim 10^{7}$yr	4×10^{6}yr
Physical size	$\sim$10 kpc	$\sim$2 kpc
X-ray properties of the weak halo emission:		
Physical size	$\sim$10-40 kpc	$\sim$2-8 kpc
Thermal emission	$kT \sim 0.6$ keV	$kT \sim 0.6$ keV
Luminosity	$L_{0.5-2.5keV}=4.8 \times 10^{41}$ erg s^{-1}	$L_{0.5-2.5keV}=1.7 \times 10^{41}$ erg s^{-1}
X-ray properties of the bright extended emission:		
Physical size	inner $\sim$10 kpc	inner $\sim$2 kpc
Column density $N_{\rm H}$	$1\text{-}3 \times 10^{21}$cm^{-2}	$\sim 10^{21}$cm^{-2}
Thermal emission	$kT_1 \sim 0.6$ keV	$kT \sim 0.7$ keV
	$kT_2 \sim 1.0$ keV	
Non-thermal emission	$\Gamma \sim 1.0\text{-}1.6$	
Luminosity	$L_{0.5-10keV}=2.9 \times 10^{42}$ erg s^{-1}	$L_{0.5-2.5keV}=5.0 \times 10^{40}$ erg s^{-1}
X-ray Off-nuclear point sources	none detected	5 detected
		$L_{x,max} \sim 10^{40}$ erg s^{-1}

[a]Distances assuming H_o=50 km s^{-1} Mpc^{-1}.
[b]Note that our study indicates that NGC 2782 is likely to host an obscured AGN.
[c]FIR flux is defined (Helou et al. 1985) as a combination of *IRAS* 60 μm and 100 μm fluxes according to $f_{FIR} = 1.26 \times 10^{-11}$ (2.58 f_{60} + f_{100}) erg s^{-1} cm^{-2}, where f_{60} and f_{100} are given by Sanders et al. (2003).
[d]SFRs determined by the Kennicutt (1998) law: SFR = $L_{FIR}/2.2 \times 10^{43}$ $M_{\odot}$ yr^{-1}.
[e]References: Schulz et al. (1998), Tecza et al. (2000), Boer et al.(1992), Smith (1994), Jogee et al. (1998).

be embedded in the bright diffuse emission and difficult to detect over the diffuse backgrounds. The upper limit for the luminosity of off-nuclear point-like sources is $\sim 10^{40}$ ergs s^{-1}, estimated from a MARX simulation. It is possible that NGC 6240, like The Antennae (NGC 4038/4039), contains a large number of X-ray point sources with luminosities $\leq 10^{40}$ ergs s^{-1}, which are difficult to resolve over the hot diffuse emission.

5.1.3 X-ray emission due to AGN activity

Previous studies indicate the presence of Compton-thick AGNs in both NGC 6240 and NGC 1386. The analysis presented in this dissertation confirm this result: the reflection components dominate the nuclear emission at energies lower than 10 keV.

There is *marginal* evidence of extended hard X-ray emission (a few arcseconds) in the center of NGC 6240, due to either the spread of the PSF or scattered nuclear emission. The dense molecular clouds concentrated in the central 3″ can be responsible for reflecting X-rays and for the observed strong iron K fluorescence line at 6.4 keV. A high-quality Fe Kα band (6.2-6.5 keV) image would be very useful to investigate the nature of this reflection. It requires a deeper *Chandra* ACIS-S observation since longer exposure can reveal more details in a narrow energy band image.

In addition to the iron K shell fluorescence line at 6.4 keV, the *Chandra* X-ray spectrum of the southern nucleus of NGC 6240 likely shows further line-emission components: He-like and H-like lines at 6.70 and 6.96 keV, respectively. This indicates additional complexity for the southern nucleus, a part from the warm scattered component (which is related to the spatially extended jet-like structure). Assuming a photonionized medium in the jet-like structure surrounding the southern nucleus, the scattered luminosity L^{sc} is estimated (2.5×10^{41} erg s^{-1}), which is close to the observed luminosity.

In this dissertation, I find evidence for the existence of an Fe Kα line emission with large equivalent width of 900 eV from the core source of NGC 2782, indicative of the presence of Compton-thick AGN. I also use various ratios of the X-ray to optical emission to discriminate between different process (e.g. $L_{0.1-2.4keV}/L_{H\alpha}$ and $L_{2-10keV}/L_{[OIII]}$ ratios). The results suggest that the direct component of AGN seems to be heavily suppressed and only a fraction of the total luminosity can be observed. The observed X-ray luminosity in 0.5-10 keV of the nuclear source is 1.3×10^{41} erg s^{-1}. With an X-ray luminosity less than 10^{42} erg s^{-1}, NGC 2782 is likely to host an obscured AGN. However, the possibility that there is an ULX in the center of NGC 2782 can not be firmly ruled out. Further studies are required to resolve this question.

5.2 Future prospects

5.2.1 Further studies of individual galaxies

Although the *Chandra* ACIS-S data of NGC 6240, NGC 2782 and NGC 1386 have been minutely analyzed in this study, a number of open issues require attention. Further studies of these objects will deepen our understandings of the physical nature of AGN and starbursts.

NGC 6240

Obtaining deeper *Chandra* ACIS-S observations of NGC 6240 are essential to better understand the nature of this galaxy.

For example, since there is only *marginal* evidence for the presence of an extended hard X-ray emission in the center of the galaxy, this results needs confirmation. Does the cold gas provide the scattering agent? This could be clarified by investigating a high-quality Fe Kα line emission image in deeper *Chandra* observations. If the surface brightness distribution of the hard X-ray emission is found to be asymmetrical and/or disturbed, it would imply that the extension is real.

I find *slight* evidence for iron lines at energies higher than 6.4 keV in the X-ray spectrum of the southern nucleus, possibly due to Fe XXV at 6.7 keV and Fe XXVI at 6.97 keV, indicative of the presence of "warm mirror" (the highly ionized medium). The existence of those lines has been confirmed by an *XMM* observation (Boller et al. 2003). Longer *Chandra* observations with increased photon statistics and higher spectral quality would provide more convincing evidence that both ionized iron lines originate in the southern nucleus and the warm scattered medium extending to the "jet"-like structure.

Generally, hardness ratio images are usually used as tools for investigating the emission properties of the X-ray emitting gases and/or the distribution of foreground column densities. As summarized in Section 5.1.2, there is a tendency of increasing thermal plasma temperature with increasing column densities. Furthermore, the actual thermal plasma in starburst regions is likely a phase continuum of states. Producing hardness ratio images, e.g. by dividing the 0.5-1.0 keV image by the 1.0-1.5 keV image, can help us explore how the emission properties change. Unfortunately, the photon counts in the soft energy bands are so limited that some artificial features appear in the hardness ratio image. Similarly, the low photon statistics prevents us from studying the the abundance gradients by using the oxygen line image, the iron line image, and so on. In order to obtain the high-quality hardness-ratio images and emission-line images allowing us to obtain detailed information of the X-ray emitting gases. A longer *Chandra* ACIS-S observations of NGC 6240 is required.

NGC 2782

Future long *Chandra* exposures of NGC 2782 are also of the great importance. Sufficient counts are expected to produce hardness ratio images, emission line images, and to allow us to model the extended emission spectra with more accurate parameters (e.g. constraining the temperature, the metal abundances, etc.).

As shown in the study of NGC 2782, the extended X-ray emission (including both the northern and the southern extended emission), can be modelled by a single-temperature plasma. With the currently available data, the extended emission can only be studied as a whole, while neither the northern nor the southern part has sufficient photon statistics to allow separate spectral fits. Such analysis could yield better constraints on the emission processes governing the two regions.

Another important question worthy of further analysis is the relation between the different features observed in the optical and the X-ray bands. The correlations between

the X-ray and optical emission do not always occur: for example, the clumpy arclike feature about 3″ north of the core emission in the Hα image has no X-ray counterpart. There are two possible interpretations presented in Section 3.5. More studies are necessary to distinguish between the two.

A longer-exposure *Chandra* ACIS-S observations will allow us to study in detail the five off-nuclear point sources through spectral fitting, and to obtain more convincing evidence for or against the presence of AGN activity in NGC 2782.

NGC 1386

The detailed spectral analysis is currently limited by the quality of the extended (and likely related to the NLR) soft X-ray emission spectrum. A thorough determination of the physical properties of the extended soft X-ray emission in NGC 1386 also requires deeper exposures with high-resolution detectors. Since photonionization of optically thin, low-density material does produce line emission, future high resolution spectra and improved XSTAR modelling are crucial.

5.2.2 Large samples studies and new observations

Merger sequences link starburst and AGN activities together. The physical pictures are apparently complex, dependent on the details of the encounters producing the merger. In this dissertation, two merger systems (NGC 6240 and NGC 2782) show both diverse and common characteristics in the X-rays band. Many interesting questions can be posed. For example, Which parameters have effect on the various stellar and non-stellar contributions to the X-ray emission? What are the robust estimators of the relative contributions of the starburst and the AGN activity in the different merger scenarios? How do these starburst and AGN activities evolve in the X-ray band along the merger sequence? Are there any trends of the variations in these two activities with merger stage, morphology, mass, starburst histories, etc.? To obtain a realistic representation of a merger, large sample studies and high-quality data of merger systems (including many ULIRGs and starburst galaxies), are necessary. Such studies are possible today based on current *Chandra* and *XMM-Newton* data.

The future brings great promise of accurate research of the X-ray properties of both AGNs and starburts. For instance, the Fe Kα line associated with AGN activity can be well studied by *Suzaku* (since 2005). Taking advantage of its broad bandpass (0.3 - 100 keV) and its high effective area at $\sim$ 6 keV as well as the good spectral resolution, we will be able to obtain accurate models of the continuum and the Fe Kα line emission. The high ($\sim$few eV) energy resolution of the X-ray calorimeter on *Constellation-X* should allow many individual X-ray lines to be resolved. It might be possible to determine the temperature range and metal abundances for multi-phase starburst components by a study of a large number of independent emission-line ratios, replacing the current method of attempting to fit complex models to low resolution spectra.

REFERENCES

Anders E., Grevesse N., 1989, GeCoA, **53**, 197

Antonucci R.R.J., Miller J.S., 1985, ApJ, **297**, 621

Antonucci R., 1993, ARA&A **31**, 473

Balestra I., Boller Th., Gallo L., Lutz D., Hess S., 2005, A&A, **442**, 469

Band D.L., Klein R.I., Castor J.I., Nash J.K., 1990, ApJ, **362**, 90

Bennert N., Jungwiert B., Komossa S., Haas M., Chini R., 2006, A&A, **446**, 919

Beswick R.J., Pedlar A., Mundell C.G., Gallimore J.F., 2001, MNRAS, **325**, 151

Bianchi S., Guainazzi M., Chiaberge M., 2006, A&A, **448**, 499

Boer B., Schulz H., Keel W.C., 1992, A&A, **260**, 67

Bohlin R.C., Savage B.D., Drake J.F., 1978, ApJ, **224**, 132

Boller Th., Keil R., Hasinger G., Costantini E., Fujimoto R., Anabuki N., Lehmann I., Gallo L., 2003, A&A, **411**, 63

Borkowski K.J., Lyerly W.J., Reynolds S.P., 2001, ApJ, **548**, 820

Braito V., Della Ceca R., Piconcelli E., Severgnini P., Bassani L., Cappi M., Franceschini A., Iwasawa K., Malaguti G., Marziani P., Palumbo G.G.C., Persic M., Risaliti G., Salvati M., 2004, A&A, **420**, 79

Brandt W.N., Hasinger G., 2005, ARA&A, **43**, 827

Brinkman A.C., Kaastra J.S., van der Meer R.L.J., Kinkhabwala A., Behar E., Kahn S.M., Paerels F.B.S., Sako M., 2002, A&A, **396**, 761

Calzetti, D., 2001, PASP, **113**, 1449

Cappi M., Panessa F., Bassani L., Dadina M., Dicocco G., Comastri A., della Ceca R., Filippenko A.V., Gianotti F., Ho L.C., Malaguti G., Mulchaey J.S., Palumbo G.G.C., Piconcelli E., Sargent W.L.W., Stephen J., Trifoglio M., Weaver K.A., 2006, A&A, **446**, 459

Cardelli J.A., Clayton G.C., Mathis J.S., 1989, ApJ**345**, 245

Cash W., 1979, ApJ, **228**, 939

Cecil G., Bland-Hawthorn J., Veilleux S., 2002, ApJ, **576**, 745

Chevalier R.A., Clegg A.W., 1985, Nature, **317**, 44

Colbert E.J.M., Wilson A.S., Bland-Hawthorn J., 1994, ApJ, **436**, 89

Colbert E.J.M., Heckman T.M., Ptak A.F., Strickland D.K., Weaver K.A., 2004, ApJ, **602**, 231

Dahlem M., Weaver K.A., Heckman T.M., 1998, ApJS, **118**, 401

Dickey J.M., Lockman F.J., 1990, ARA&A**28**, 215

Done C., Madejski G.M., Smith D.A., 1996, ApJ, **463**, 63

Fabbiano G., Kim D.W., Trinchieri G., 1992, ApJS, **80**, 531

Fabbiano G., Zezas A., Murray S.S., 2001, ApJ, **554**, 1035

Fabbiano G., Baldi A., King A.R., Ponman T.J., Raymond J., Read A., Rots A., Schweizer F., Zezas A., 2004, ApJ, **605**, 21

Fabbiano G., 2006, ARA&A, **44**, 323

Ferruit P., Wilson A.S., Mulchaey J., 2000, ApJS, **128**, 139

Fosbury R.A.E., Wall J.V., 1979, MNRAS, **189**, 79

Franceschini A., Braito V., Persic M., Della Ceca R., Bassani L., Cappi M., Malaguti P., Palumbo G.G.C., Risaliti G., Salvati M., Severgnini P., 2003, MNRAS, **343**, 1181

Fried J.W., Schulz H., 1983, A&A, **118**, 166

Gallagher S.C., Brandt W.N., Chartas G., Garmire G.P., Sambruna R.M., 2002, ApJ, **569**, 655

Gallimore J.F., Beswick R., 2004, AJ, **127**, 239

Genzel R., Lutz D., Sturm E., Egami E., Kunze D., Moorwood A.F.M., Rigopoulou D., Spoon H.W.W., Sternberg A., Tacconi-Garman L.E., Tacconi L., Thatte N., 1998, ApJ, **498**, 579

Gerssen J., van der Marel R.P., Axon D., Mihos J.C., Hernquist L., Barnes, J.E., 2004, AJ, **127**, 75

Ghisellini G., Haardt F., Matt G., 1994, MNRAS, **267**, 743

Gilfanov M., 2004, PThPS, **155**, 49

Grimes J.P., Heckman T., Strickland D., Ptak A., 2005, ApJ, **628**, 187

Grimm H.-J., Gilfanov M., Sunyaev R., 2003, MNRAS, **339**, 793

Guainazzi M., Matt G., Brandt W.N., Antonelli L.A., Barr P., Bassani L., 2000, ApJ, **356**, 463

Halderson E.L., Moran E.C., Filippenko A.V., Ho L.C., 2001, AJ, **122**, 637

Heckman T.M., Armus L., Miley G.K., 1987, AJ, **93**, 276

Heckman T.M., Armus L., Miley G.K., 1990, ApJS, **74**, 833

Heckman T.M., Lehnert M.D., Armus L., The nearest active galaxies. Coleccion Nuevas Tendencias, Proceedings of the meeting held in Madrid in May 1992. Edited by John Beckman, Luis Colina and Hagai Netzer. Published by Consejo Superior de Investigaciones Cientificas, Madrid, 1993a, p.133

Heckman T.M., Lehnert M.D., Armus L., 1993b in "The Environment and Evolution of Galaxies", edited by J. Michael Shull and Harley A. Thronson. Astrophysics and Space Science Library, Vol. **188**, p.455

Heckman T.M., Dahlem M., Eales S.A., Fabbiano G., Weaver K., 1996, ApJ, **457**, 616

Heckman T.M., 1998, ASPC, **148**, 127

Heckman T.M., 2000, Philosophical Transactions of the Royal Society of London, Series A, Vol. 358, no. 1772, p.2077

Heckman T.M., Gas and Galaxy Evolution, ASP Conference Proceedings, Vol. 240. Edited by John E. Hibbard, Michael Rupen, and Jacqueline H. van Gorkom. San Francisco: Astronomical Society of the Pacific, ISBN: 1-58381-077-3, 2001, p. 345

Heckman T.M., 2003, Galaxy Evolution: Theory & Observations (Eds. Vladimir Avila-Reese, Claudio Firmani, Carlos S. Frenk & Christine Allen) Revista Mexicana de Astronomíay Astrofísica (Serie de Conferencias) Vol. 17, pp. 47-55

Helou G., Soifer B.T., Rowan-Robinson M., 1985 ApJ**298**, 7

Ho L.C., Filippenko A.V., Sargent W.L.W., 1997, ApJS, **112**, 315

Ho L.C. 1999, AdSpR, **23**, 813

Huo Z.Y., Xia X.Y., Xue S.J., Mao S., Deng Z.G., 2004, ApJ, **611**, 208

Imanishi M., Dudley C.C., 2000, ApJ, **545**, 701

Iwasawa K. Comastri A., 1998, MNRAS, **297**, 1219

Iyomoto N., Makishima K., Fukazawa Y., Tashiro M., Ishisaki y., 1997, PASJ **49**, 425

Jansen F., Lumb D., Altieri B., Clavel J., Ehle M., Erd C., Gabriel C., Guainazzi M., Gondoin P., Much R., Munoz R., Santos M., Schartel N., Texier D., Vacanti G., 2001, A&A, **365**, 1

Jogee S., Kenney J.D.P., Smith B.J., 1998 ApJ, **494**, 185

Kallman T., Bautista M., 2001, ApJS, **133**, 221

Kennicutt R.C.Jr., 1998 ApJ, **498**, 541

Kinkhabwala A., Sako M., Behar E., Kahn S.M., Paerels F., Brinkman A.C., Kaastra J.S., Gu M.F., Liedahl D.A., 2002, ApJ, **575**, 732

Komossa S., Schulz H., Greiner J., 1998, A&A, **334**, 110

Komossa S., Burwitz V., Hasinger G., Predehl P., Kaastra J.S., Ikebe Y., 2003, ApJ, **582**, 15

Komossa S., Hasinger G., Schulz H., International Astronomical Union Symposium no. 217, held 14-17 July, 2003 in Sydney, Australia. Edited by P.-A. Duc, J. Braine, and E. Brinks. San Francisco: Astronomical Society of the Pacific, 2004., p.338

Krolik J.H., Vrtilek J.M., 1984, ApJ, **279**, 521

Leahy D.A., Creighton J., 1993, MNRAS, **263**, 314

Lehnert M.D., Heckman T.M., 1996, ApJ, **472**, 546

Lehnert M.D., Heckman T.M., Weaver K.A., 1999, ApJ, **523**, 575

Lira P., Ward M.J., Zezas A., Murray S.S., 2002, MNRAS, **333**, 709

Lonsdale C.J., Farrah D., Smith, H., astro-ph/0603031; Review article, published in "Astrophysics Update 2 - topical and timely reviews on astronomy and astrophysics". Ed. John W. Mason. Springer/Praxis books. ISBN: 3-540-30312-X.

Lutz D., Veilleux S., Genzel R., 1999, ApJ, **517**, 13

Maccacaro T., Perola G.C., Elvis M., 1982, ApJ, **257**, 47

Magdziarz P., Zdziarski A.A., 1995, MNRAS, **273**, 837

Maiolino R., Comastri A., Gilli R., Nagar N.M., Bianchi S., Böker T., Colbert E., Krabbe A., Marconi A., Matt G., Salvati M., 2003, MNRAS, **344**, 59

Marshall F.E., Netzer H., Arnaud K.A., Boldt E.A., Holt S.S., Jahoda K.M., Kelley R., Mushotzky R.F., Petre R., Serlemitsos P.J., Smale A.P., Swank J.H., Szymkowiak A.E., Weaver K.A., 1993, ApJ, bf 405, 168

Martin C.L., Kobulnicky H.A., Heckman T.M., 2002, ApJ, **574**, 663

Mateos S., Barcons X., Carrera F.J., Ceballos M.T., Hasinger G., Lehmann I., Fabian A.C., Streblyanska A., 2005, A&A, **444**, 79

McCarthy P.J., van Breugel W., Heckman T., 1987, AJ, **93**, 264

McDowell J.C., Clements D.L., Lamb S.A., Shaked S., Hearn N.C., Colina L., Mundell C., Borne K., Baker A.C., Arribas S., 2003, ApJ, **591**, 154

Mitsuda K., Seventeeth Texas Symposium on Relativistic Astrophysics and Cosmology, Edited by Hans Böhringer, Gregor E. Morfill, and Joachim E. Trümper. Annals of the New York Academy of Sciences, Vol. 759 (New York, NY: The New York Academy of Sciences), 1995., p.213

Morrison R., McCammon D., 1983, ApJ, **270**, 119

Mulchaey J.S., Koratkar A., Ward M.J., Wilson A.S., Whittle M., Antonucci R.R.J., Kinney A.L., Hurt T., 1994, ApJ, **436**, 586

Mushotzky R.F., Done C., Pounds K.A., 1993, ARA&A, **31**, 717

Mushotzky R.F., Cowie L.L., Barger A.J., Arnaud K.A., 2000, Naturr, **404**, 459

Nagar N.M., Wilson A.S., Mulchaey J.S., Gallimore J.F., 1999, ApJS, **120**, 209

Nandra K., Pounds K.A., 1994, MNRAS, **268**, 405

Nandra K., Mushotzky R.F., Arnaud K., Steidel C.C., Adelberger K.L., Gardner J.P., Teplitz H.I., Windhorst R.A., 2002, ApJ, **576**, 625

Ogle P.M., Brookings T., Canizares C.R., Lee J.C., Marshall H.L., 2003, A&A, **402**, 849O

Osterbrock D.E., 1989, in: Astrophysics of Gaseous Nebulae and Active Galactic Nuclei, University Science Books

Panessa F, Bassani L., 2002, A&A, **394**, 435

Persic M., Rephaeli Y., 2002, A&A, **382**, 843

Persic M., Rephaeli Y., Braito V., Cappi M., Della Ceca R., Franceschini A., Gruber D.E., 2004, A&A, **419**, 849

Pettini M., Steidel C.C., Adelberger K.L., Dickinson M., Giavalisco M., 2000, ApJ, **528**, 96

Phillips M. M., Charles P.A., Baldwin J.A., 1983 ApJ, **266**, 485

Ptak A., Serlemitsos P., Yaqoob T., Mushotzky R., Tsuru T., 1997, AJ, **113**, 1286

Ptak A., Serlemitsos P., Yaqoob T., Mushotzky R., 1999, ApJS, **120**, 179

Ptak A., Heckman T., Levenson N.A., Weaver K., Strickland D., 2003, ApJ, **592**, 782

Ranalli P., Comastri A., Setti G., 2003, A&A, **399**, 39

Rieke G.H., Low F.J., 1972, ApJ, **176**, 95

Risaliti G., Maiolino R., Salvati M., 1999, ApJ, **522**, 157

Roberts T.P., Warwick R.S., Ward M.J., Murray S.S., 2002, MNRAS, **337**, 677

Saikia, D. J.; Pedlar, A.; Unger, S. W.; Axon, D. J. 1994, MNRAS, **270**, 46

Sanders D.B., Soifer B.T., Elias J.H., Madore B.F., Matthews K., Neugebauer G., Scoville N.Z., 1988, ApJ, **325**, 74

Sanders D.B., Mirabel I.F., 1996, ARA&A, **34**, 749

Sanders D.B., Mazzarella J.M., Kim D.-C., Surace J.A., Soifer B.T., 2003 AJ, **126**, 1607

Seyfert C.K., 1943, ApJ, **97**, 28

Schulz H., Komossa S., Berghofer T.W., Boer B., 1998, A&A, **330**, 823

Smith, Beverly J. 1994, AJ, **107**, 1695

Stevens I.R., Read A.M., Bravo-Guerrero J., 2003, MNRAS, **343**, 47

Strickland D.K., Heckman T.M., Weaver K.A., Dahlem M., 2000, AJ, **120**, 2965

Strickland D.K., Stevens I.R., 2000, MNRAS, **314**, 511

Strickland D.K., Heckman T.M., Weaver K.A., Dahlem M., 2000, AJ, **120**, 2965

Strickland D.K., Colbert E.J.M., Heckman T.M., Weaver K.A., Dahlem M., Stevens I.R., 2001, ApJ, **560**, 707

Strickland D.K., Heckman T.M., Weaver K.A., Hoopes C.G., Dahlem M., 2002, ApJ, **568**, 689

Strickland D.K., Heckman T.M., Colbert E.J.M., Hoopes C.G., Weaver K.A., 2004, ApJS, **151**, 193

Suchkov A.A., Balsara D.S., Heckman T.M., Leitherner C., 1994, ApJ, **430**, 511

Tacconi L.J., Genzel R., Tecza M., Gallimore J.F., Downes D., Scoville N.Z., 1999, ApJ, **524**, 732

Tecza M., Genzel R., Tacconi L.J., Anders S., Tacconi-Garman L.E., Thatte N., 2000 ApJ, **537**, 178

Teng S.H., Wilson A.S., Veilleux S., Young A.J., Sanders D.B., Nagar N.M., 2005, ApJ, **633**, 664

Thronson H.A.Jr., Majewski S., Descartes L., Hereld M., 1990, ApJ, **364**, 456

Tsuru T.G., Awaki H., Koyama K., Ptak A., 1997, PASJ, **49**, 619

Usui T., Saito M., Tomita A., 1998, AJ **116**, 2166

Usui T., Saitō M., Tomita A., 2001, AJ, **121**, 2483

van der Werf P.P., Genzel R., Krabbe A., Blietz M., Lutz D., Drapatz S., Ward M.J., Forbes D.A., 1993, ApJ, **405**, 522

Veilleux S., Osterbrock D.E., 1987, ApJS, **63**, 295

Veilleux S., Shopbell P.L., Rupke D.S., Bland-Hawthorn J., Cecil G., 2003, AJ, **126**, 2185

Veilleux S., Cecil G., Bland-Hawthorn J., 2005, ARA&A, **43**, 769

Vignati P., Molendi S., Matt G., Guainazzi M., Antonelli L.A., Bassani L., Brandt W.N., Fabian A.C., Iwasawa K., Maiolino R., Malaguti G., Marconi A., Perola G.C., 1999, A&A, **349**, 57

Weisskopf M.C., Tananbaum H.D., Van Speybroeck L.P., O'Dell S.L., 2000, SPIE, **4012**, 2

Xia X.Y., Xue S.J., Mao S., Boller T., Deng Z.G., Wu H., 2002, ApJ, **564**, 196

Young A.J., Wilson A.S., Shopbell P.L., 2001, ApJ, **556**, 6

Zezas A., Fabbiano G., Rots A H., Murray S.S., 2002, ApJS, **142**, 239

ACKNOWLEDGEMENTS

Many thanks to my advisors, Dr. Stefanie Komossa and Porf. Günther Hasinger, for giving me the opportunity to work on this interesting topic at MPE. I am very grateful to them for allowing me to conducting scientific research, teaching me among many things and opening my view to the large scales of astrophysical research over the three years.

Much appreciation to all the members of the X-ray group for their great help. I am utterly grateful to those who imparted their wisdom and advice: Werner Becker, Vadim Burwitz, Iskra Strateva, Jose Ramirez. Many thanks to Harald Baumgartner for always helping me with my computer.

I would like to express my gratitude to the International Max-Planck Research School on Astrophysics in which I participated. I am thankful for the support of my director Porf. Günther Hasinger and Dr. Werner Becker.

Thanks to friends who read and helped with English and German: Felicitas Mokler, Ludwig Trepl.

I thank to all the friends whow helped and supported me: Felicitas, Alina, Aybüke, David, Wang Jie, Wang Wei and many others.

I wish to thank my parents, who support and encourage me all the time.